

SUPERRESOLUTION NONLINEAR STRUCTURED ILLUMINATION MICROSCOPY BY
STIMULATED EMISSION DEPLETION

by

Han Zhang

Copyright © Han Zhang 2014

A Dissertation Submitted to the Faculty of the

DEPARTMENT OF OPTICAL SCIENCES

In Partial Fulfillment of the Requirements

For the Degree of

DOCTOR OF PHILOSOPHY

In the Graduate College

THE UNIVERSITY OF ARIZONA

2014

THE UNIVERSITY OF ARIZONA
GRADUATE COLLEGE

As members of the Dissertation Committee, we certify that we have read the dissertation prepared by Han Zhang, titled Superresolution Nonlinear Structured Illumination Microscopy by Stimulated Emission Depletion and recommend that it be accepted as fulfilling the dissertation requirement for the Degree of Doctor of Philosophy.

_____ Date: (11/24/2014)
Leilei Peng

_____ Date: (11/24/2014)
Tom Milster

_____ Date: (11/24/2014)
Ron Liang

Final approval and acceptance of this dissertation is contingent upon the candidate's submission of the final copies of the dissertation to the Graduate College.

I hereby certify that I have read this dissertation prepared under my direction and recommend that it be accepted as fulfilling the dissertation requirement.

_____ Date: (11/24/2014)
Dissertation Director: Leilei Peng

STATEMENT BY AUTHOR

This dissertation has been submitted in partial fulfillment of the requirements for an advanced degree at the University of Arizona and is deposited in the University Library to be made available to borrowers under rules of the Library.

Brief quotations from this dissertation are allowable without special permission, provided that an accurate acknowledgement of the source is made. Requests for permission for extended quotation from or reproduction of this manuscript in whole or in part may be granted by the copyright holder.

SIGNED: Han Zhang

ACKNOWLEDGEMENTS

First of all, I would like to gratefully and sincerely thank my advisor, Dr. Leilei Peng, for giving me the opportunity to conduct such an interesting research for this dissertation. Dr. Peng has given me invaluable guidance on my research and spent large amount of her time on a day-to-day basis on my project. Without her thoughtful guidance and encouragement, this dissertation cannot be completed.

I also thank to Dr. Tom Milster and Dr. Ron Liang for serving as my dissertation committee member and giving me the continued support during my study and research.

I also would like to express my thanks to Dr. Ming Zhao, Dr. Yu Li, Golchehr Noshirvaniallahabadi, Run Huang, Dr. Aili Zhang, Kimiko Della Croce, Dr. Guang Yao, Patty Estes, Dr. Daniela C. Zarnescu, Dr. Weibin Zhou, Dr. Young-Sik Kim, Zheng Cai, Yijun Ding, Yuhao Wang, Xinda Hu, Tianquan Su, Wenrui Cai, Qian Li, Liang Gao, Gongwen Zhu, Xiaoyin Zhu, Qiang Fang, Yi Qin and Weibo Chen for their wholehearted support and great insight on my work. I truly enjoyed working with all of these wonderful people and wish everyone the best.

The immeasurable thanks go to my wife and my parents for their deepest love, support and sacrifice. My work cannot be completed without their support.

Dedication

**To my family
whose love and support bring me where I am**

Table of Contents

LIST OF FIGURES	9
LIST OF TABLES	15
Abstract	16
Chapter 1 Introduction to superresolution fluorescence microscopy	18
1.1 Introduction to fluorescence microscopy	18
1.2 Resolution limit in traditional fluorescence microscopy due to light diffraction.....	18
1.3 Current microscopy techniques for extended resolution and superresolution.....	20
1.3.1 Superresolution microscopy based on the manipulation of fluorophore	22
1.3.2 Superresolution microscopy based on manipulation of illumination	23
1.4 Limitation to current superresolution techniques	25
1.5 Outline of the thesis	25
Chapter 2 Introduction to stimulated emission depletion (STED) - structured illumination microscopy (SIM).....	27
2.1 Demonstration of nonlinear SIM theory in spatial and frequency domain	27
2.2 Introduction to the strong nonlinear effect due to STED quenching	33
2.3 Nonlinear structured illumination generated by the combination of a uniform excitation and a linear STED interference	34
2.4 Advantage of STED-SIM compared with other nonlinear SIM.....	35
2.4.1 Comparison between STED-SIM and Saturated-SIM.....	35
2.4.2 Comparison between STED-SIM and Photoswitchable-SIM	39

2.5 Summary	40
Chapter 3 Algorithm Development and Feasibility Study of STED-SIM.....	42
3.1 STED-SIM superresolution image reconstruction algorithm development	42
3.2 STED-SIM superresolution reconstruction simulation	48
3.2.1 Simulation on 1D STED-SIM superresolution reconstruction to study the influence of STED power and interference contrast.....	48
3.2.2 2D simulation with commercial available laser power to predict the feasibility of STED-SIM.....	50
3.2.3 Study of the performance of STED-SIM with a field enhancement mechanism by two dimensional simulation	52
3.3 Summary.....	53
Chapter 4 Surface Plasmon Resonance (SPR) enhanced STED-SIM.....	54
4.1 SPR enhancement.....	54
4.1.1 Introduction to SPR field enhancement mechanism.....	54
4.1.2 Multilayer thin film to generate SPR	56
4.1.3 12 times of field enhancement from SPR by field calculation	58
4.2 SPR enhanced STED effect experiment.....	59
4.2.1 Multilayer thin films fabrication by electron beam vapor deposition	59
4.2.2 8 times STED quenching effect enhancement by SPR in experiments	61
4.3 1D SPR enhanced STED-SIM	66
4.3.1 Optical setup of 1D STED-SIM with SPR enhancement and the sample preparation	66

4.3.2 5-fold improved resolution beyond diffraction limit on fluorescent beads with 1D superresolution reconstruction.....	70
4.4 Challenge and prospect on SPR enhanced STED-SIM.....	75
Chapter 5 Two dimensional superresolution imaging with STED-SIM	77
5.1 2D STED-SIM experimentally demonstrated by fluorescence beads sample	77
5.1.1 Two types of optical setups for 2D STED-SIM: transmitted fluorescence STED-SIM and epi-fluorescence STED-SIM.....	77
5.1.2 STED interference contrast calibration.....	80
5.1.3 2D Superresolution imaging on fluorescent beads	83
5.1.4 Superresolution imaging stability test.....	85
5.2 2D superresolution imaging on fixed biological samples	89
5.2.1 Sample preparation	89
5.2.2 STED-SIM imaging with tubulins of U2OS cell.....	90
5.2.3 STED-SIM imaging with granules of neuron cells	92
5.3 Summary	95
Chapter 6 Summary	96
Appendix-Nonlinear Structured Illumination Application in Light-Sheet	
Microscopy.....	98
A1 Light-sheet microscopy	98
A1.1 Introduction to light-sheet fluorescent microscopy	98
A1.2 Limitation of traditional light-sheet fluorescent microscopy.....	99
A2 Two-photon Bessel light-sheet microscope with nonlinear structured illumination.....	100

A2.1 Introduction to two-photon Bessel light-sheet microscope with nonlinear SIM	100
A2.2 The theory and algorithm development in two-photon Bessel light-sheet microscope with nonlinear SIM.....	101
A2.3 Optical setup and sample preparation.....	105
A2.4 The axial and lateral imaging resolution characterization.....	107
A2.5 Structured illumination parameter optimization.....	108
A2.6 Nonlinear structured light-sheet illumination microscopy on zebrafish kidney.	110
A3 Summary.....	113
References.....	114

LIST OF FIGURES

Figure 1.1	(a) Single point object. (b) Two point objects. (c) Image of the point object shown in (a). (d) Image of two point objects shown in (c).....	20
Figure 1.2	Image acquisition and processing in STORM and PALM. At every cycle, a sparse subset fluorophores are turned on and the position of each fluorophore is fitted. After a number of cycles, the position for all the fluorophores can be decided and therefore formed the final superresolution image.....	23
Figure 1.3	(a) STED beam on object plane. (b) Diffraction limited PSF. (c) Effective PSF in point scanning STED microscopy.....	24
Figure 2.1	Explanation of imaging diffraction limit boundary in spatial domain and frequency domain.....	28
Figure 2.2	Examples of Moiré pattern.....	29
Figure 2.3	Principle of linear SIM in spatial domain and frequency domain.....	31
Figure 2.4	Explanation of nonlinear SIM principle in spatial domain and frequency domain.	32
Figure 2.5	The energy band diagram in (a) spontaneous emission and (b) Stimulated emission.	34
Figure 3.1	(a) 1D saturated structured illumination. (b) 2D STED interference pattern. (c) Effective nonlinear illumination pattern after an emission filter with the combination of a linear 2D STED pattern and a uniform excitation. (d) 2D frequency domain image patching during superresolution reconstruction with 1D	

	structured illumination. (e) 2D frequency domain image patching during superresolution reconstruction with our 2D grid pattern.....	46
Figure 3.2	(a) Simulated object. (b) Simulated raw images after excited by structured illumination with varied phases. (c) Fourier components in different frequency domain after image processing. (d) Reconstructed image in frequency domain. (e) Superresolution image in spatial domain. (f) Simulated diffraction limit image from object in (a).....	47
Figure 3.3	(a) STED nonlinear structured illuminations with STED powers of 5 Isat and 30 Isat, respectively. (b) STED nonlinear structured illuminations with interference contrasts of 90% and 100%, respectively. STED power is set to be 10 Isat.....	48
Figure 3.4	(a) One dimensional simulated object. Those simulated particles have the separations of 30 nm, 40 nm, 50 nm and 300 nm. (b) Simulated diffraction limit image from object in (a). (c) Simulated 1D STED-SIM reconstructed image with 95% contrast from object in (a). (d) Simulated 1D STED-SIM reconstructed image with 90% contrast from object in (a).....	50
Figure 3.5	(a) Two dimensional simulated object. Those simulated bars have the separations of 24 nm, 36 nm, 48 nm, 60 nm and 72 nm. (b) Simulated diffraction limit image from object in (a). (c) Simulated 2D STED-SIM reconstructed image with 95% interference contrast and 5 Isat average power from object in (a). (d) Simulated 2D STED-SIM reconstructed image with 95% interference contrast and 20 Isat average power from object in (a).....	52

Figure 4.1	Laser introduced surface plasmons and electric field enhancement of surface plasmon resonance.....	56
Figure 4.2	(a) Fluorescence quenching due to the absorption of metal. (b) The exponential decay of SPR evanescent field (blue curve) and the relative fluorescence emission from the fluorophore after the quenching of metal absorption (red curve).....	57
Figure 4.3:	(a) Electric field enhancement against silver thickness. (b) Electric field enhancement against incident angle. The blue plot is from parallel beam single wavelength simulation and the red one is from Gaussian focused beam with broadband wavelength.....	59
Figure 4.4	AFM image of (a) pre-clean coverslip surface, (b) pre-clean coverslip surface after piranha wash, (c) 40 nm silver and 15 nm SiO ₂ coating on top of pre-clean coverslip and (d) 40 nm silver and 15 nm SiO ₂ coating on top of piranha washed pre-clean coverslip. The field of view of each image is 1 × 1 μm ² . The RMS of the surface roughness is (a) 4.9 nm, (b) 0.2 nm, (c) 3.2 nm and (d) 0.9 nm.....	60
Figure 4.5	TIRF-STED setup for measuring SPR enhanced STED effect. PBS: Polarized beam splitter. DM: Dichroic mirror. The inset is the multilayer structure to generate SPR enhanced STED effect.....	62
Figure 4.6	ATTO 633 spectrum.....	63
Figure 4.7	STED effect with and without SPR enhancement.....	65
Figure 4.8	1D SPR-enhanced STED-SIM setup. The inset shows the SPR interference generated by laser beam and thin films.....	67
Figure 4.9	Fluosphere sample preparation process.....	69

Figure 4.10	1D SPR-enhanced STED-SIM image processing.....	72
Figure 4.11	(a) Diffraction limit image. (b) Superresolution reconstruction with linear term only. (c) Superresolution reconstruction with up to second harmonics nonlinear term. (d) Fourier domain image of (a). (e) Fourier domain image of (b). (f) Fourier domain image of (c).....	73
Figure 4.12	(a) Diffraction limit image of one fluorescent bead. (b) Superresolution image of the same beads with reconstruction up to 3rd nonlinear harmonic terms in Fourier domain. (c) The cross section of bead image between the arrows in (a) and (b). The blue and green plots are for diffraction limit and STED-SIM images respectively.....	74
Figure 4.13	(a) Two SPR fields on the surface of multi-layer film. (b) The overlap of two SPR fields. (c) Interference field distortion on rough multi-layer films simulation.....	76
Figure 5.1	Optical setup for 2D STED-SIM transmitted fluorescence microscope.....	78
Figure 5.2	Optical setup for 2D epi-fluorescence type STED-SIM.....	79
Figure 5.3	(a) 2D STED pattern. The field of view is $25 \times 25 \mu\text{m}^2$. (b) STED interference contrast calibration experiment. One dimensional STED interference is scanned across a single bead while illuminated by a uniform excitation. A camera is placed after emission filter to detect fluorescence signal emitted from this single bead..	80
Figure 5.4	The STED interference contrast test.....	82
Figure 5.5	(a) Full field diffraction limit image. (b) Full field STED-SIM superresolution image. (c) Magnified image of the red square region in (a). (d) Magnified image of the red square region in (b).....	84

Figure 5.6	Beads profile between arrows in figure 5.5 (a) and (b).....	85
Figure 5.7	Grating stability test.....	87
Figure 5.8	Grating stability test at different time.....	88
Figure 5.9	(a) Diffraction limit image of tubulins in fixed U2OS cell, labeled with ATTO 633. The field of view is $12 \times 12 \mu\text{m}^2$ (b) STED-SIM superresolution image of the same object in (a).....	90
Figure 5.10	(a) Reconstructed image with artifacts. (b) Reconstructed image without artifacts. (c) The Fourier domain image of (a). (d) The Fourier domain image of (b).....	92
Figure 5.11	(a-e) Diffraction limit images of granules of neuron cells. (f-j) STED-SIM images of the same objects.....	94
Figure A1	The nonlinear SIM Imaging processing steps to remove strong diffused signal in light-sheet imaging of deep tissue structures.....	104
Figure A2	(a) Optical schematic of the nonlinear structured illumination Bessel beam two-photon light-sheet microscope. SLM: spatial light modulator. (b) Two-photon emission from a cuvette of fluorescein solution under a focused Gaussian beam, and (c) under a Bessel beam.....	106
Figure A3	Axial and lateral resolution calibration.....	107
Figure A4	(a) Nonlinear structured two-photon excitation image from a fluorescein solution sample. (b) Normalized spatial power spectrum of two-photon excitation patterns showing high order harmonics of the pattern. (c) Normalized spectra powers at different harmonic orders of the excitation pattern with different pattern period.	

	Different color represents varied pattern period. The dashed line is the typical noise level of light-sheet images deep inside zebrafish.....	108
Figure A5	Diffusion reductions with our novel nonlinear SIM reconstruction algorithm....	110
Figure A6	3D two-color images of kidney cellular structure of a live double transgenic zebrafish larva at 4dpf. Green fluorescence protein (GFP) labels endothelial cells in the vasculature and presented in green color.....	112

LIST OF TABLES

Table 4.1	Full-field STED on different substrates.....	66
-----------	--	----

Abstract

The understanding of the biological processes at the cellular and subcellular level requires the ability to directly visualize them. Fluorescence microscopy played a key role in biomedical imaging because of its high sensitivity and specificity. However, traditional fluorescence microscopy has a limited resolution due to optical diffraction. In recent years, various approaches have been developed to overcome the diffraction limit. Among these techniques, nonlinear structured illumination microscopy (SIM) has been demonstrated a fast and full field superresolution imaging tool, such as Saturated-SIM and Photoswitching-SIM.

In this dissertation, I report a new approach that applies nonlinear structured illumination by combining a uniform excitation field and a patterned stimulated emission depletion (STED) field. The nature of STED effect allows fast switching response, negligible stochastic noise during switching, low shot noise and theoretical unlimited resolution, which predicts STED-SIM to be a better nonlinear SIM. After the algorithm development and the feasibility study by simulation, the STED-SIM microscope was tested on fluorescent beads samples and achieved full field imaging over 10×10 micron square at the speed of 2s/frame with 4-fold improved resolution. Our STED-SIM technique has been applied on biological samples and superresolution images with tubulin of U2OS cells and granules of neuron cells have been obtained.

In this dissertation, an effort to apply a field enhancement mechanism, surface plasmon resonance (SPR), to nonlinear STED-SIM has been made and around 8 time enhancement on STED quenching effect was achieved. Based on this enhancement on STED, 1D SPR enhanced STED-SIM was built and 50 nm resolution of fluorescence beads sample was achieved.

Algorithm improvement is required to achieve full field superresolution imaging with SPR enhanced STED-SIM.

The application of nonlinear structured illumination in two photon light-sheet microscopy is also studied in this dissertation. Fluorescent cellular imaging of deep internal organs is highly challenging because of the tissue scattering. By combining two photon Bessel beam light-sheet microscopy and nonlinear SIM, 3D live sample imaging at cellular resolution in depth beyond 200 microns has been achieved on live zebrafish. Two-color imaging of pronephric glomeruli and vasculature of zebrafish kidney, whose cellular structures located at the center of the fish body are revealed in high clarity.

Chapter 1 Introduction to superresolution fluorescence microscopy

1.1 Introduction to fluorescence microscopy

Fluorescence, the luminescence of a substance when excited by radiation, carries longer wavelength than illumination light and is widely used as a mean of preparing specific biological probes. Fluorescence microscope was developed to use the fluorescence, instead of reflection, transmission or absorption, to study the properties of many types of substance. In a typical fluorescence microscope design, a bright light source with specific wavelengths and a set of matched spectral filters are required to generate the fluorescence from sample and separate the emission signal from excitation. Biological samples can be fluorescently stained or genetically modified so that a protein of interest carries a fluorescent reporter molecule, which allow observers to track specific components of the target sample during the imaging. Fluorescence microscope has become one of the most essential tools for visualizing biological specimen with high specificity, high sensitivity and high resolution.

1.2 Resolution limit in traditional fluorescence microscopy due to light diffraction

However, like all microscopes, traditional fluorescence microscopy has a limit on imaging resolution due to light diffraction, termed as Abbe diffraction limit. The limited resolution follows the relation in Eq.1.1.

$$d = \frac{1.22\lambda}{2NA} \quad (1.1)$$

where λ is the wavelength of detected light and NA is the numerical aperture of the imaging system. Typically in fluorescence microscopy, the resolution is limited to around 300 nm with visible light and an oil-immersion high NA objective.

This diffraction limit, presented as a point spread function (PSF) that is an Airy disk function in an ideal imaging system, causes a finite spread in the image from an infinite small point object. The optical terminology, Airy disk, describes the best focused spot of light that a perfect circular lens can provide, which is limited by the diffraction of light. In figure 1.1(a) and (c), a single point in the object plane will generate an Airy disk image with the width of the diffraction limit. Two points with a separation smaller than the diffraction limit cannot be resolved from image (figure 1.1 (b) and (d)). The resolution of an imaging system is determined by the minimal distance between two resolvable points, which is the width of point spread function (PSF).

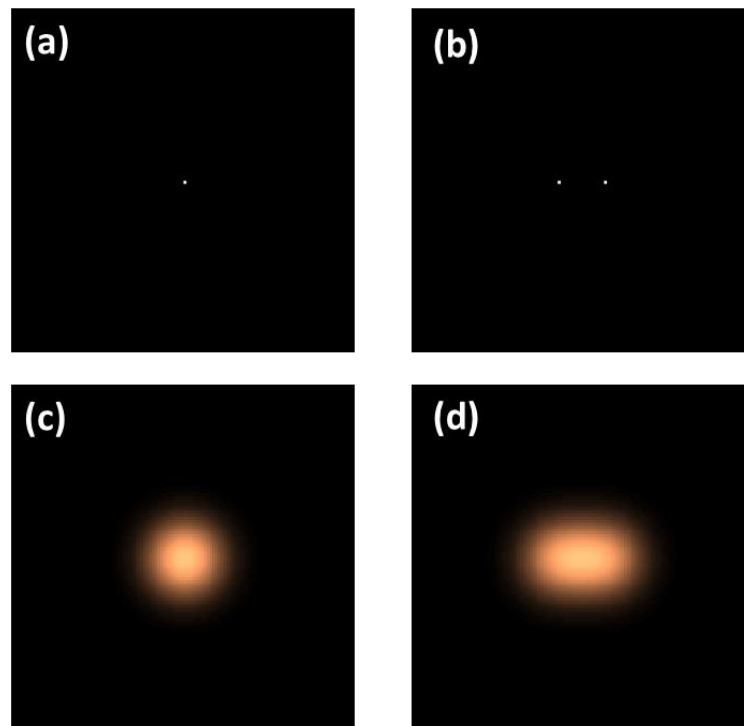


Figure 1.1 (a) Single point object. (b) Two point objects. (c) Image of the point object shown in (a). (d) Image of two point objects shown in (c).

1.3 Current microscopy techniques for extended resolution and superresolution

Several far-field imaging techniques are known to extend resolution beyond the diffraction limit. Among those techniques, confocal and multiphoton microscopies are most widely utilized in biomedical study [1-5]. By combining a focused excitation beam and a pinhole in detection path, confocal microscope has a resolution improvement factor of $\sqrt{2}$ in theory. By exciting the dyes with multiple photons, the effective point spread function (PSF) of multiphoton microscopy can be reduced by nonlinear absorption process. However, this improvement in PSF is counteracted by the increase of excitation wavelength. Therefore, instead of resolution improvement, those techniques are developed to enable 3D imaging.

In the past decade, several techniques, termed as superresolution fluorescence microscopy, were developed to overcome the diffraction limit on imaging resolution [6-12]. Based on principles of those superresolution techniques, they can be categorized to two groups:

1. Superresolution fluorescence microscopy based on the manipulation of fluorophore, such as photoactivated localization microscopy (PALM) [13-15], fluorescence photoactivation localization microscopy (fPALM) [16, 17], ground-state depletion with individual molecule return microscopy (GSDIM) [18, 19] and stochastic optical reconstruction microscopy (STORM) [20-23]. Those techniques can achieve full field superresolution image based on the localization of single molecule.

2. Superresolution fluorescence microscopy based on the manipulation of illumination, such as point scanning stimulated emission depletion (STED) microscopy [24-27], linear structured illumination microscopy (SIM) [28-31] and nonlinear SIM [32, 33]. By applying manipulated illumination, the specimen can be excited at the region smaller than imaging PSF. For instance, in point scanning STED, the width of effective excitation PSF decrease as STED power increase and can reach to the size below 20 nm [34]. And in linear SIM, the width of each excitation interference peak is half of the diffraction limit. The width of effective excitation region decides the resolution of new imaging system.

There are also some techniques utilizing both the manipulation of fluorophore and the manipulation of illumination to achieve the superresolution imaging. For example, photoswitching SIM is a hybrid technique between the above two categories [33].

1.3.1 Superresolution microscopy based on the manipulation of fluorophore

The biological structure is ultimately defined by the molecules that build up this structure, which means, in fluorescent imaging, the coordinates of all the fluorophores decide how the image looks like. Therefore, the resolution of the fluorescent imaging system can be determined by the position precision of each fluorophore contained in the image.

If the distribution of fluorophores is sparse, single molecule imaging can easily locate these fluorophores precisely. The Airy disk image of a single fluorophore can be fitted with ideal Airy function. And the fluorophore location presented by fitted Airy function center can be much more precise than diffraction limit. The fluorophore location accuracy is decided by the number of photon emitted from this fluorophore and detected by camera, following E.q. 1.2 [35]:

$$d_{precision} = \frac{d}{\sqrt{N}} \quad (1.2).$$

Where d is the diffraction limit and N is the photon of detected photons from same fluorophore.

However, in biological sample, the distribution of fluorophores is usually dense. The Airy disk images of multiple fluorophores overlap together and forbid Airy function fitting. The single molecule imaging technique realizes superresolution by turning on a small subset of fluorophores, the fluorophore location of which can be determined by Airy function fitting. Once the location of every fluorophore has been determined for this sparse subset, another sparse subset with different fluorophores turned on is acquired. This process is repeated over many cycles until most of the fluorophores contained in the object are covered. Hundreds of small subsets are then merged to form the superresolution image. The image forming process is illustrated in figure 1.2.

The solid rounds and hollow rounds represent the fluorophores which have been turned on or off. And the crosses in this figure present the located fluorophores. After many cycles, the number of located fluorophores keeps increasing. Eventually, the coordinates of all the fluorophores can be acquired. Based on this technique, fPALM and STORM can achieve the fluorescent image with resolution better than 20 nm [20].

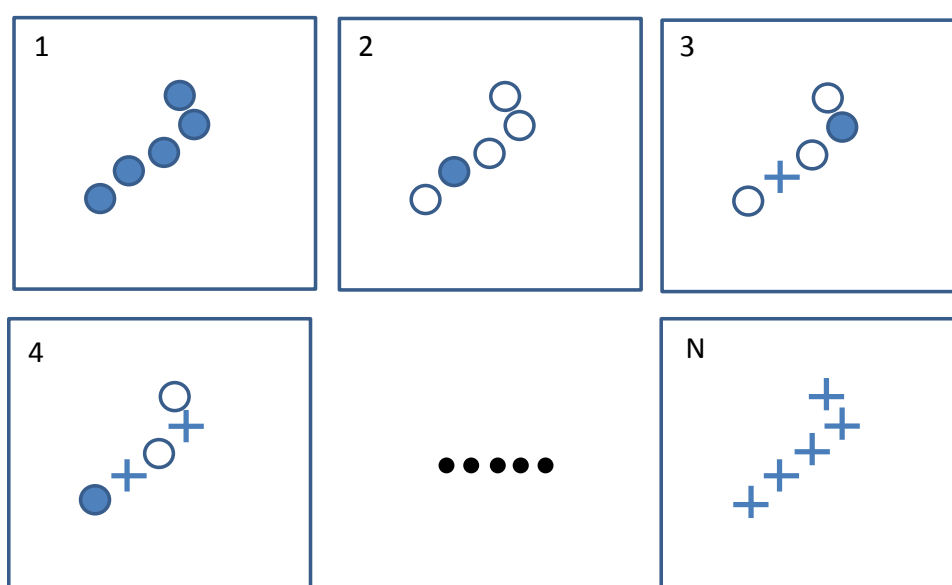


Figure 1.2 Image acquisition and processing in STORM and PALM. At every cycle, a sparse subset fluorophores are turned on and the position of each fluorophore is fitted. After a number of cycles, the position for all the fluorophores can be decided and therefore formed the final superresolution image.

1.3.2 Superresolution microscopy based on manipulation of illumination

The nature of the diffraction limit on resolution is that our ability to focus the light to a single spot is restricted by light diffraction. The manipulation of illumination technique, which utilized in point scanning STED [36] and SIM superresolution microscopy [28, 37, 38], can break this limit.

By turning off the fluorophores inside the excitation PSF region except the center, point scanning STED microscopy is able to decrease the size of the effective PSF. Figure 1.3 (a) shows the STED beam shape on the object plane which can turn off the fluorophores. In figure 1.3 (b), without donut shape STED beam, the PSF is diffraction limited. With STED beam, since only the fluorophores at the center part of the donut shape beam is not turned off, the size of effective PSF can be decreased significantly as presented in figure 1.3 (c). The size of the effective PSF decides the resolution of the imaging system.

Another technique that relies on the manipulation of illumination is SIM. By illuminating the specimen with an excitation interference pattern, linear SIM can shift the frequency information beyond the diffraction limit boundary into the directly observation region in spatial frequency domain and improve the resolution by two times. To further improve the imaging resolution, strong nonlinear effect can be combined with SIM to perform nonlinear SIM. The detail of SIM and nonlinear SIM will be introduced in Chapter 2.

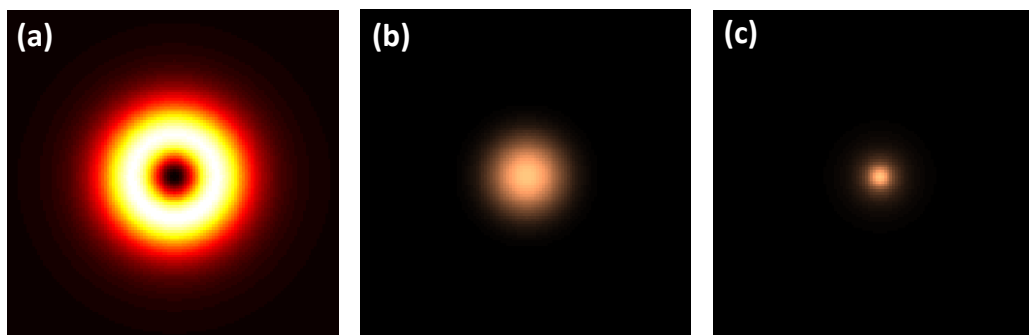


Figure 1.3 (a) STED beam on object plane. (b) Diffraction limited PSF. (c) Effective PSF in point scanning STED microscopy.

1.4 Limitation to current superresolution techniques

Although all of the above techniques have been approved to be practical in biomedical imaging [39-46], they all have their limitations during the application. The imaging speed for single molecule based superresolution technique can be extremely slow, since thousands of cycles are required to cover most of the fluorophores in the specimen. And the turning on/off process is random which leads to the possibility that some fluorophores are not shown in the final image even after thousands of cycles. As a point scanning technique, point scanning STED microscopy has the compromise between imaging speed and the field of view which make video rate imaging challenging over large field of view. And as a full field microscopy, linear SIM is currently the most practical superresolution technique. However, the resolution of linear SIM can only be improved by a factor of 2. To pursue better resolution improvement, nonlinear effect needs to be introduced into the system and will be discussed in detail in chapter 2.

1.5 Outline of the thesis

In this dissertation, a new nonlinear structured illumination microscopy, termed as STED-SIM is reported. In chapter 2, the principle of STED-SIM and its unique advantage comparing with other nonlinear SIMs are introduced. Chapter 3 illustrates the algorithm development and the feasibility verification by simulation on STED-SIM. In chapter 4, a field enhancement mechanism, surface plasmon resonance, is introduced into STED-SIM imaging system in order to achieve better resolution. The experimental result of SPR-enhanced STED-SIM is presented. In chapter 5, the biological sample imaging of our regular STED-SIM microscope is reported. Superresolution image has been acquired in fixed cell samples. In the appendix, the application of nonlinear SIM in Bessel beam two-photon light sheet microscopy is reported. Two-color

imaging of pronephric glomeruli and vasculature of zebrafish kidney, whose cellular structures located at the center of the fish body are revealed in high clarity by two-color two-photon Bessel light-sheet SIM.

Chapter 2 Introduction to stimulated emission depletion (STED) - structured illumination microscopy (SIM)

In this chapter, the basic principal of nonlinear structured illumination microscopy will be introduced. By applying a strong nonlinear effect, STED quenching effect, a novel Nonlinear SIM termed as STED-SIM is proposed to perform fast superresolution microscopy in full field. Compared with other nonlinear SIM, STED-SIM has the fundamental advantages of fast imaging speed, negligible switching stochastic noise, low shot noise and theoretically unlimited resolution.

2.1 Demonstration of nonlinear SIM theory in spatial and frequency domain

To fully understand the principle of nonlinear structured illumination microscopy, the imaging forming processes in both spatial and frequency domain need to be studied. The formation of a diffraction limited image can be described mathematically in the spatial domain by multiplying the object with illumination and then convolving with the point spread function (PSF) of the imaging system (Figure 2.1). With uniform illumination and theoretic diffraction limit airy disk PSF, periodic patterned objects with low spatial frequency and high spatial frequency were both simulated. Figure 2.1 (left) shows the object with low spatial frequency can be resolved while the one with high spatial frequency cannot, which can be understood more clearly in frequency domain as illustrated in figure 2.1 (right). The Fourier transform of the PSF from an imaging system is the optical transfer function (OTF) for the same imaging system. As shown in figure 2.1 (right), for a theoretic airy disk PSF, the OTF is a cone centered in the spatial frequency domain, of which the circular boundary is the diffraction limit frequency. Any spatial frequency information inside the diffraction limit boundary can be directly observed by the imaging system.

The entire frequency components of low spatial frequency object in figure 2.1 (left) are contained inside the diffraction limit boundary, so it can be directly resolved as described previously. For the high spatial frequency object, the high frequency components have been beyond the diffraction limit boundary and cannot be directly obtained in the observed image. Only the component with zero frequency can be observed in the final image as shown in figure 2.1 (right).

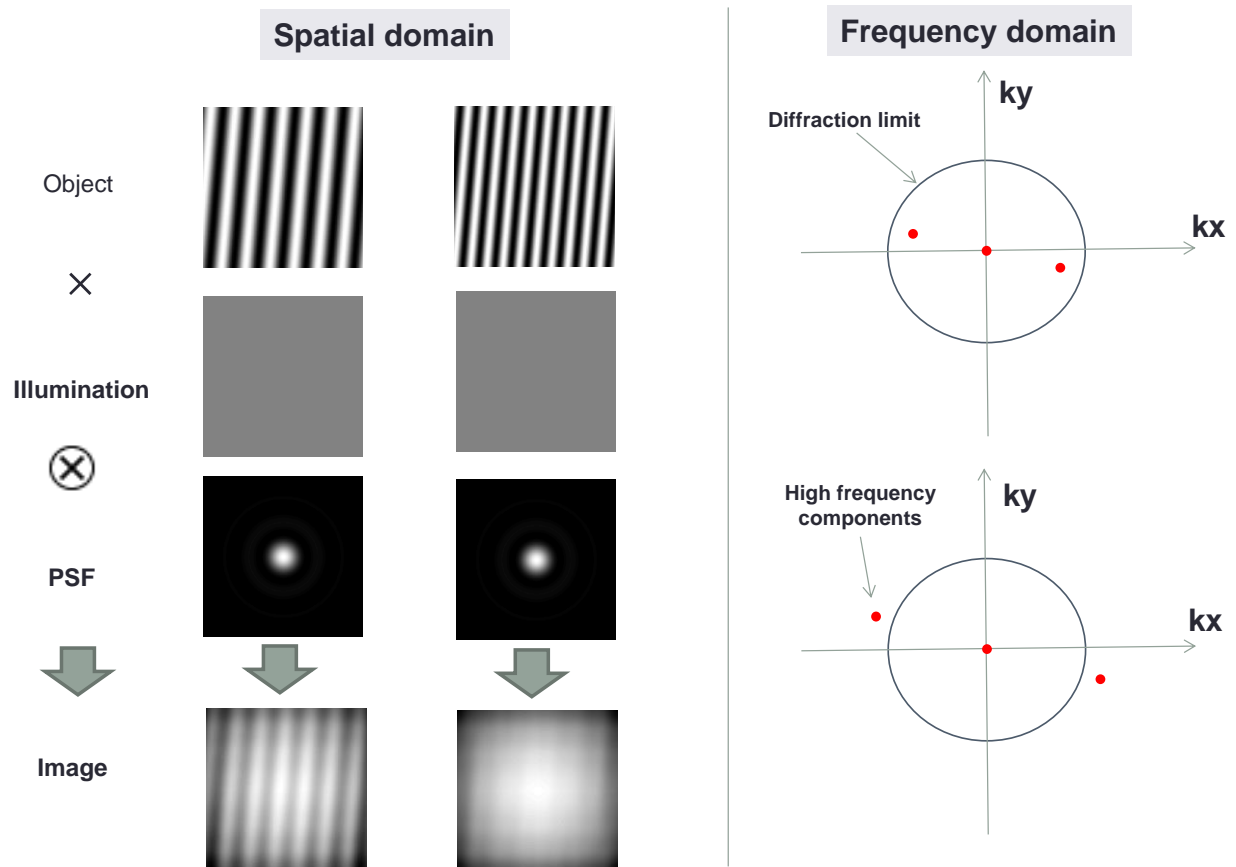


Figure 2.1 Explanation of imaging diffraction limit boundary in spatial domain and frequency domain. (Left) Image forming processes in spatial domain for objects with high spatial frequency and low spatial frequency, a uniform illumination is employed. (Right) The frequency components of the same objects described in (left) and the diffraction limit boundary in spatial frequency domain.

In the aforementioned cases, a uniform illumination is employed and the final images were strictly diffraction limited. To break the limitation of light diffraction, the Moiré pattern effect can be introduced to an imaging system [28]. Figure 2.2 shows two cases of the generation of moiré pattern, which is a secondary pattern created by two superimposed pattern. When a high spatial frequency sample is illuminated by a structured pattern, a moiré pattern with low spatial frequency can be observed in the final illuminated object. It means that the high frequency information of the object is contained in the low spatial frequency moiré pattern and then detected by imaging system.

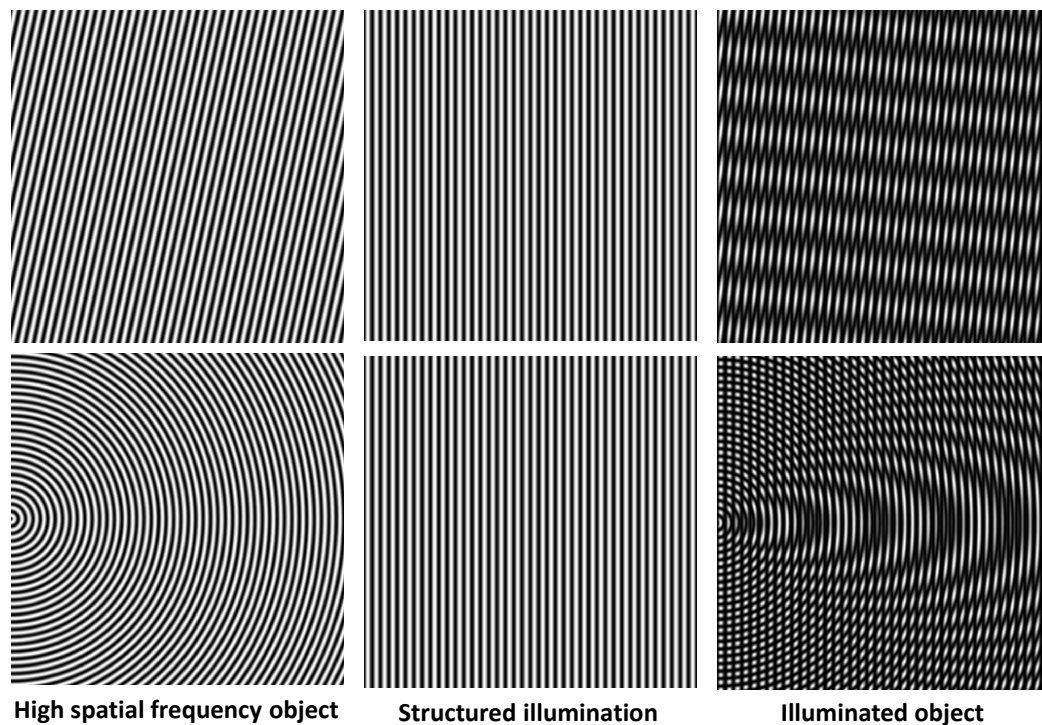


Figure 2.2 Examples of Moiré pattern. (Left) The simulated object with high spatial frequency. (Middle) The patterned illumination. (Right) The Moiré pattern revealed in the illuminated object.

Similar to the imaging process described in figure 2.1, the principle of linear SIM can be studied in both spatial and frequency domain. In figure 2.3, instead of uniform illumination, a patterned illumination was performed on top of the object. As presented in figure 2.3 (left), after imaging process, the previous unresolved object introduced in figure 2.1 has an image with Moiré pattern which contains the high frequency information and therefore can be utilized in the superresolution reconstruction process later. The top diagram in figure 2.3 (right) explains this case. The components with high frequency can be shifted into diffraction limit boundary and contained in the directly observed image after illuminated by a patterned light [47].

However, the resolution of linear SIM can only be improved by 2-fold. In the bottom diagram of figure 2.3 (right), if the frequency component exceeds the domain which is two times larger than diffraction limit domain, it could not be contained in the image with a linear structured illumination. In spatial domain, the Moiré pattern would not be observed as illustrated in figure 2.3 (left) with a higher spatial frequency object.

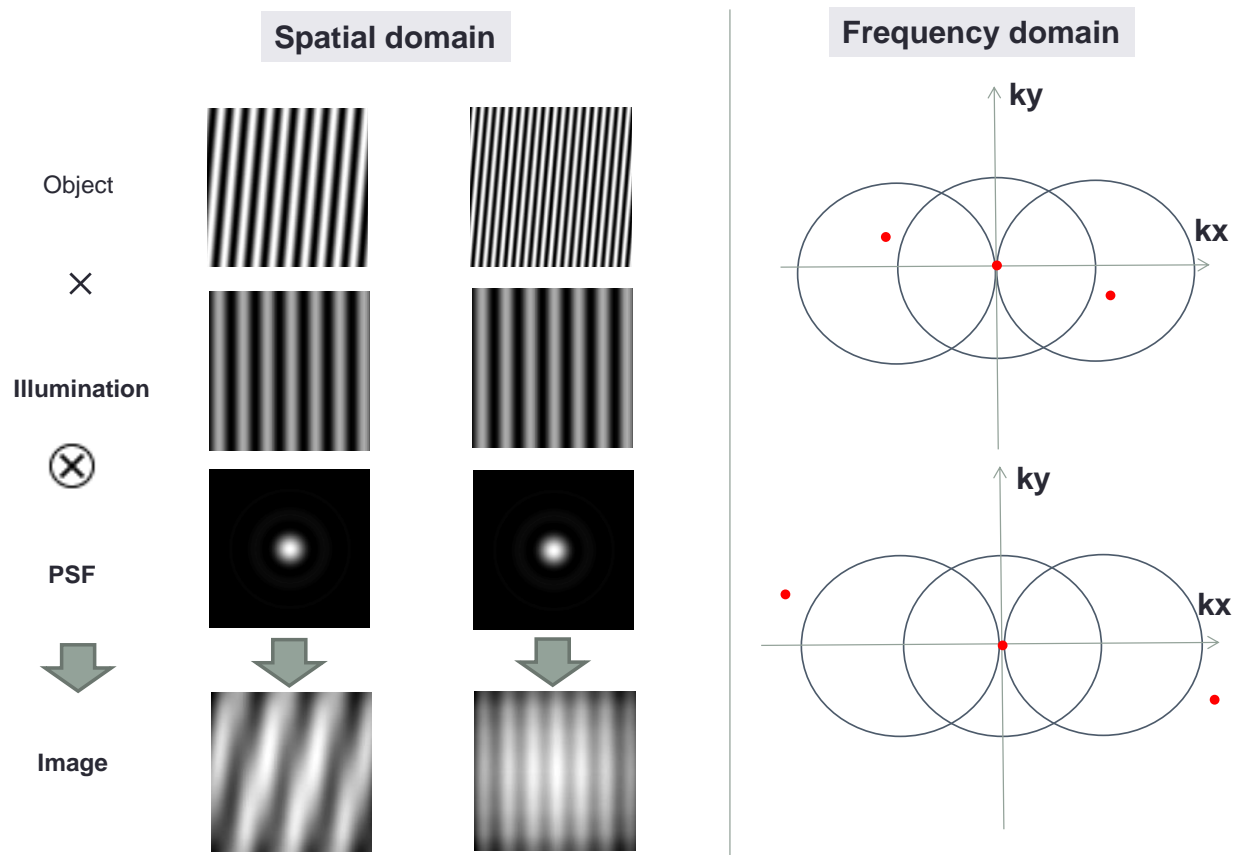


Figure 2.3 Principle of linear SIM in spatial domain and frequency domain. (Left) Image forming processes in linear SIM with high spatial frequency and low spatial frequency objects, a linear patterned illumination is employed. (Right) The frequency components of the same objects in Fourier domain during linear SIM reconstruction process. Nonlinear SIM further improves the resolution of structured illumination microscopy by using a structured illumination that generates a strong nonlinear effect on the object [32]. Effectively, the image is formed by multiplying the object with a nonlinear structured pattern and convolving with PSF of imaging system. Figure 2.4 (left) illustrates the spatial domain representation of nonlinear SIM, in which an object which cannot be resolved with linear SIM contains the Moiré pattern that carries the high spatial frequency information after illuminated by a nonlinear pattern. After reconstruction following the algorithm we will discuss in next chapter, the superresolution

image can be acquired. In the frequency domain, the nonlinear SIM effectively shift the frequency information in higher harmonic orders to the domain inside the diffraction limit boundary. Figure 2.4 (right) shows the higher order solved in nonlinear SIM leads to image information at higher frequency and better resolution in spatial domain. Linear term, 1st order harmonics and 2nd order harmonics give the resolution of 120 nm, 80 nm and 65 nm respectively, assuming the diffraction limited resolution is at 250 nm.

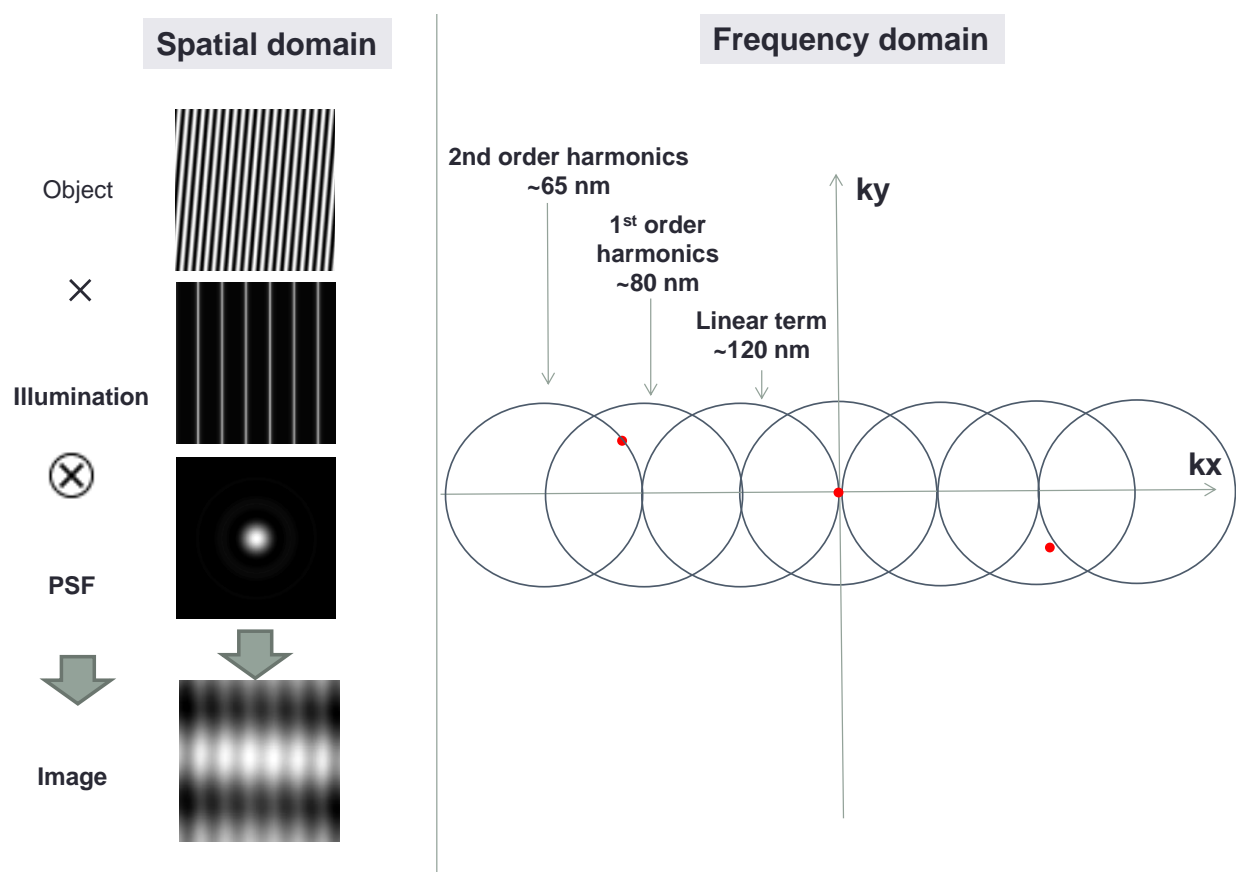


Figure 2.4 Explanation of nonlinear SIM principle in spatial domain and frequency domain. (Left) Image forming processes in nonlinear SIM with high spatial frequency object, a nonlinear structured illumination employed. (Right) The spatial frequency information of the same object and the Fourier domain explanation in nonlinear SIM. Higher order solved in frequency domain gives better resolution in spatial domain.

2.2 Introduction to the strong nonlinear effect due to STED quenching

In fluorescent imaging, various types of nonlinear effect can be employed to generate nonlinear structured illumination. Saturated SIM (SSIM) and Photon-switchable SIM have been previously demonstrated [32, 33]. The nonlinear effect we utilized is the stimulated emission depletion nonlinear (STED) effect [48]. The nature of STED effect allows fast switching response, negligible stochastic noise during switching, low overall background and theoretical unlimited resolution, which predicts STED-SIM to be a better alternative to SSIM and photoswitchable-SIM. The comparison between nonlinear SIMs will be discussed in detail in the following section. The nonlinear effect of STED comes from the stimulated emission of fluorophore. Figure 2.5 (a) illustrates the spontaneous emission process of a fluorophore. The emission lights have a broad bandwidth, the wavelengths of which are on the red side of the excitation wavelength. At the same time, if there is a strong stimulating light interacting with some of the fluorophores, the fluorescent emission from those fluorophores would have exact the same phase, frequency, polarization, and travel direction as the stimulating light (figure 2.5 (b)) [49]. The stronger the stimulating light is, the higher the chance of stimulated emission is and the weaker the spontaneous emission will be. The strength of spontaneous emission from certain amount of fluorophores decreases as the intensity of incident stimulating light increases, as plotted in figure 2.7 (b). The intensity of spontaneous emission has strong nonlinear relation with the strength of stimulating light. This nonlinear effect has been applied in our STED-SIM to generate the structured illumination with strong nonlinearity as introduced in the following section.

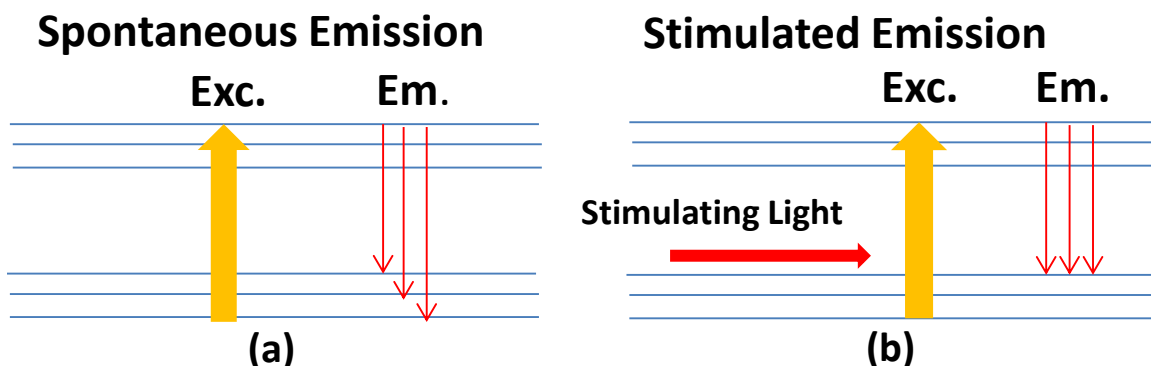


Figure 2.5 The energy band diagram in (a) spontaneous emission and (b) stimulated emission.

2.3 Nonlinear structured illumination generated by the combination of a uniform excitation and a linear STED interference

To apply STED effect to SIM system to generate nonlinear structured illumination, a uniform excitation and a linear sine pattern STED field were employed on the sample plane simultaneously, as illustrated in figure 2.7. With this illumination scheme, after being excited, the fluorophores would have spontaneous and stimulated emission depending on the location. The location where the STED field reaches its maximum intensity has the highest chance for stimulated emission to occur in the fluorophores, while at the STED interference valley, the probability of stimulated emission from fluorophores would be at its minimum. In the imaging path, an emission filter that blocks the STED wavelength was used. Only the fluorophores at/near the valley of STED interference can be observed by camera. The effective nonlinear structured illumination is shown in figure 2.7.

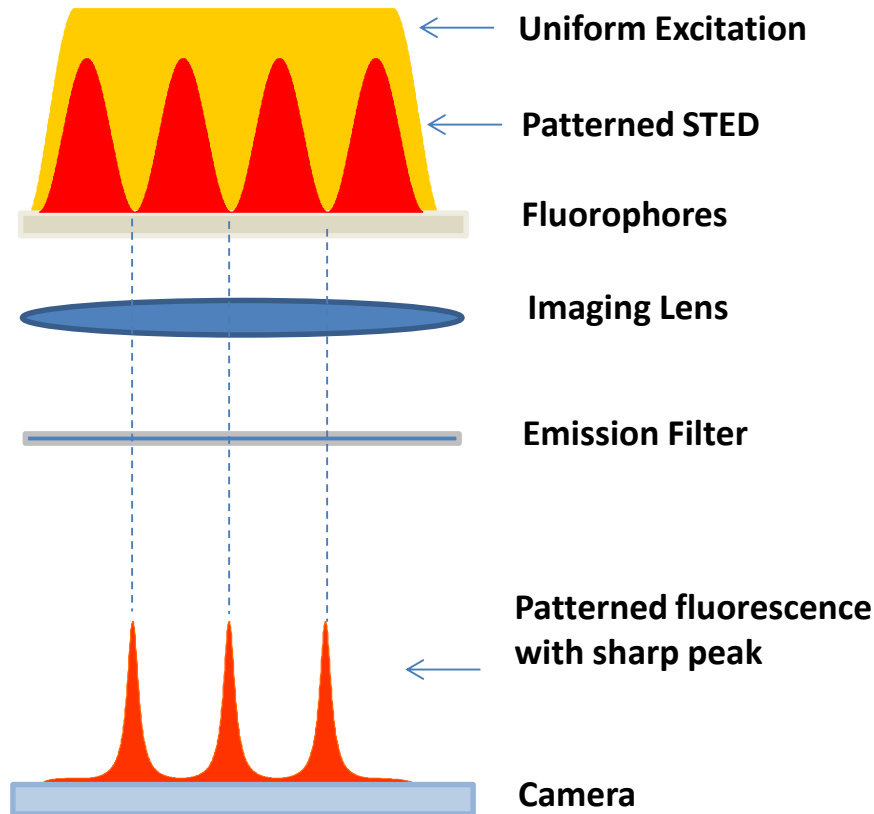


Figure 2.6 The schematic of the forming of nonlinear structured illumination with the combination of linear STED interference pattern and a uniform illumination

2.4 Advantage of STED-SIM compared with other nonlinear SIM

2.4.1 Comparison between STED-SIM and Saturated-SIM

The first nonlinear SIM approach was demonstrated in 2005. The nonlinearity of saturation was applied in SIM to further increase the resolution which had already been improved by 2-fold in linear SIM [32]. In Saturated-SIM, the fluorescence intensity against excitation strength follows the nonlinear relation:

$$\text{Fluorescence} \sim \frac{I_{ex}}{I_{ex} + I_{sat}} \quad (2.1)$$

Where I_{ex} is the excitation power and I_{sat} is the constant to present the fluorophore's saturation power. As plotted in figure 2.6 (a), the fluorescence emission would reach its maximum as the excitation increases for certain fluorophore concentration. The saturated structured-illumination turns most part of the sample into the 'on' state. The simulated results are shown in figure 2.8 (a). In comparison, following the nonlinear relation [50]:

$$\text{Fluorescence} \sim \frac{I_{sat}}{I_{ex} + I_{sat}} \quad (2.2)$$

STED-SIM realizes nonlinear structured illumination by turning most part of the sample into the 'off' state as shown in figure 2.8 (b). This feature allows STED-SIM to perform superresolution imaging with less shot noise and less photon bleaching on fluorescen

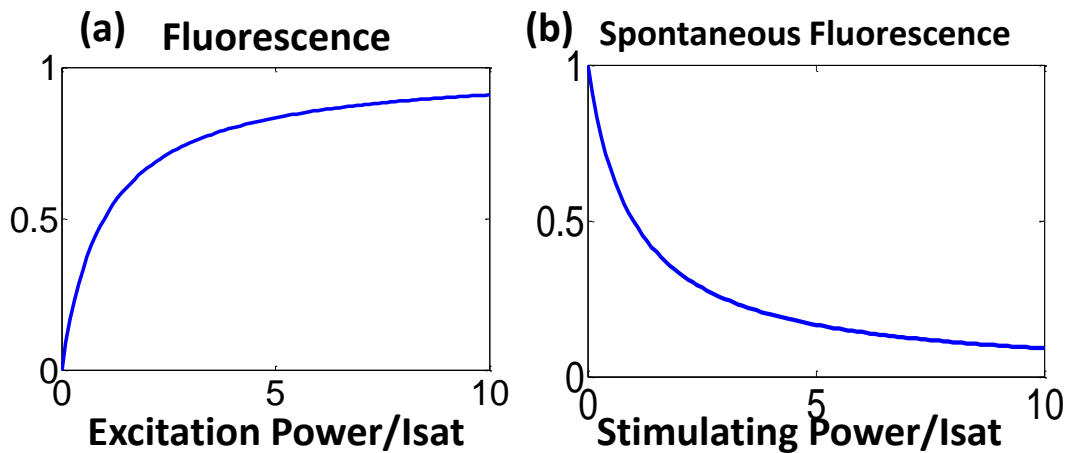


Figure 2.7 Spontaneous fluorescence strength in (a) Saturation (b) STED.

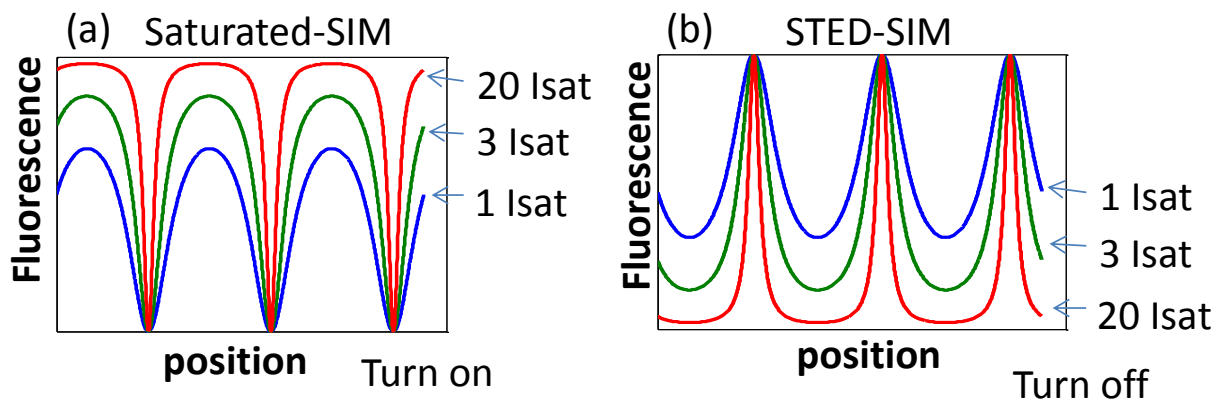


Figure 2.8 Effective nonlinear structured illumination patterns in (a) Saturated-SIM and (b) STED-SIM.

Saturated-SIM also has self-limiting resolution, whereas the resolution of STED-SIM is unlimited in theory. Figure 2.9 presents the relative strengths of high order harmonics for Saturated-SIM against the excitation power [51]. The curves with different colors represent varied harmonics orders as marked in the figure. The dashed line is assumptive minimal detectable signal noise ratio (SNR) level. The harmonics orders with larger than minimal detectable SNR level strength can be retrieved after imaging processing and contribute to better resolution. As the excitation power increases, clearly presented in figure 2.9, the harmonics orders which can be solved decreases. This restriction gives Saturated-SIM self-limited resolution. As the excitation power raise, both the shot noise and the saturation nonlinearity increase. However, the shot noise increase faster than saturation nonlinearity. This is the fundamental reason of the self-limited resolution in Saturated-SIM.

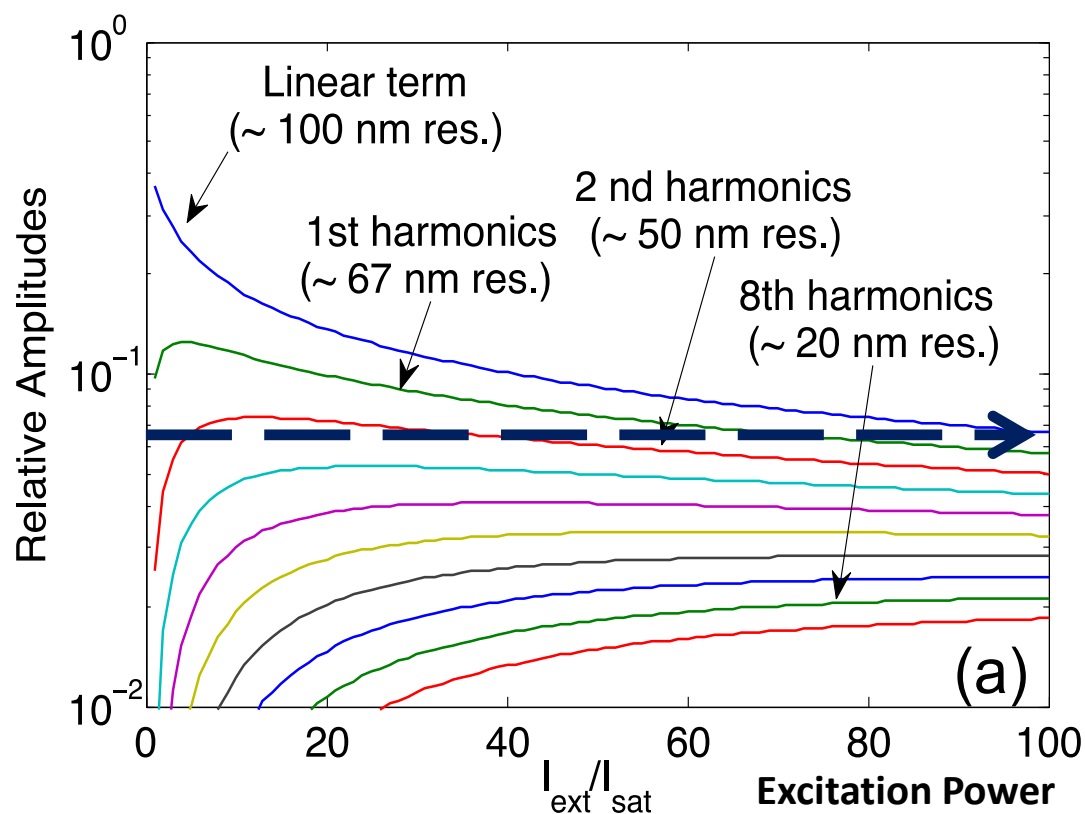


Figure 2.9 The strength of Saturated-SIM nonlinear high order harmonics as excitation power increases. Different colors of the curves represent varied harmonics orders: blue for linear term, green for 1st harmonics order, red for 2nd harmonics order and so on. The dashed line represents the assumptive minimal detectable SNR level. The harmonics orders above the dashed line can be retrieved after reconstruction.

Similar plots for STED-SIM are presented in figure 2.10 [51]. The solvable harmonics order can keep expanding with increased STED power. Theoretically, the resolution improvement for STED-SIM is unlimited. The better performance in STED-SIM comes from the low shot noise and strong nonlinear effect due to the STED quenching effect.

The properties of darker shot noise, weaker photon bleaching and theoretical unlimited resolution of the STED nonlinear effect makes the STED-SIM to be a potential better alternate nonlinear SIM technique than Saturated-SIM.

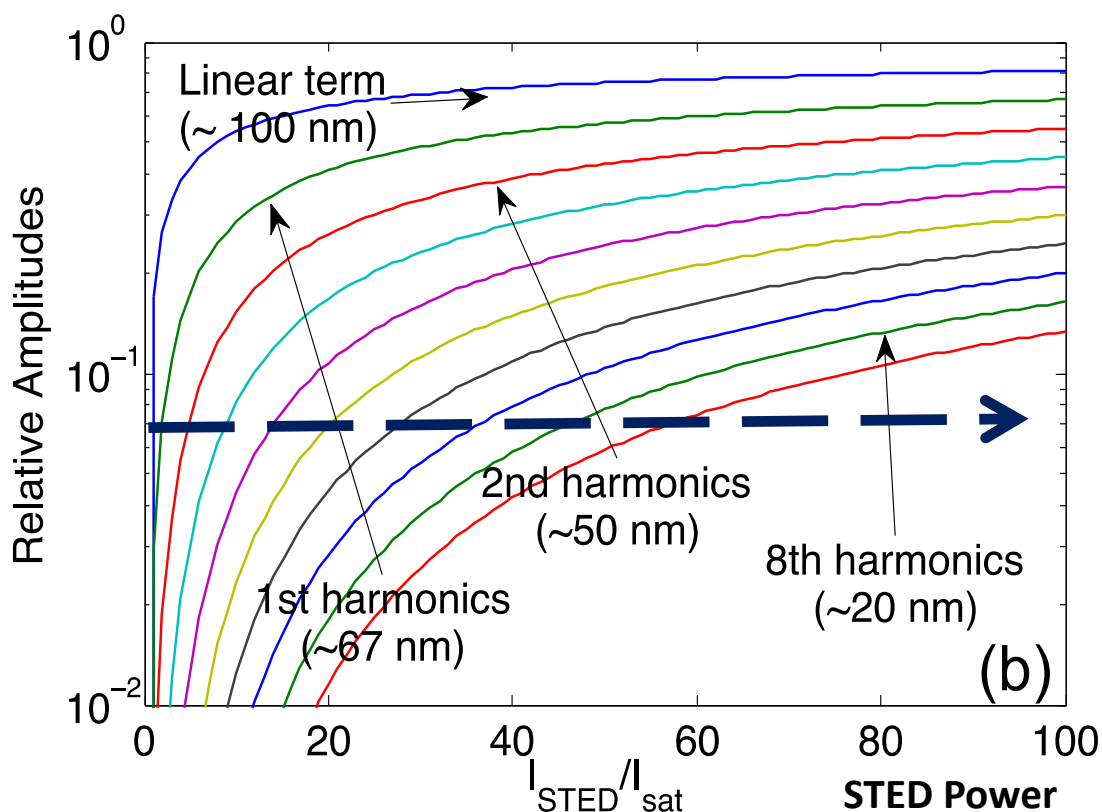


Figure 2.10 The strength of STED-SIM nonlinear high order harmonics as STED power increases. Different colors of the curves represent varied harmonics orders: blue for linear term, green for 1st harmonics order, red for 2nd harmonics order and so on. The dashed line represents assumptive minimal detectable SNR level.

2.4.2 Comparison between STED-SIM and Photoswitchable-SIM

Another demonstrated nonlinear SIM technique employs the nonlinearity in the photon switching process to produce patterned illumination [33]. It has similar ‘turn off’ effect as we mentioned in STED-SIM. Besides shot noise, both STED-SIM and Photoswitchable-SIM have switching noise when turning on/off fluorophores. In STED-SIM, the fluorophore switch is a per excitation/emission cycle process which happens thousands time during one frame exposure. The switching noise is negligible after the summation of emission signal in one exposure. However,

in Photoswitchable-SIM, the fluorophore switch happens one time per frame which brings significant noise into the final image. Figure 2.11 (a-b) illustrates the advantage of STED-SIM in eliminating stochastic noise. 50 particles per unit length is assumed in figure 2.11 (a). Besides, STED-SIM is a faster imaging technique compared with Photoswitchable-SIM, which requires minutes to achieve one superresolution image. Therefore, STED-SIM makes a better nonlinear approach than Photoswitchable-SIM for its fast imaging speed and negligible switching stochastic noise.

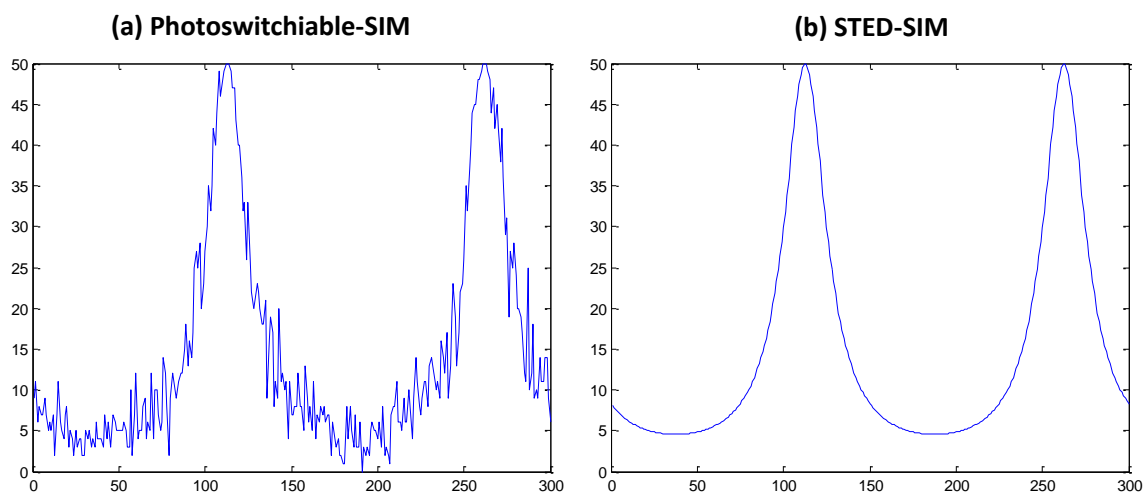


Figure 2.11 Stochastic noises in photoswitchable-SIM. (a) The nonlinear structured illumination in photoswitchable-SIM. Assume 50 particles per unit length. (b) Stochastic noises are removed after the summation of thousands of cycles in STED-SIM.

2.5 Summary

Structured illumination microscopy is currently the most practical superresolution imaging technique. Combining with a strong nonlinear effect, nonlinear SIM achieves resolution far beyond diffraction limit. We theoretically demonstrated that the STED-SIM provides a better

nonlinear SIM approach than Saturated-SIM and Photoswitchable-SIM because of its fast imaging speed, negligible stochastic noise during switch process, low shot noise and theoretically unlimited resolution. The reconstruction algorithm of STED-SIM will be discussed in next chapter.

Chapter 3 Algorithm Development and Feasibility Study of STED-SIM

In this chapter, the algorithm for STED-SIM superresolution reconstruction is developed. Different from previous nonlinear SIM, instead of applying one dimensional interference pattern, 2D grid interference pattern is employed to maximize the imaging speed by removing pattern rotation. By simulating the STED-SIM image acquisition and processing in 1D, the influence of STED power and interference contrast to final reconstructed image quality is studied. The feasibility of STED-SIM with commercial available laser source is validated by 2D STED-SIM simulation.

3.1 STED-SIM superresolution image reconstruction algorithm development

As mentioned in chapter 2, STED-SIM is in theory a better alternate technique than Saturated-SIM and Photoswitchable-SIM due to fast imaging speed, negligible switching stochastic noise, low shot noise, and theoretical unlimited resolution, which makes it a promising superresolution fluorescence microscopy approach among the current available approaches. In this chapter, the mathematical algorithm of the STED-SIM superresolution reconstruction process will be deduced and the simulation of 1D and 2D STED-SIM reconstruction will be performed to study the influence of varied experiment condition, such as STED power and interference contrast.

The algorithm of linear SIM reconstruction is studied firstly to help understand the complicated STED-SIM image reconstruction. After performing a linear patterned illumination on the sample, the illuminated sample can be described as the multiplication of the sample and the illumination pattern, in spatial domain as depicted in Eq. (3.1). Final observed image will be formed after

convolving the illuminated sample with the point spread function (PSF) of the imaging system, as depicted in equation (3.2).

$$Em(x) = Sample(x) \times Illumination(x) \quad (3.1)$$

$$Image(x) = (Sample(x) \times Illumination(x)) \otimes PSF(x) \quad (3.2)$$

where, x is the spatial position and sample expresses the fluorophore distribution. Illumination, PSF, Em and $Image$ are the illumination pattern, point spread function, illuminated object and final observed image, respectively.

Eq. (3.3-3.4) shows the image forming process in spatial frequency domain: the final image in frequency domain is equal to the sample convolve with the illumination in frequency and then multiplied by optical transfer function (OTF) of the imaging system.

$$Em(\epsilon) = Sample(\epsilon) \otimes Illumination(\epsilon) \quad (3.3)$$

$$Image(\epsilon) = (Sample(\epsilon) \otimes Illumination(\epsilon)) \times OTF(\epsilon) \quad (3.4)$$

Where ϵ is the spatial frequency.

For linear SIM, the illumination can be formed by two beam interference [52] and expressed as Eq. (3.5). Eq. (3.6) depicts the Fourier transform of Eq. (3.5) and consists of three shifted delta functions. The Fourier domain expression of Eq. (3.4) is shown in Eq. (3.7), which contains one non-shifted and two shifted sample information in frequency domain (Eq. (3.7)). Reconstruction of high resolution image can be realized by solving those three unknowns- $Sample(\epsilon)$, $Sample(\epsilon + k_0)$ and $Sample(\epsilon - k_0)$, where k_0 is the spatial frequency of the pattern period. In

order to solve those unknowns, three different equations are required. Multiple images can be acquired with illumination pattern with different phases, which provide equations in Fourier domain as expressed in Eq. (3.7-3.8) (φ_1, φ_2 are the varied phases of illumination pattern). With those equations, the information solved in frequency domain can reach the spatial frequency beyond diffraction limit and therefore lead to superresolution image.

$$\text{Illumination}(x) = 1 + \cos(2\pi k_0 x) \quad (3.5)$$

$$\text{Illumination}(\varepsilon) = \delta(\varepsilon) + \frac{1}{2}\delta(\varepsilon - k_0) + \frac{1}{2}\delta(\varepsilon + k_0) \quad (3.6)$$

$$\text{Image}_1(\varepsilon) = (\text{Sample}(\varepsilon) + \frac{1}{2}\text{Sample}(\varepsilon + k_0) + \frac{1}{2}\text{Sample}(\varepsilon - k_0)) \times \text{OTF}(\varepsilon) \quad (3.7)$$

$$\text{Image}_2(\varepsilon) = (\text{Sample}(\varepsilon) + \frac{1}{2}e^{i\varphi_1}\text{Sample}(\varepsilon + k_0) + \frac{1}{2}e^{-i\varphi_1}\text{Sample}(\varepsilon - k_0)) \times \text{OTF}(\varepsilon) \quad (3.8)$$

$$\text{Image}_3(\varepsilon) = (\text{Sample}(\varepsilon) + \frac{1}{2}e^{i\varphi_2}\text{Sample}(\varepsilon + k_0) + \frac{1}{2}e^{-i\varphi_2}\text{Sample}(\varepsilon - k_0)) \times \text{OTF}(\varepsilon) \quad (3.9)$$

In the above equations, as described in chapter 2, the effective illumination in STED-SIM can be calculated by equation

$$\text{Illumination}(x) = \frac{1}{1+C \times (1+\cos(2\pi k_0 x))} \quad (3.10)$$

The Fourier transform of this nonlinear patterned illumination is expressed in Eq. 3.11, which contains delta functions with further shifts in frequency domain. C_i represents the constant ratio for various delta functions. The frequency information contained in the image with nonlinear patterned illumination (Eq. 3.12) is higher compared with the information in the image acquired with linear patterned illumination (Eq. 3.7). In the nonlinear case, the number of the frames with

different phase required is decided by the harmonic order tried to be solved, following the relation of Eq. 3.13 (where $N_{equation}$ is the number of equation required and N_{order} is the harmonic order to be solved).

$$\begin{aligned} \text{Illumination}(\varepsilon) = & C_0\delta(\varepsilon) + C_{-1}\delta(\varepsilon - k_0) + C_1\delta(\varepsilon + k_0) + C_{-2}\delta(\varepsilon - 2k_0) + C_2\delta(\varepsilon + 2k_0) + \\ & C_{-3}\delta(\varepsilon - 3k_0) + C_3\delta(\varepsilon + 3k_0) + \dots \dots \end{aligned} \quad (3.11)$$

$$\begin{aligned} \text{Image}_n(\varepsilon) = & (C_0\text{Sample}(\varepsilon) + C_1e^{i\varphi_n}\text{Sample}(\varepsilon + k_0) + C_{-1}e^{-i\varphi_n}\text{Sample}(\varepsilon - k_0) + \\ & C_2e^{i2\varphi_n}\text{Sample}(\varepsilon + 2k_0) + C_{-2}e^{-i2\varphi_n}\text{Sample}(\varepsilon - 2k_0) + \dots \dots) \times \text{OTF}(\varepsilon) \end{aligned} \quad (3.12)$$

$$N_{equation} = 2 \times N_{order} + 1 \quad (3.13)$$

One dimensional patterned illumination was previously employed for 2D structured illumination microscopy. The 1D pattern was shifted in one dimension to acquire the high spatial frequency information in that direction and then rotated by an angle to retrieve the information in another direction, as shown in figure 3.1 (a) and (d). After a 180 degree rotation, the full 2D frequency information for a high resolution image can be acquired [53]. However, the speed of the rotation process is much slower than the shifting process which limits the imaging speed of the system. In our experiment, we chose the Piezo stages to drive the 2D STED pattern to perform nonlinear SIM. Figure 3.1 (b) presents the two incoherently superimposed orthogonal STED interference patterns. Combined with a uniform excitation, the effective illumination pattern is simulated and shown in figure 3.1 (c). During the data acquisition, the 2D grid pattern was shifted only by piezo stages, of which the shifting time is negligible, and the speed of the super-resolution imaging is only limited by the rate of photon registration. The Fourier domain patching obtained

with this 2D nonlinear structured illumination is presented in figure 3.1 (e) compared with the one obtained with 1D patterned illumination (figure 3.1 (d)).

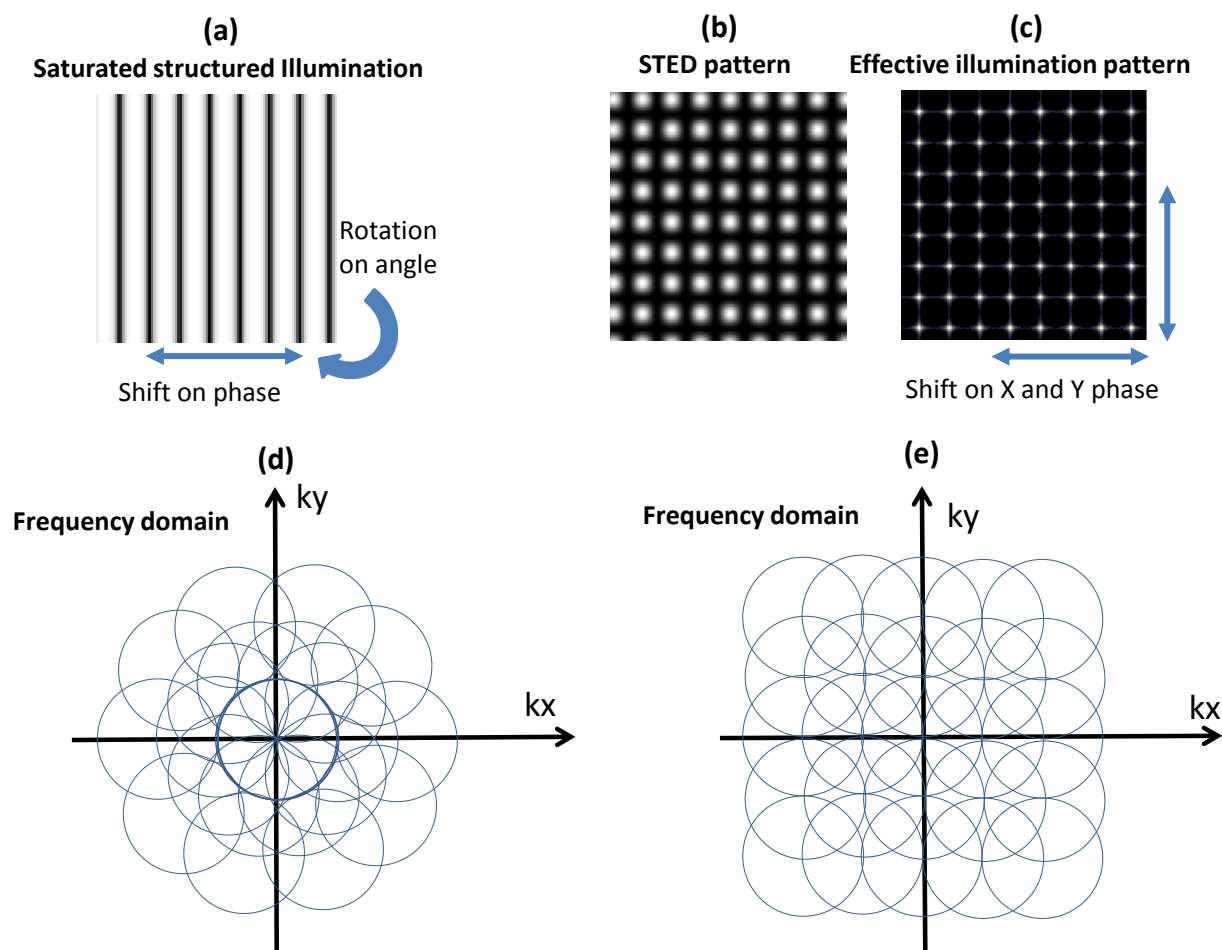


Figure 3.1 (a) 1D saturated structured illumination. (b) 2D STED interference pattern. (c) Effective nonlinear illumination pattern after an emission filter with the combination of a linear 2D STED pattern and a uniform excitation. (d) 2D frequency domain image patching during superresolution reconstruction with 1D structured illumination. (e) 2D frequency domain image patching during superresolution reconstruction with our 2D grid pattern.

Figure 3.2 illustrates the image acquiring and processing steps. A simulated object and corresponding diffraction limit image are presented in figure 3.2 (a) and (f). The two separated

horizontal lines cannot be distinguished in diffraction limit image since the distance between lines is below the resolution of imaging system. With our STED-SIM, the same simulated object is illuminated by 2D nonlinear pattern (figure 3.1 (c)) and results in raw images (figure 3.2 (b)). A set of frames are acquired with several different pattern phases. After image processing in Fourier domain, different frequency components can be solved and patched to the final Fourier domain image (figure 3.2 (c-d)). After the final step of inverse Fourier transform, the spatial domain image with superresolution can be acquired as shown in figure 3.2 (e). Two horizontal lines can be clearly separated and the reconstructed circle object proves the free of directional artifacts for STED-SIM reconstruction.

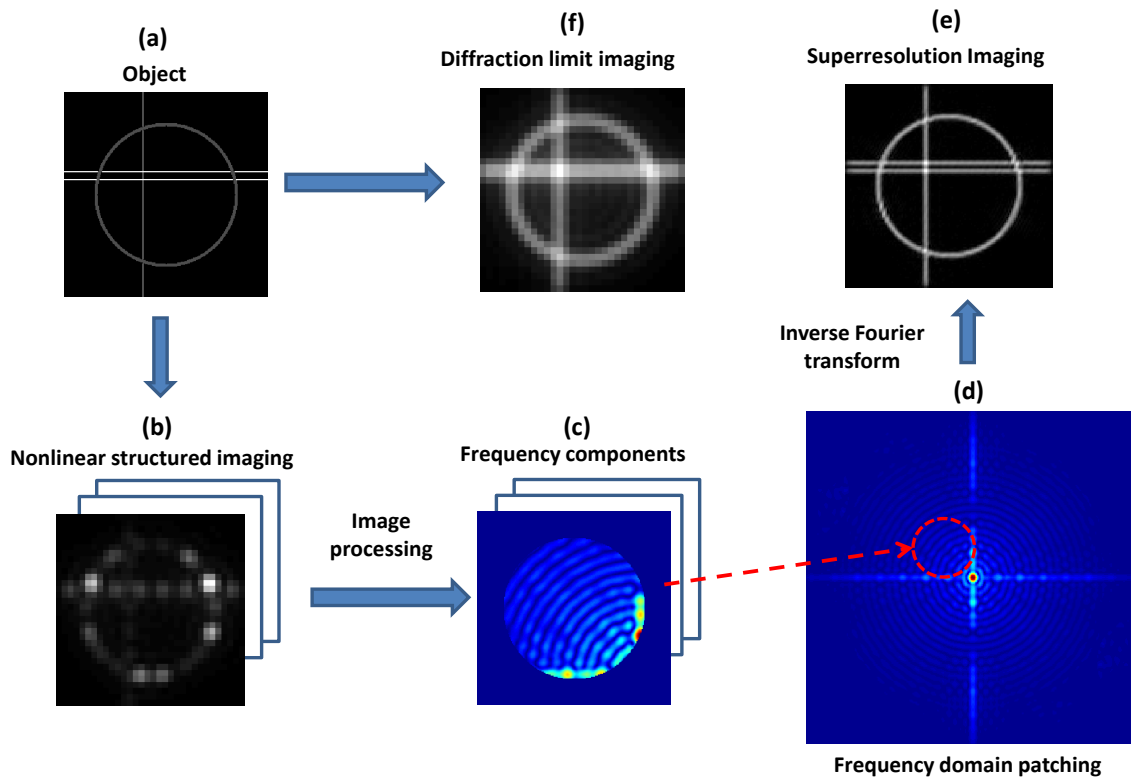


Figure 3.2 (a) Simulated object. (b) Simulated raw images after excited by structured illumination with varied phases. (c) Fourier components in different frequency domain after image processing. (d) Reconstructed image in frequency domain. (e) Superresolution image in spatial domain. (f) Simulated diffraction limit image from object in (a).

3.2 STED-SIM superresolution reconstruction simulation

3.2.1 Simulation on 1D STED-SIM superresolution reconstruction to study the influence of STED power and interference contrast

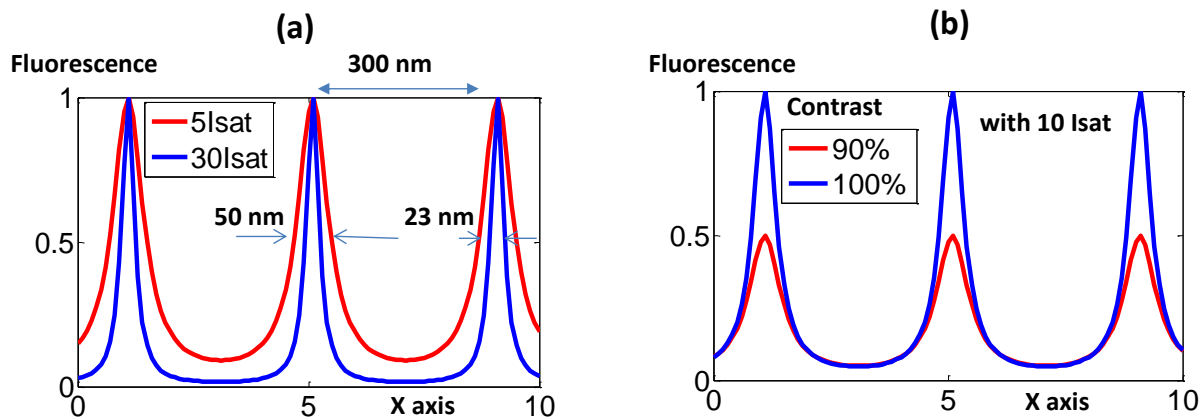


Figure 3.3 (a) STED nonlinear structured illuminations with STED powers of 5 Isat and 30 Isat, respectively. (b) STED nonlinear structured illuminations with interference contrasts of 90% and 100%, respectively. STED power is set to be 10 Isat.

Two of the major factors that determine the resolution of STED-SIM are average STED power and interference contrast. As presented in figure 3.3 (a), two effective nonlinear illumination patterns are plotted under the condition of perfect interference (100% interference contrast) and different STED powers. The FWHM of the effective illumination with 5 Isat STED power pattern (red curve) and 30 Isat STED power pattern (blue curve) are 50 nm and 23 nm, respectively. Isat is saturation intensity that presents the STED power which quenches the

fluorescence emission to the half of maximum. For fixed signal noise ratio, the FWHM of the effective illumination pattern is the indicator of nonlinear SIM-SIM system resolution since it represents the smallest area which can be illuminated. In figure 3.3 (b), the average STED power is set to be $10 I_{\text{sat}}$, and the interference contrasts are set at two different values shown with red curve (90%) and blue curve (100%), respectively. The simulation results show that the low interference contrast would significantly decrease the effective illumination strength and therefore lead to performance with low signal noise ratio. Therefore, high STED power and high interference contrast are favorable for obtaining STED-SIM with better imaging resolution.

To test the STED-SIM reconstruction algorithm, the 1D imaging reconstruction process is simulated and the simulation results are shown in figure 3.4. The simulated objects are the 10 nm particles with separations of 30 nm, 40 nm, 50 nm and 300 nm, respectively. The signal strength is 500 photons per pixel at the particle center without STED quenching. The simulated diffraction limit imaging results are shown in figure 3.4 (b) with diffraction limit resolution of 250 nm. As expected, only the peaks with 300 nm particle distance can be resolved. Two different contrasts of 90% and 95% are both considered when simulating the imaging process with the STED-SIM algorithm described above. In this simulation, 13 frames with different phases are combined to solve the high order harmonics to the 6th order under the circumstance with shot noise and readout noise. As shown in figure 2 (c-d), the particles with 40 nm spacing can barely be resolved, which is in correspondence with the predicted results considering the low signal level and the particle size. Higher interference contrast provides better reconstructed image quality. The reconstructed image in figure 3.4 (d) presents more artifacts than the image in figure 3.4 (c). This 1D simulated result validated our STED-SIM reconstruction algorithm.

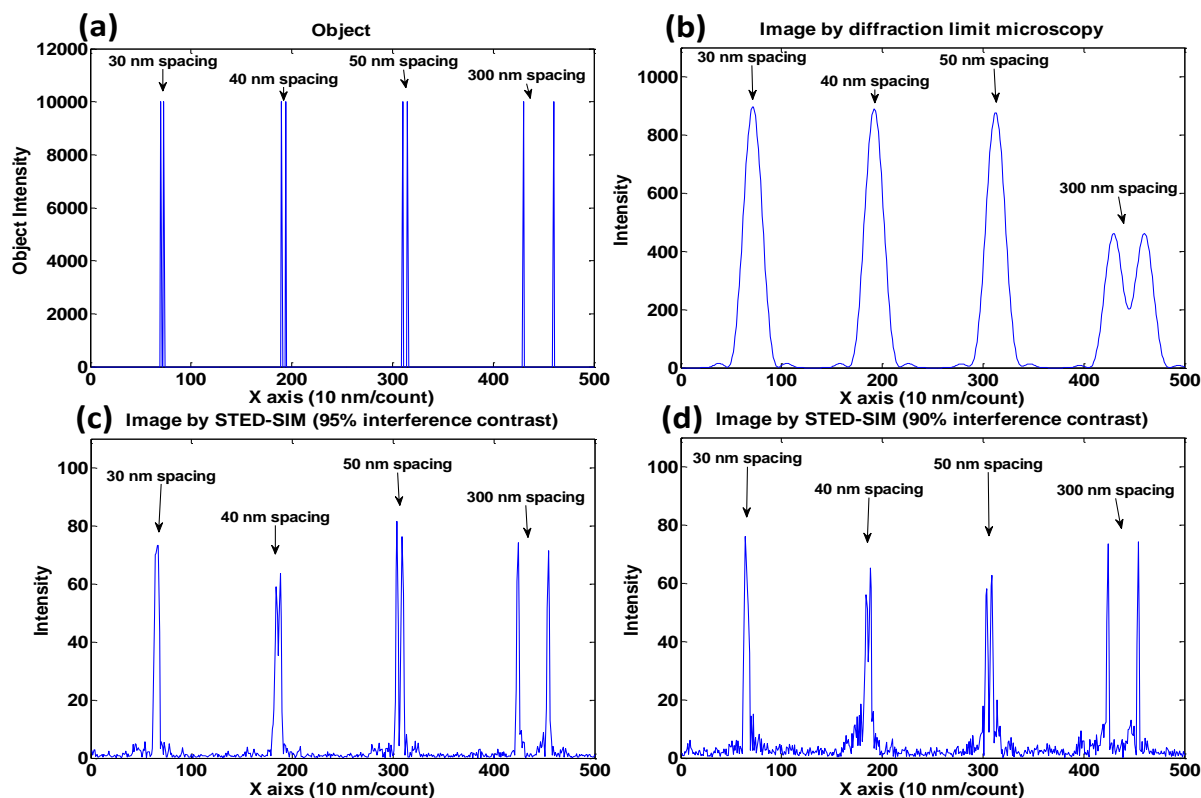


Figure 3.4 (a) One dimensional simulated object. Those simulated particles have the separations of 30 nm, 40 nm, 50 nm and 300 nm. (b) Simulated diffraction limit image from object in (a). (c) Simulated 1D STED-SIM reconstructed image with 95% contrast from object in (a). (d) Simulated 1D STED-SIM reconstructed image with 90% contrast from object in (a).

3.2.2 2D simulation with commercial available laser power to predict the feasibility of STED-SIM

In this section, theoretical study with the aforementioned model will be discussed when considering the actual experiment condition. The commercial available laser source can provide 5 Isat average STED power on the $10 \times 10 \mu\text{m}^2$ field of view. The performance of the superresolution imaging system is simulated under this condition. A 2D simulated object is presented in figure 3.5 (a). The objects are the 12 nm wide bars with separations of 24 nm, 36 nm,

48 nm, 60 nm and 72 nm, respectively. The circle object is utilized to test the directional artifacts of the reconstructed image. The average STED power is set to be $5 I_{\text{sat}}$ and the interference is 95% in the simulation, which can be achieved practically. Considering our 660 nm working wavelength and objective with an NA of 1.49, the diffraction limit resolution of the imaging system is 300 nm. As we expected, no separated targets can be resolved in the simulated diffraction image (figure 3.5 (b)), while in the 2D STED-SIM reconstructed image, 60 nm resolution of the system under such experimental condition can be realized with no directional artifacts. The simulated result shows a 5-fold resolution improvement with our STED-SIM approach compared with traditional diffraction limit microscope.

3.2.3 Study of the performance of STED-SIM with a field enhancement mechanism by two dimensional simulation

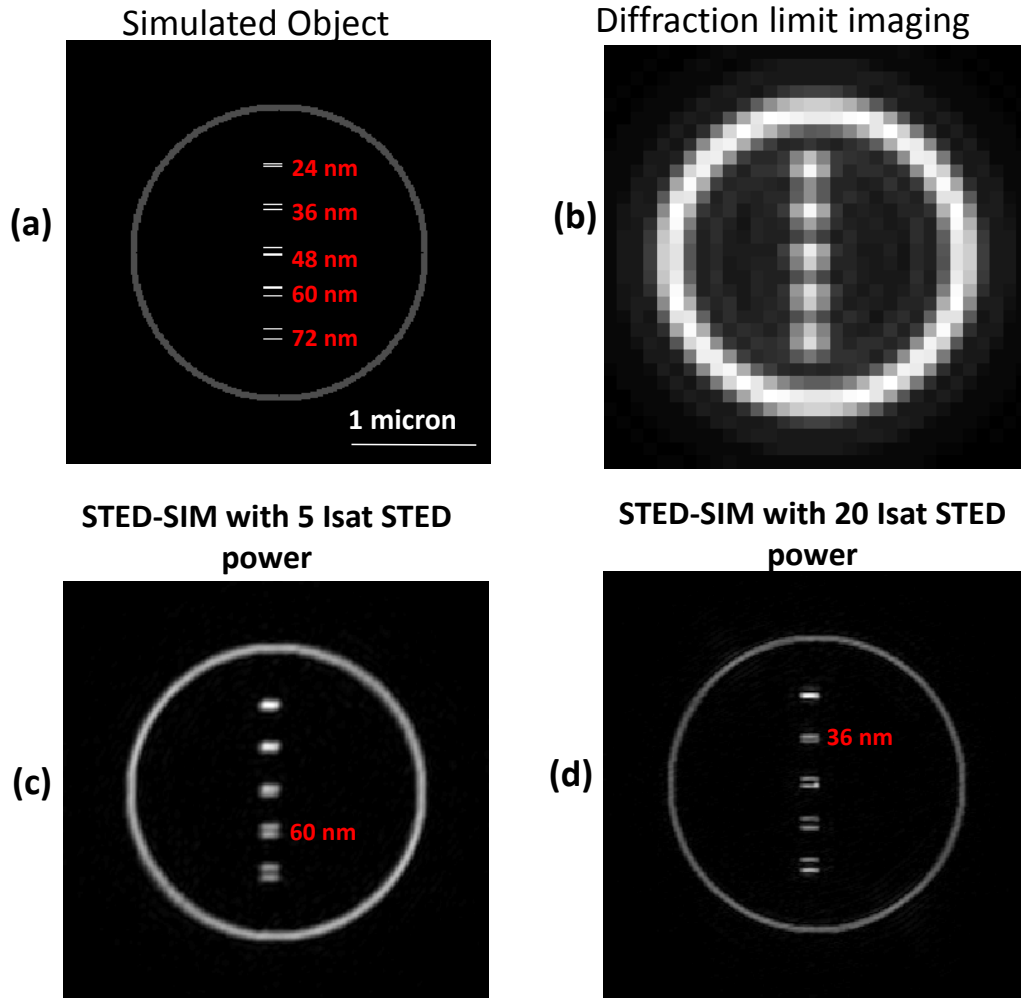


Figure 3.5 (a) Two dimensional simulated object. Those simulated bars have the separations of 24 nm, 36 nm, 48 nm, 60 nm and 72 nm. (b) Simulated diffraction limit image from object in (a). (c) Simulated 2D STED-SIM reconstructed image with 95% interference contrast and 5 Isat average power from object in (a). (d) Simulated 2D STED-SIM reconstructed image with 95% interference contrast and 20 Isat average power from object in (a).

The available power from the commercial laser limits the performance of our STED-SIM system. To further improve the STED-SIM resolution, a field amplifying mechanism is required to work with current laser source. If the average STED power can reach $20 I_{\text{sat}}$ over full field of view, the resolution of our STED-SIM technique can reach 36 nm as simulated in figure 3.5 (d). A potential mechanism widely used for field enhancement is Surface Plasmon Resonance (SPR) [54]. The details of this mechanism and its application in our STED-SIM will be presented in detail in chapter 4.

3.3 Summary

In this chapter, the STED-SIM image processing algorithm is developed mathematically. Differ from other nonlinear SIMs, the combination of a 2D STED patterned field and a uniform excitation field is required to generate nonlinear structured illumination. With this illumination design, the imaging speed of our STED-SIM technique will only be limited by camera speed. Our STED-SIM algorithm is verified by the 1D image reconstruction simulation. Considering the practical $5 I_{\text{sat}}$ average power with commercial laser source and 300 nm diffraction limit resolution, encouraging imaging resolution of 60 nm is predicted by our 2D STED-SIM simulation. Moreover, after introducing a field enhancing mechanism, the resolution can be further enhanced to 36 nm with the STED-SIM technique in theory. Details of such amplifying mechanism will be discussed in chapter 4.

Chapter 4 Surface Plasmon Resonance (SPR) enhanced STED-SIM

In this chapter, a field enhancement mechanism, surface plasmon resonance (SPR), is introduced to our STED-SIM system in the effort of reaching 30 nm imaging resolution. The SPR field enhancement effect is firstly predicted by field calculation and simulation. The experimental test shows that the SPR mechanism provides 8 times stronger quenching effect for STED beam to turn off the excited fluorophores. With a 50-mW STED beam, $10 I_{SAT}$ over a $17 \times 10 \mu m^2$ area or $14 I_{SAT}$ over an $11 \times 6.5 \mu m^2$ area were achieved on an optimal SPR structure of 40-nm sliver and 15-nm SiO₂. The introducing of SPR enhancement to STED-SIM system provides better than 50 nm resolution in some region but fails to achieve improved superresolution in full field because of the propagation of the SPR field along the interface and the distortion of interference field.

4.1 SPR enhancement

4.1.1 Introduction to SPR field enhancement mechanism

As discussed in previous chapter, in full-field STED-SIM, a stronger STED nonlinear effect is highly desirable. In current traditional point-scanning STED microscopy, the STED beam is tightly focused to a donut-shape spot [55]. With small focused beam size, the STED field intensity can reach $200 I_{sat}$ and lead to the extreme superresolution of 8 nm [34]. The typical value for I_{sat} is $3 \sim 10 \text{ MW}/\text{cm}^2$ [56]. In our full-field STED-SIM, the size of the STED field illuminated on the sample stage reaches to the area of $10 \times 10 \mu m^2$, which is hundred times larger than that of point-scanning STED. With our current commercial laser source, the STED field intensity is around $5 I_{sat}$ over full-field view, which has a predicted 60 nm resolution in

simulation. In order to further improve the resolution, an enhancement mechanism has to be employed so that the STED intensity can reach up to $20 I_{\text{sat}}$ over $10 \times 10 \mu\text{m}^2$ field of view.

Surface plasmon resonance (SPR) is a widely used technique for enhancing the electric field [54, 57, 58]. SPR enhanced Raman, fluorescence and two-photon fluorescence have been previously reported [59-63]. Surface plasmons are coherent electron oscillations that exist at the interface between two materials where the real part of the dielectric function has different sign across the interface. A typical structure for exciting laser introduced surface plasmons, Kretschmann configuration, is shown in figure 4.1 [64]. When a laser beam is incident from one side of a dielectric-metal dielectric structure, at the interface of the other side of metal, the surface plasmons can be excited. And the resonance of the surface plasmons will be introduced when the laser beam is at a specific critical incident angle. The electric field intensity of the SPR can be tens of times stronger compared with incident light. By employing the SPR enhancement mechanism, the STED nonlinear effect can be further strengthened with our current laser source.

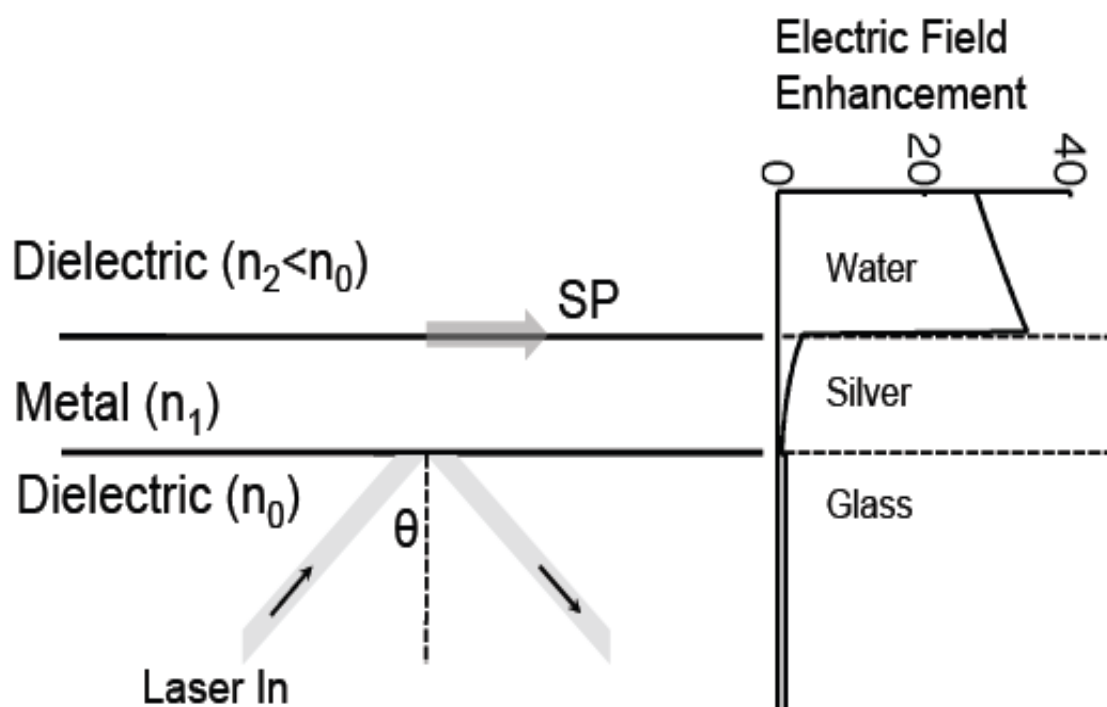


Figure 4.1 Laser introduced surface plasmons and electric field enhancement of surface plasmon resonance.

4.1.2 Multilayer thin film to generate SPR

In our effort of achieving SPR enhancement on STED quenching effect, the Kretschmann configuration is applied. The first dielectric in our approach is glass (coverslip) and the second dielectric is water (cell medium). The metal chosen to generate the SPR is silver [65], due to the working wavelength is in the range of visible wavelength (gold for infrared light). Although the electric field of SPR is enhanced by tens of times, it is an evanescent field the intensity of which decays exponentially along the axis perpendicular to the interface between dielectric and metal, as shown in blue line plotted in figure 4.2 (b). This feature limits the experiments to be performed on the surface of the metal. However, the fluorescent emission will be absorbed by the metal when the fluorophore is attached on the metal as illustrated in figure 4.2 (a). This

quenching effect is due to the energy transfer between fluorophore and metal. And the emission strength from the fluorophore is then proportional to $1/(1 + \frac{d_0^4}{d^4})$, where d is the distance from the metal surface and d_0 is a constant relative to the metal and fluorophore character. The relation between fluorophore emission and distance from metal surface is plotted in figure 4.2 (b), red curve. The half quenching distance between a fluorophore and an ideal metal surface is estimated to be 10~15 nm [66]. Considering the exponential decay of evanescent field and the fluorescent quenching from metal, there is a balance on the distance from the sample to the metal. Silicon dioxide film is coated on top of silver to control the distance between sample and metal, and protect the metal film from oxidization. The final structure in our experiment to generate SPR is glass-silver-SiO₂-water multilayer as shown in figure 4.5 (inset).

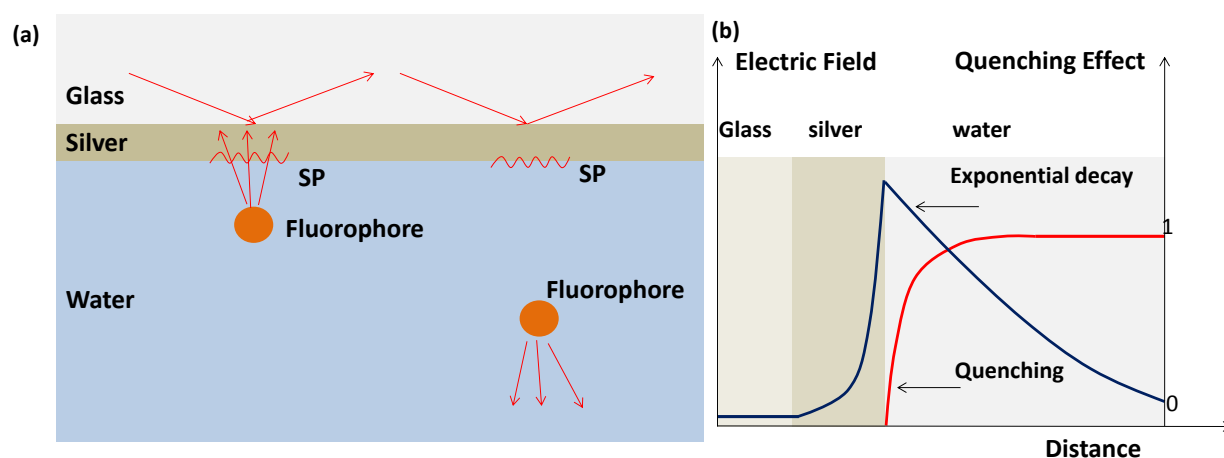


Figure 4.2: (a) Fluorescence quenching due to the absorption of metal. (b) The exponential decay of SPR evanescent field (blue curve) and the relative fluorescence emission from the fluorophore after the quenching of metal absorption (red curve).

4.1.3 12 times of field enhancement from SPR by field calculation

The simulation of surface plasmon resonance enhancement has been performed to optimize the thickness of different layers. Considering the SiO₂ layer that separates the silver and fluorophores is much thinner than a wavelength, the optical property of our glass-silver-SiO₂-water multilayer can be simulated with glass-silver-water multilayer. Considering three-layer structure, the reflectivity R for p-polarized light (SPR cannot only be generated by s polarized light), with E₀ the incoming and E_r the reflected field is given by

$$R = |r_{012}^p|^2 = \left| \frac{E_r^p}{E_0^p} \right|^2 = \left| \frac{r_{01}^p + r_{12}^p \exp(2ik_{z1}d)}{1 + r_{01}^p r_{12}^p \exp(2ik_{z1}d)} \right|^2 \quad \text{with } r_{ik}^p = \left(\frac{k_{zi}}{\epsilon_i} - \frac{k_{zk}}{\epsilon_k} \right) / \left(\frac{k_{zi}}{\epsilon_i} + \frac{k_{zk}}{\epsilon_k} \right)$$

Where k is the wave vector and z axis is perpendicular to the interface. d is the thickness of metal and ε is the dielectric function. SPR is only generated by p-polarized light. When the reflectivity is at its lowest value, the intensity of electromagnetic field is at its maximum at the surface of the other side of metal. The value of enhancement T is given by, for p-polarized light:

$$T = |t_{012}^p|^2 = \left| \frac{t_{01}^p t_{12}^p \exp(ik_{z1}d)}{1 + r_{01}^p r_{12}^p \exp(2ik_{z1}d)} \right|^2$$

$$t_{ik}^p = 1 + r_{ik}^p$$

The plots in figure 4.3 (a) presents the electric field enhancement against silver thickness. Two conditions are considered: parallel beam with single wavelength (ideal) and focused Gaussian beam with broadband wavelength (practical). The wavelength utilized in simulation is 680 nm and 680 nm- 730 nm respectively. For focused beam simulation, the power of the laser beam follows Gaussian distribution against incident angle with standard deviation of 2 degrees. As demonstrated in figure 4.3 (a), with the silver thickness of 40 nm, the enhancement of electric

filed is at its maximum of 12 times compared with incident beam. The critical incident angle to generate the SPR is also simulated and presented in figure 4.3 (b). An incident angle around 70 degrees is required.

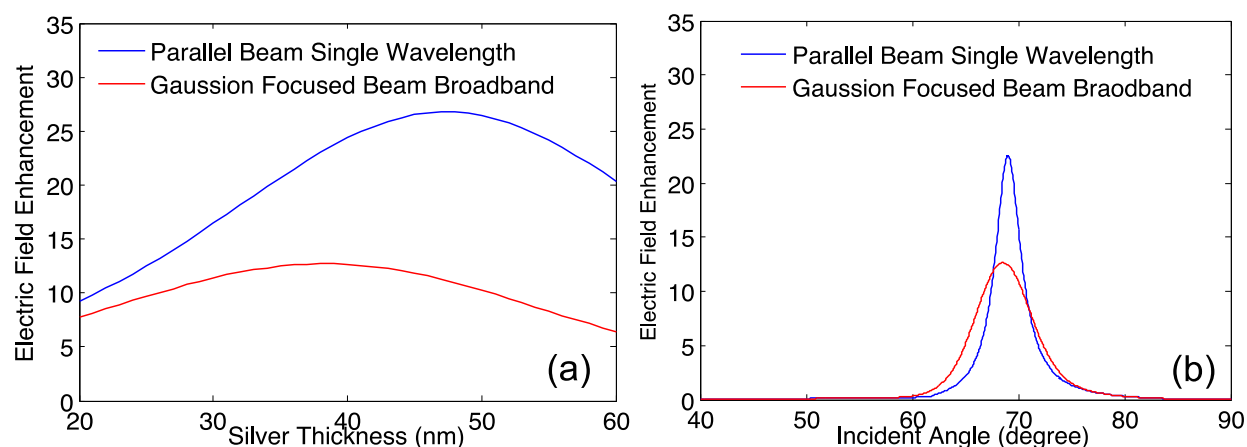


Figure 4.3: (a) Electric field enhancement against silver thickness. (b) Electric field enhancement against incident angle. The blue plot is from parallel beam single wavelength simulation and the red one is from Gaussian focused beam with broadband wavelength [51].

4.2 SPR enhanced STED effect experiment

4.2.1 Multilayer thin films fabrication by electron beam vapor deposition

In experiments, the multilayer film, 40 nm silver (optimized by simulation) and 15 nm SiO₂ (optimized by experiments as listed in table 4.1), was coated by electron beam physical vapor deposition (BOC Edwards Auto 306 E-beam Evaporator). To generate uniform SPR field, smooth film surface is strictly required. Two types of substrates were tested: preclean coverslip (Fisherbrand premium cover glass) and piranha washed preclean coverslip. The protocol of piranha wash process is listed in appendix. AFM images of different substrate type were taken

before and after thin films coating. The results are shown in figure 4.4: piranha wash is necessary to achieve smoothest film surface, whose surface roughness is 0.9 nm RMS after thin film coating.

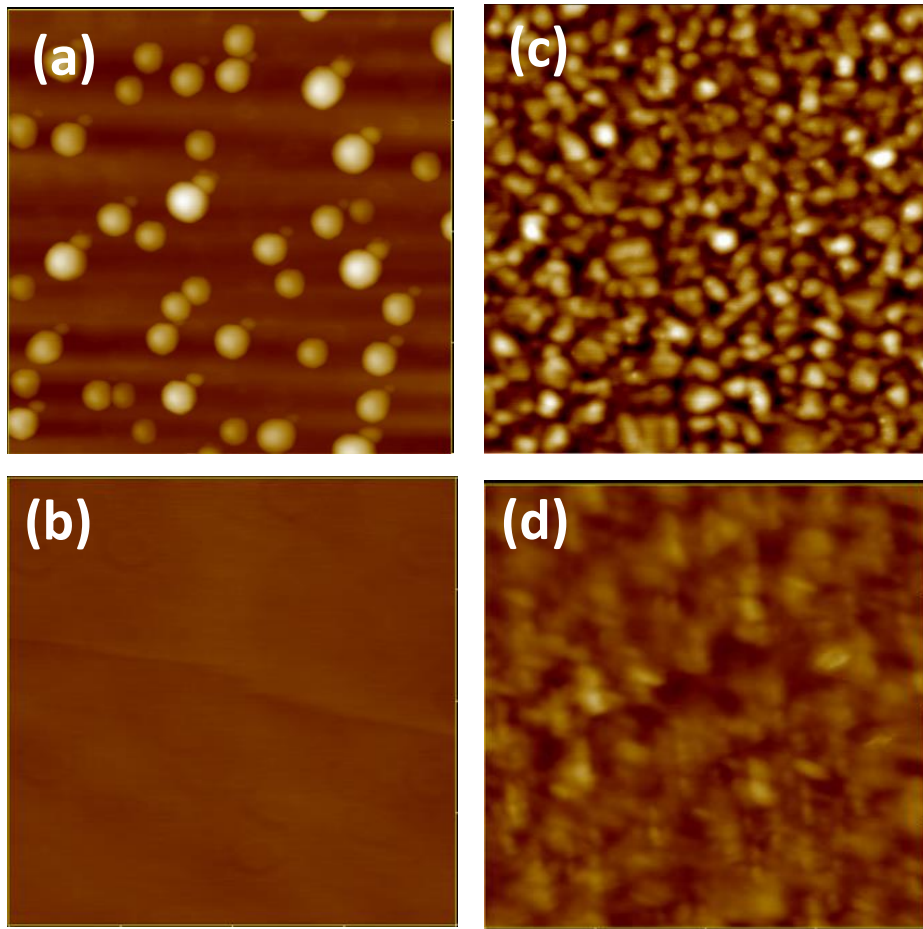


Figure 4.4 AFM image of (a) preclean coverslip surface, (b) preclean coverslip surface after piranha wash, (c) 40 nm silver and 15 nm SiO₂ coating on top of preclean coverslip and (d) 40 nm silver and 15 nm SiO₂ coating on top of piranha washed preclean coverslip. The field of view of each image is $1 \times 1 \mu\text{m}^2$. The RMS of the surface roughness is (a) 4.9 nm, (b) 0.2 nm, (c) 3.2 nm and (d) 0.9 nm.

4.2.2 8 times STED quenching effect enhancement by SPR in experiments

After acquiring high quality multilayer substrates, to test the SPR enhancement experimentally, a STED-TIRF (TIRF refers to total internal reflection) setup was built to examine STED effects with and without SPR. Figure 4.5 shows a sketch of the optical setup. A supercontinuum pulsed laser (Fianium SC-450-PP-HE) with pulse duration < 350 ps was utilized to generate both the excitation and STED beams. The excitation beam was filtered by a 615 ± 15 nm bandpass filter (Semrock FF01-630/20-25, tilted) and attenuated to the power of 3 mW. The STED beam was filtered by a 705 ± 25 nm bandpass filter (Semrock FF01-716/40-25, tilted). A delay stage was placed in excitation beam path to control the arrival time of the STED pulse to match the excitation pulse, so the STED effect could be maximized. As we discussed before, SPR can only be generated by the p-polarized incident light, a polarized beam splitter and a half wave plate were employed to ensure that only the p-polarized STED beam is passed onto the sample. The fluorescent sample was ATTO 633 (the spectrum of ATTO 633 is illustrated in figure 4.6) water solution at $100 \mu\text{g/ml}$ with anti-fading agent (ProLong Gold, Invitrogen), placed on top of a silver-SiO₂ coated coverslip. SPR is launched in the Kretschmann configuration, as shown in the inset of figure 4.5. Spontaneous emissions of the fluorophores were recorded by a 15X microscope with a CCD camera (Thorlabs DCU223M) through a 660 ± 10 nm filter (Semrock FF01-661/20), which removed stray excitation and STED light.

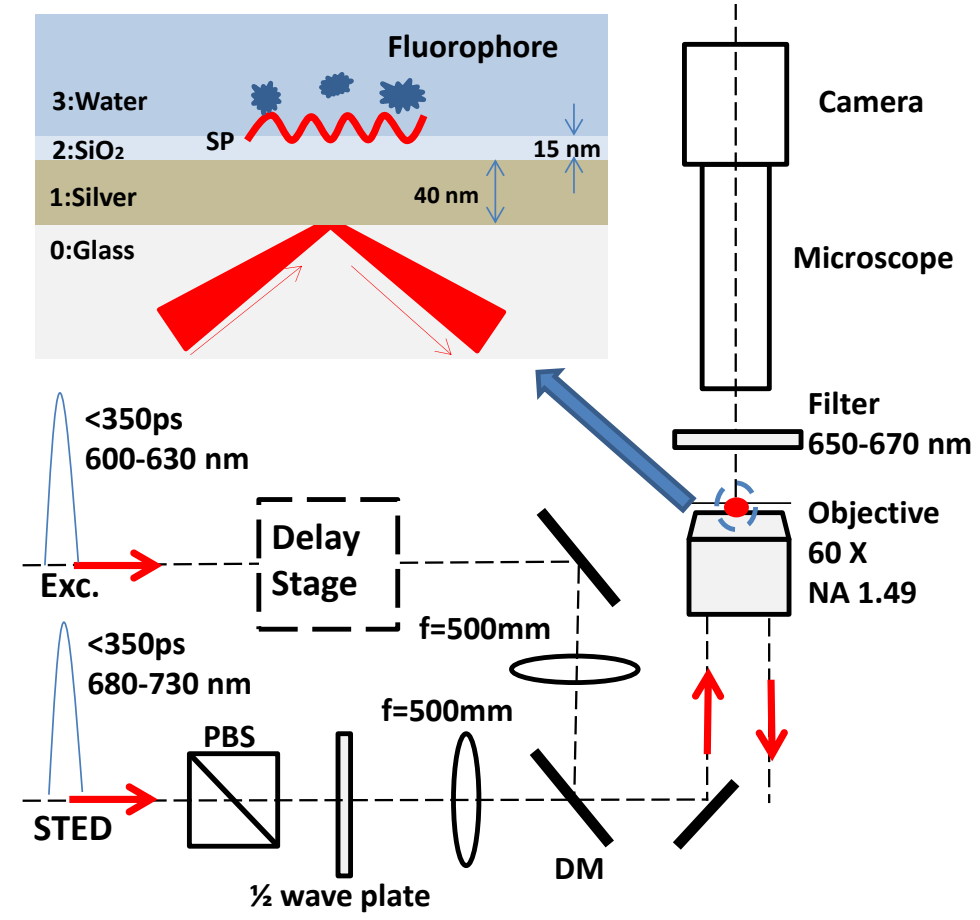


Figure 4.5 TIRF-STED setup for measuring SPR enhanced STED effect. PBS: Polarized beam splitter. DM: Dichroic mirror. The inset is the multilayer structure to generate SPR enhanced STED effect [51].

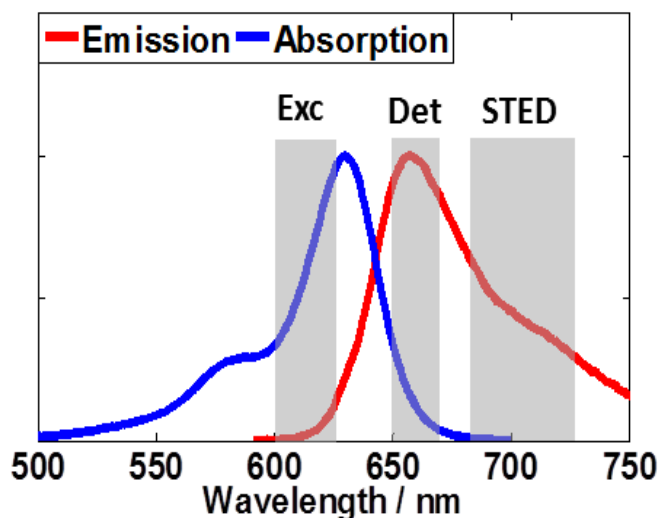


Figure 4.6 ATTO 633 spectrum.

Figure 4.7 shows the experimental STED fluorescence quenching with and without SPR enhancement. Spontaneous fluorescence emissions under increasing STED beam power from 0 mw to 50 mw were measured and presented in figure 4.7 (a). Quenching of spontaneous fluorescence emission at the peak of the STED beam with and without SPR enhancement were compared and shown in Figure 4.4 (b). STED quenching is much stronger on the SPR substrate than on the plain glass coverslip.

The field enhancement factor varies little when the SiO₂ layer thickness is between 0~30 nm, according to the field calculation. However, the SiO₂ layer thickness is a critical factor for metal quenching effect on fluorescence emission. An optimal SiO₂ layer thickness needs to balance between the decay of STED evanescence field and the decrease of metal quenching as discussed before. The half quenching distance between a fluorophore and an ideal metal surface is estimated to be 10~15 nm, depended on the properties of the metal and the fluorophore. Thus we compared SPR enhanced STED on 40-nm silver layer and 10, 15 and 20-nm SiO₂ layer

respectively. Spontaneous fluorescence emission intensity at the center of the STED beam was fitted with a quenching curve of $(1 + P_{STED}/P_{SAT})^{-1}$. P_{SAT} represents the STED beam power that caused 50% quenching at the beam center. Table 4.1 lists fitted P_{SAT} on glass and SPR structures with four different SiO₂ thicknesses. Estimated I_{SAT} values are also listed. The strongest STED effect was observed on 40-nm silver and 15-nm SiO₂. A STED enhancement factor of 8 was observed in the SPR substrate compared with glass substrate, which is slightly lower than the field calculation result due to the neglect of the metal quenching effect. With a 50-mW STED beam, 10 I_{SAT} over a $17 \times 10 \mu m^2$ area or 14 I_{SAT} over an $11 \times 6.5 \mu m^2$ area were achieved on an optimal SPR structure of 40-nm silver and 15-nm SiO₂. With this SPR enhancement, further resolution improvement of STED-SIM is possible.

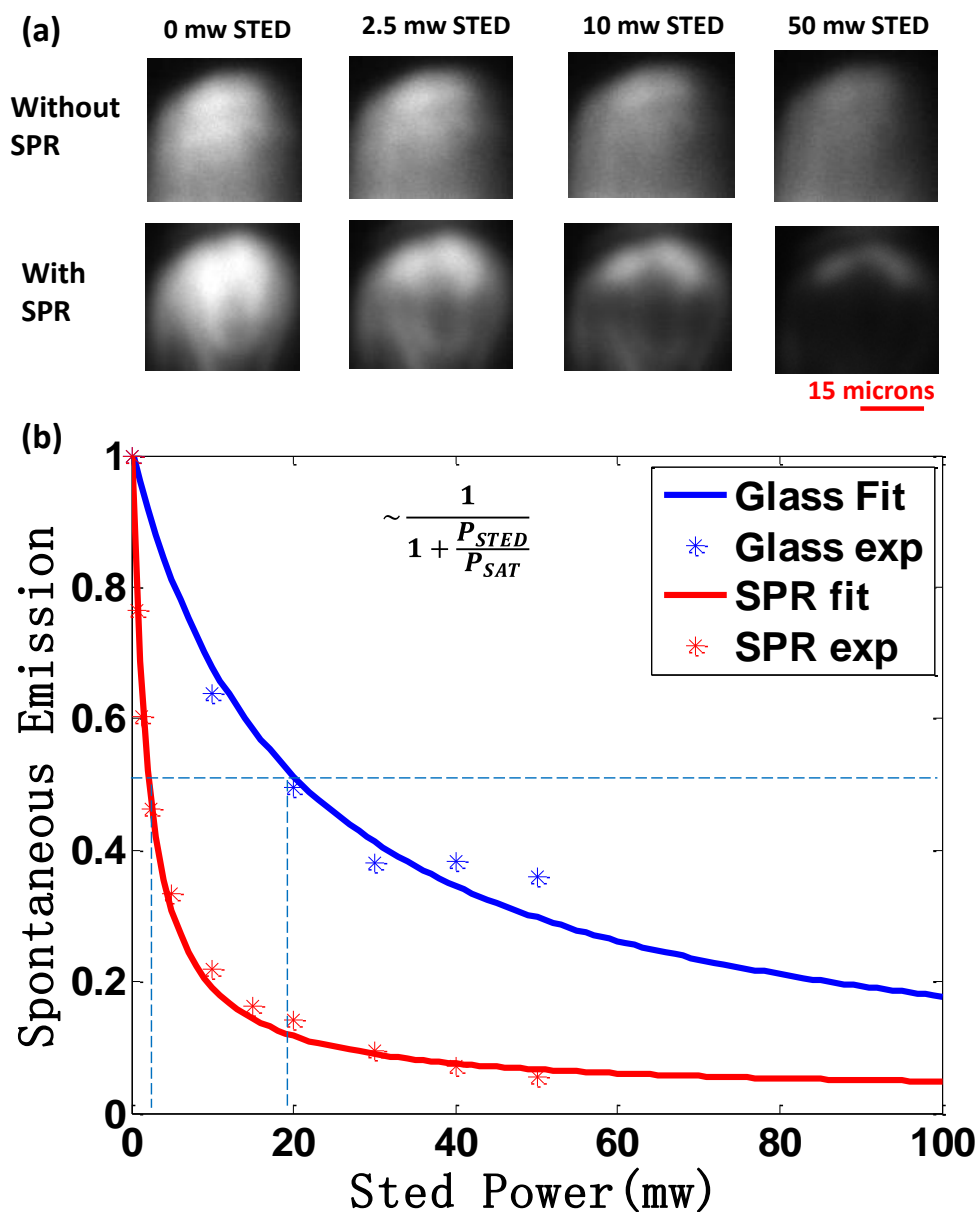


Figure 4.7 STED effect with and without SPR enhancement. Top: spontaneous emission patterns from Atto 633 water solution on a glass and a glass-silver-SiO₂ substrate. The pattern frame size is 30×30 μm². The STED power was increased from 0 to 2.5, 10, and 50 mW respectively. The STED beam had an FWHM size of 18×11 μm². Considering the objective lens caused a 40% transmission loss, the estimated instantaneous STED intensities on the sample were approximately 0, 3, 13, and 65 MW/cm² at the beam center. Bottom: Quenching of spontaneous emission at the center of the STED beam on SPR substrate and glass. The SPR substrate was a glass coverslip

coated with 40 nm silver followed by 15 nm SiO₂. Quenching fitting curves follow $(1 + P_{STED}/P_{SAT})^{-1}$. P_{SAT} values are listed in Table 4.1 [51].

Table 4.1 Full-field STED on different substrates

50% quenching point	Glass	40 nm Silver + 10 nm SiO ₂	40 nm Silver + 15 nm SiO ₂	40 nm Silver + 20 nm SiO ₂	40 nm Silver + 30 nm SiO ₂
P_{SAT} (mW)	14	2.5	1.7	2.0	3.5
I_{SAT} (MW/cm ²) ^a	18	3.3	2.2	2.6	4.6

^a I_{SAT} values were estimated based on the 18×11 μm² FWHM STED beam size, 1MHz repetition rate, ~350 ps pulse duration, and 60% transmission rate of the TIRF objective lens. The transmission rate of TIRF objective lens is estimated by the reflection beam from TIRF. The power of reflection beam is 40 % of the incident beam. Considering the fact that the reflection beam passes objective lens twice, the estimated transmission rate of the objective lens is 60%. [51]

4.3 1D SPR enhanced STED-SIM

4.3.1 Optical setup of 1D STED-SIM with SPR enhancement and the sample preparation

Figure 4.8 illustrates the optical setup of one dimensional SPR enhanced STED-SIM imaging system. Similar to the previous TIRF-STED setup, two beams with different wavelengths were generated by the same supercontinuum laser source (Fianium SC-450-PP-HE) and bandpass filters (Semrock FF01-630/20-25 and Semrock FF01-716/40-25, both tilted). The excitation power and the STED power are 1 mw and 50 mw, respectively. The arrival time difference between pulses from two paths was optimized by the delay stage in excitation path. A customized binary phase grating was placed in the STED path to split the beam. The grating was placed on a piezo stage to perform phase shifting during the experiments. All the orders except ± 1 orders were blocked (around 50% of the energy were distributed in ± 1 orders). The remaining two beams then passed through an oil immersion objective (NA=1.49) to interference on the object plane. The automatic control of the STED beam on/off status was performed by an automatic shutter mounted in the STED path. The fluorescence emission from the sample was

detected by a sCMOS camera after collected by another oil immersion objective (NA=1.49) and filtered by a bandpass filter (Semrock FF01-661/20-25). The inset structure in figure 4.8 illustrates the multi-layer film and the SPR interference generated by laser beam and thin films. The optical system was completed with the data acquisition card, piezo stage and electrical shutter to perform automatic 1D superresolution imaging.

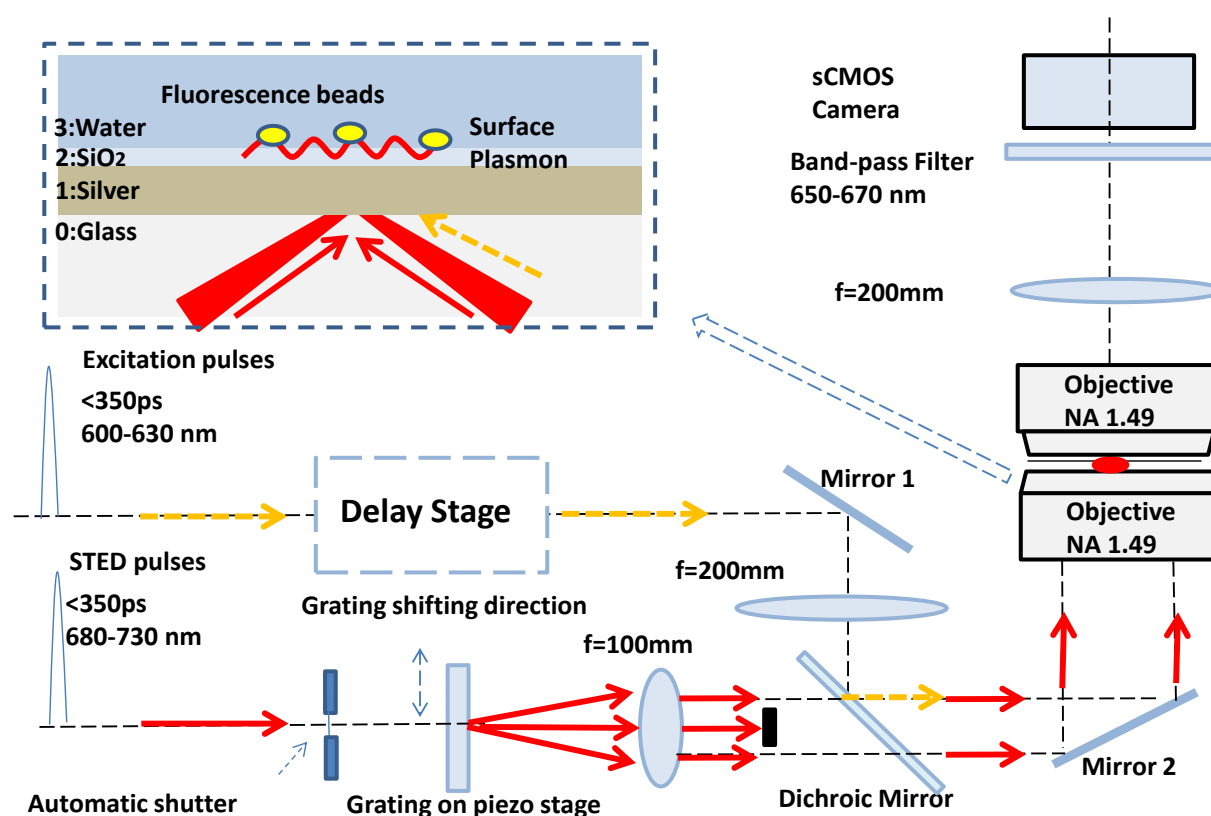


Figure 4.8 1D SPR-enhanced STED-SIM setup. The inset shows the SPR interference generated by laser beam and thin films.

The sample imaged by our 1D STED-SIM setup are 20 nm fluorescent beads (Invitrogen, crimson fluorescent (625/645)). The fluorescent beads are chemical bonded to the coverslip through following process (Figure 4.9): 1. Perform piranha wash on pre-cleaned coverslip to

hydroxylate the glass surface. Mixed 20 ml H_2O_2 (30%) and 60 ml H_2SO_4 (98%) (Pour H_2SO_4 into H_2O_2 in the beaker with coverslip) for 25 minutes. Rinse the coverslip with Milli-Q water and dry it with nitrogen gas; 2. Salinize the surface with APTES ethanol solution. Immerse the coverslip into the mixed solution of 75 ml ethanol, 3 ml water, 2 ml APTES and heat to 50 centigrade for 20 minutes. Rinse the coverslip with Milli-Q water and dry it with nitrogen gas; Heat to 100 centigrade in the air for 20 minutes for curing. 3. Chemical bond the fluorescent beads with surface-aminated coverslip. Dilute the fluorescent beads water solution into the concentration of 0.00007% solid and sonicate it for 10 minutes. Immerse the coverslip with aminated surface into the fluorescent beads solution for 10 minutes at room temperature. Rinse the coverslip and dry it by nitrogen gas. The mounting medium for fluorescent beads sample is anti-fading solution prepared through following process: 1. Add 2.4 g Mowiol into 6 g glycerol. Stir to mix; 2. Add 6 ml Milli-Q water and stir overnight; 3. Add 12ml 0.2 M Tris (PH 8.5) and heat to 50 C° for 30 minutes; 4. Centrifuge at 3000 rad/s for 10 minutes; 5. Add 2.5% dabco for anti-fading. The sample was mounted in a customized sample chamber. The sample chamber is prepared by seal two coverslips with a Press-to-Seal silicone isolator placed and tightly sealed in the middle of them.

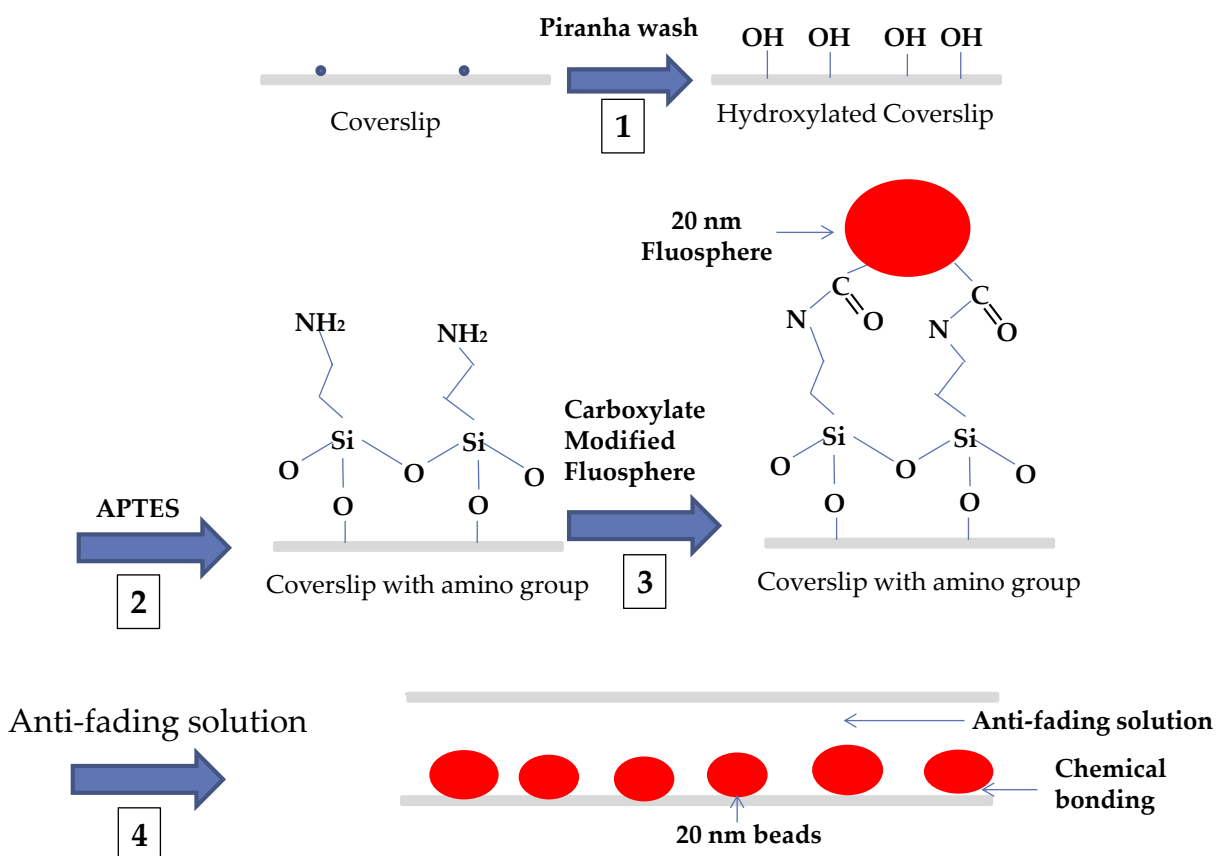


Figure 4.9 Fluosphere sample preparation process.

During the image acquisition process, a set of images with varied phases were taken under following steps: 1. Turn on the uniform excitation beam. 2. Open the automatic shutter to turn on the 1D STED interference on top of the sample. 3. One frame is acquired by sCMOS camera with 30 ms exposure time. 4. The grating is shifted by a fixed phase by driving the piezo stage. 5. Another frame is acquired by sCMOS camera with 30 ms exposure time. 6. Repeat until the phase of the grating was shifted by 2π totally.

4.3.2 5-fold improved resolution beyond diffraction limit on fluorescent beads with 1D superresolution reconstruction

After acquiring the complete set of the images, the superresolution reconstruction was performed following the algorithm described in the previous chapter. As shown in figure 4.10, the shifting phase of each step was set to be $\frac{2}{5}\pi$ and 5 original frames were acquired to produce one 1D superresolution image. The diffraction limit image of three fluorescent beads with uniform excitation is presented in figure 10 (a). After turning on the STED interference field, 5 frames with varied interference phases were taken and shown in figure 4.10 (b). At different phases, difference fluorescent beads were turned off from camera by stimulated emission depletion. The data analyze was performed in frequency domain. Figure 4.10 (c) presents the Fourier transform of five original images with different phases. Figure 4.10 (d) shows the reconstructed image in frequency domain following the algorithm developed in the previous chapter. The final superresolution image in spatial domain is illustrated in figure 4.10 (e) after inverse Fourier transform.

With sufficient STED power and acceptable interference contrast, the resolution of STED-SIM system is determined by the order of harmonics solved in frequency domain. Figure 4.11 (a) and (d) present the diffraction limit beads image in spatial and frequency domain, respectively. When perform the reconstruction up to the linear term in frequency domain, the resolution of the beads image in spatial domain would be improved by 2 times (figure 4.11 (b) and (e)). Figure 4.11 (c) illustrates the same beads image with 4-fold improved resolution, which is the inverse Fourier

transform of the frequency domain image reconstructed by up to 2nd harmonics order terms. Three and seven original frames are required to reconstruct figure 4.11 (b) and (c), respectively.

With 50 mW STED power from our laser source and 8-fold field enhancement with SPR, the highest harmonics order which can be obtained is 3rd harmonics order, which gives our SPR STED-SIM system resolution a 5-fold improvement. Figure 4.12 (a-b) shows the resolution comparison between diffraction limit image and SPR enhanced STED-SIM image with maximum STED power. The bead cross section comparison between figure 4.12 (a-b) is plotted in figure 4.12 (c) with FWHM of 270 nm and 50 nm for diffraction limit image and SPR enhanced STED-SIM image, respectively. Compared with conventional imaging technique, our SPR enhanced STED-SIM system acquired around 5-fold improvement resolution beyond diffraction limit in one dimension.

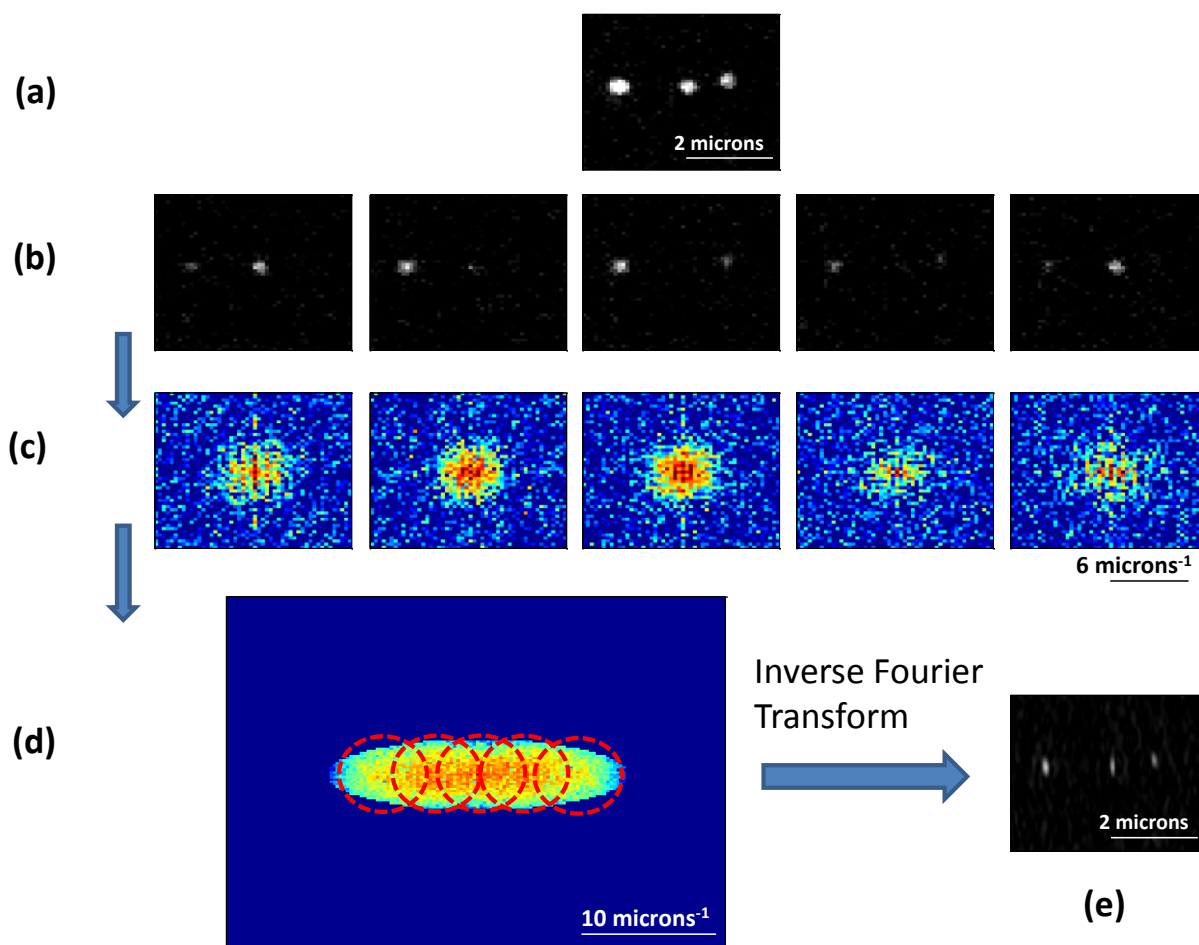


Figure 4.10 1D SPR-enhanced STED-SIM image processing. (a) Diffraction-limit image with a uniform excitation. (b) Fluorescence beads images under a uniform excitation and a patterned STED field with varied phases. (c) Fourier domain information transferred from corresponding spatial domain images in (b). (d) Reconstructed Fourier domain information after image processing. (e) Final reconstructed super-resolution image. Inverse Fourier transform image from (d).

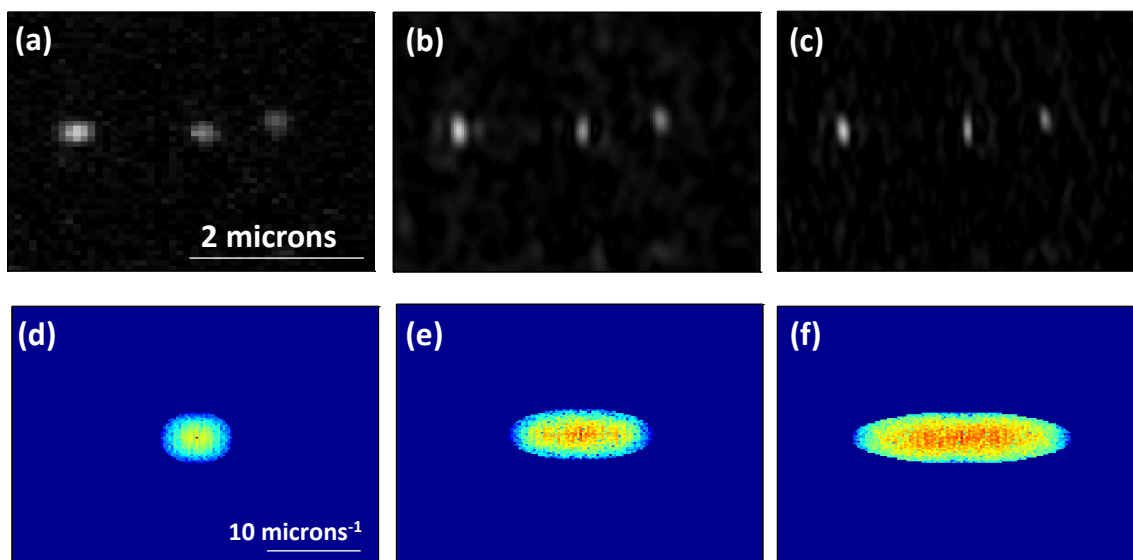


Figure 4.11 (a) Diffraction limit image. (b) Superresolution reconstruction with linear term only. (c) Superresolution reconstruction with up to second harmonics nonlinear term. (d) Fourier domain image of (a). (e) Fourier domain image of (b). (f) Fourier domain image of (c).

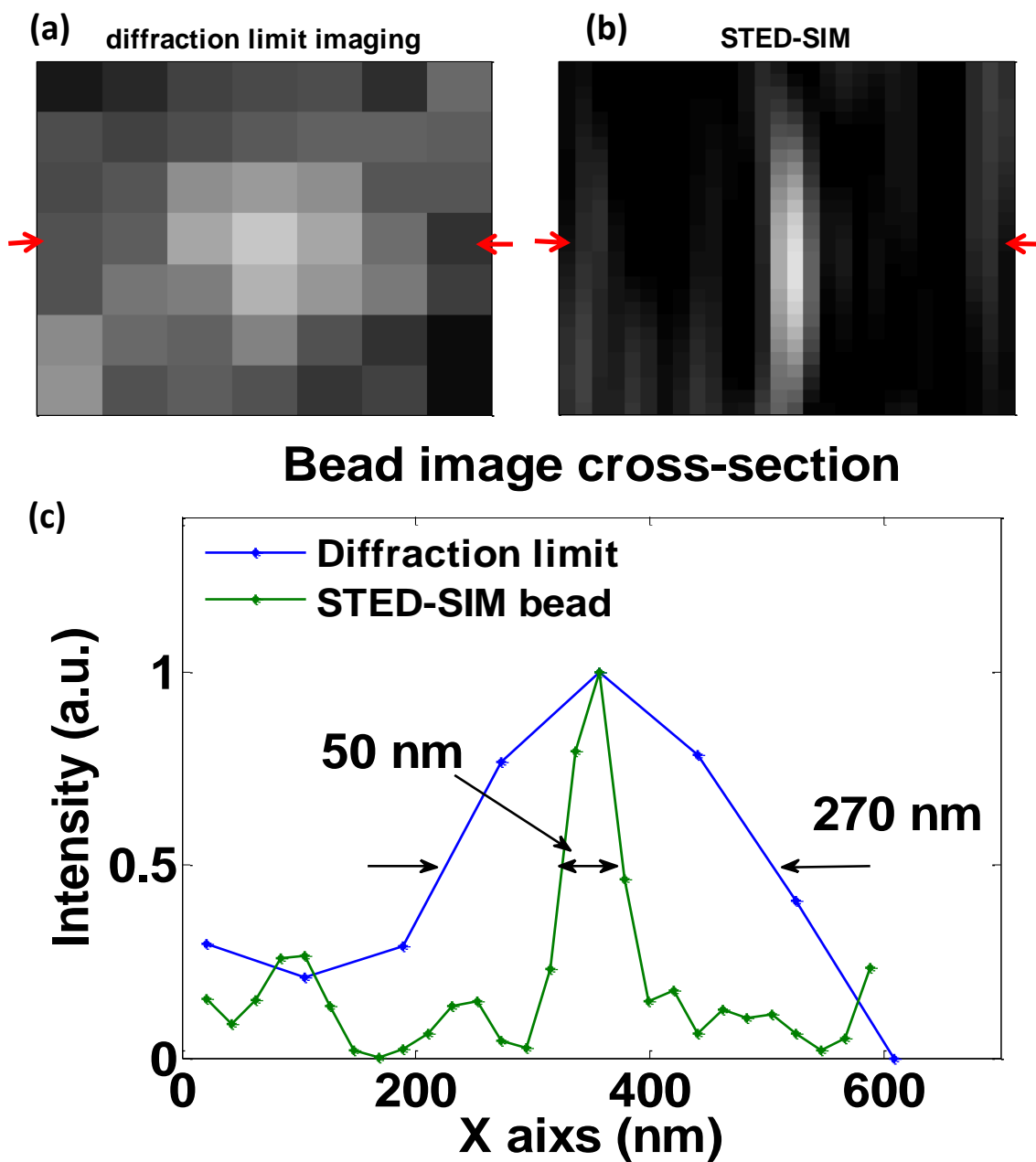


Figure 4.12 (a) Diffraction limit image of one fluorescent bead. (b) Superresolution image of the same beads with reconstruction up to 3rd nonlinear harmonic terms in Fourier domain. (c) The cross section of bead image between the arrows in (a) and (b). The blue and green plots are for diffraction limit and STED-SIM images respectively.

4.4 Challenge and prospect on SPR enhanced STED-SIM

As shown in figure 4.10, the image with only several beads can be reconstructed. Full field superresolution imaging has not been achieved with SPR enhanced STED-SIM. There are two major reasons for this:

1. SPR is the collective oscillation of free electrons in a solid (as presented in figure 4.13 (a)) or liquid stimulated by incident light. It decays over the direction perpendicular to the interface and propagate along the interface at the same time, as can be seen in figure 4.13 (a). The SPR generated by a Gaussian beam will have a long ‘tail’ along the incident direction which make the field intensity distribution uniform. The contrast of two beam interference is highly depending on the intensity of both the two beams, which should be identical over the full field to achieve best contrast. Due to the unbalanced fields from propagation of SPR, high contrast interference is highly difficult to obtain. Figure 4.13 (b) shows the overlap of two propagation SPR waves. Two fields with the same intensity over the entire overlap region cannot be achieved, which means the SPR interference in our experiments has inhomogeneous contrast at different location.

2. Although fabrication techniques can decrease the surface roughness of multi-layer film, it cannot create an absolutely flat surface. A rough surface can cause different phase of the SPR field at same location, which would lead to locally distorted interference fringe as simulated in figure 4.13 (c). The locally fringe distortion cause failures in superresolution image reconstruction.

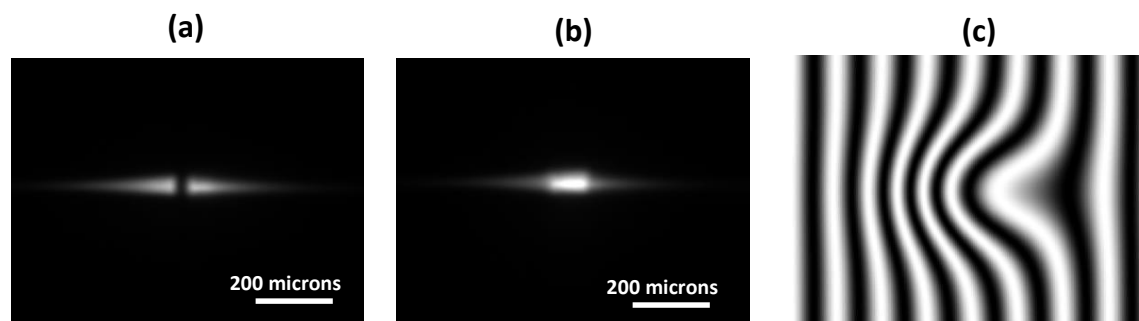


Figure 4.13 (a) Two SPR fields on the surface of multi-layer film. (b) The overlap of two SPR fields. (c) Interference field distortion on rough multi-layer films simulation.

There are many potential approaches to overcome the aforementioned challenges in SPR enhanced STED-SIM. Image reconstruction with random patterns may be the best technique to solve our current problems [67]. Bayesian algorithm has been previously developed [68, 69]. Hundreds of original images would be required to reconstruct one superresolution image.

Chapter 5 Two dimensional superresolution imaging with STED-SIM

This chapter presents a STED-SIM microscope that was built with a commercially available laser source. The system achieves 4-times resolution improvement over the diffraction limit on fluorescent beads. The system was then applied to biological samples. Two dimensional superresolution images of fixed U2OS cell's tubulins and neuron cell's granules were acquired.

5.1 2D STED-SIM experimentally demonstrated by fluorescence beads sample

5.1.1 Two types of optical setups for 2D STED-SIM: transmitted fluorescence STED-SIM and epi-fluorescence STED-SIM

The STED-SIM microscope was implemented in two versions: transmitted fluorescence microscope and epi-fluorescence microscope. In transmitted fluorescence microscope, two high NA objectives were employed for the illumination and detection, the sample between the objectives has a thickness of 200 μm , which leaves little space for large size samples. So though both types of microscope functions well in the fluorescence beads imaging, it is not suitable for imaging biological sample. The epi-fluorescence microscope would be more suitable considering the size of the sample and extra space required to store mounting medium. The setups for both types of STED-SIM microscopes will be introduced.

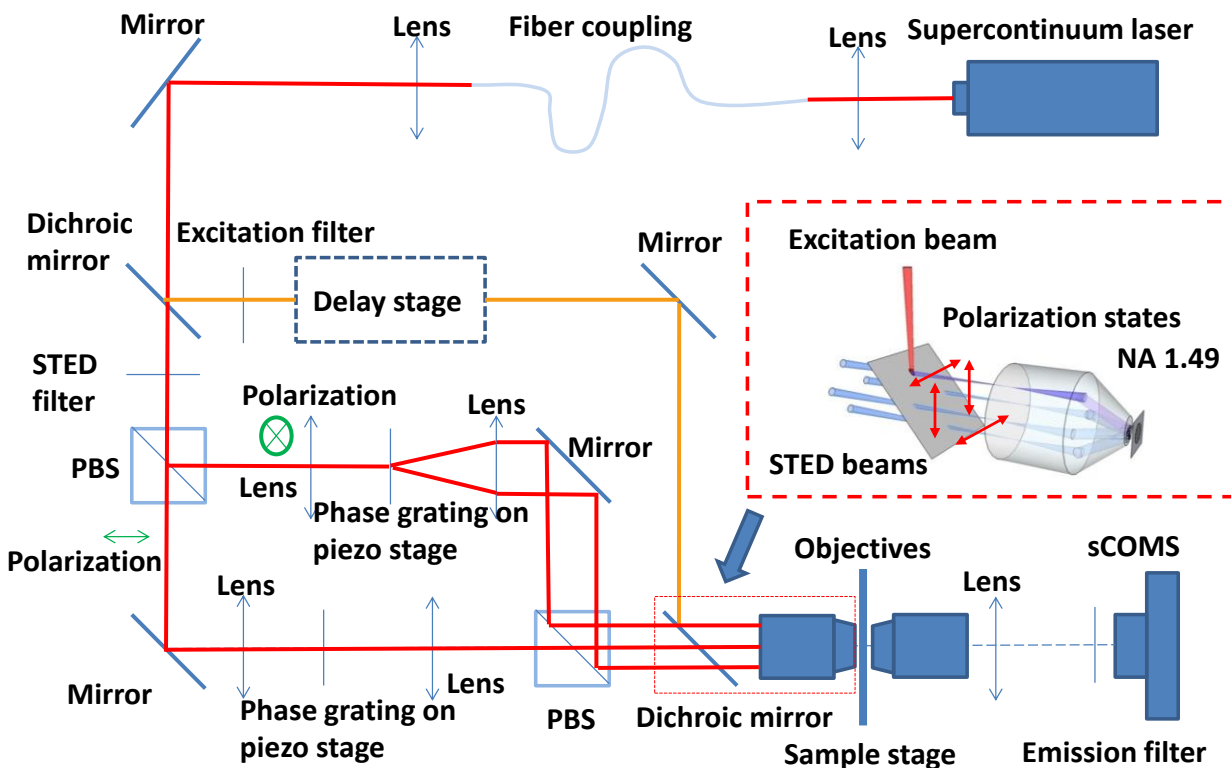


Figure 5.1 Optical setup for 2D STED-SIM transmitted fluorescence microscope. PBS: Polarized Beam Splitter. All lens utilized in this experiment are positive doublets. The inset figure describes the details of the excitation objectives. Both the excitation and detection objectives have the NA of 1.49. The detector is a sCOMS camera.

Figure 5.1 illustrates the optical setup for transmitted STED-SIM. A supercontinuum laser source (Fianium SC-450-PP-HE) was employed to provide both the excitation and STED beams. After coupling through a multimode fiber, the output laser beam was divided into two beams by a dichroic mirror and then passed through excitation and STED filter separately. A delay stage was placed in the excitation path to control the delay of the excitation beam, so that the excitation pulse and STED pulse could reach the sample simultaneously and achieve maximum STED effect.

The STED beam was then separated by a polarized beam splitter (PBS) to provide polarized STED beams in horizontal and vertical path, respectively. In each path, the STED beam was diffracted into two beams by grating and then became parallel after a positive lens. In those two paths, the gratings have different orientations for the beams to be diffracted in orthogonal planes. After recombined by another PBS, four parallel STED beams then propagated into the illumination objectives as shown in the inset of figure 5.1.

Differing from the SPR-enhanced STED-SIM experiments described in the Chapter 4, standard coverslips were used as the sample substrate. The sample was mounted between the illumination and detection objectives. A sCMOS camera placed after the emission filter was utilized to capture fluorescence image.

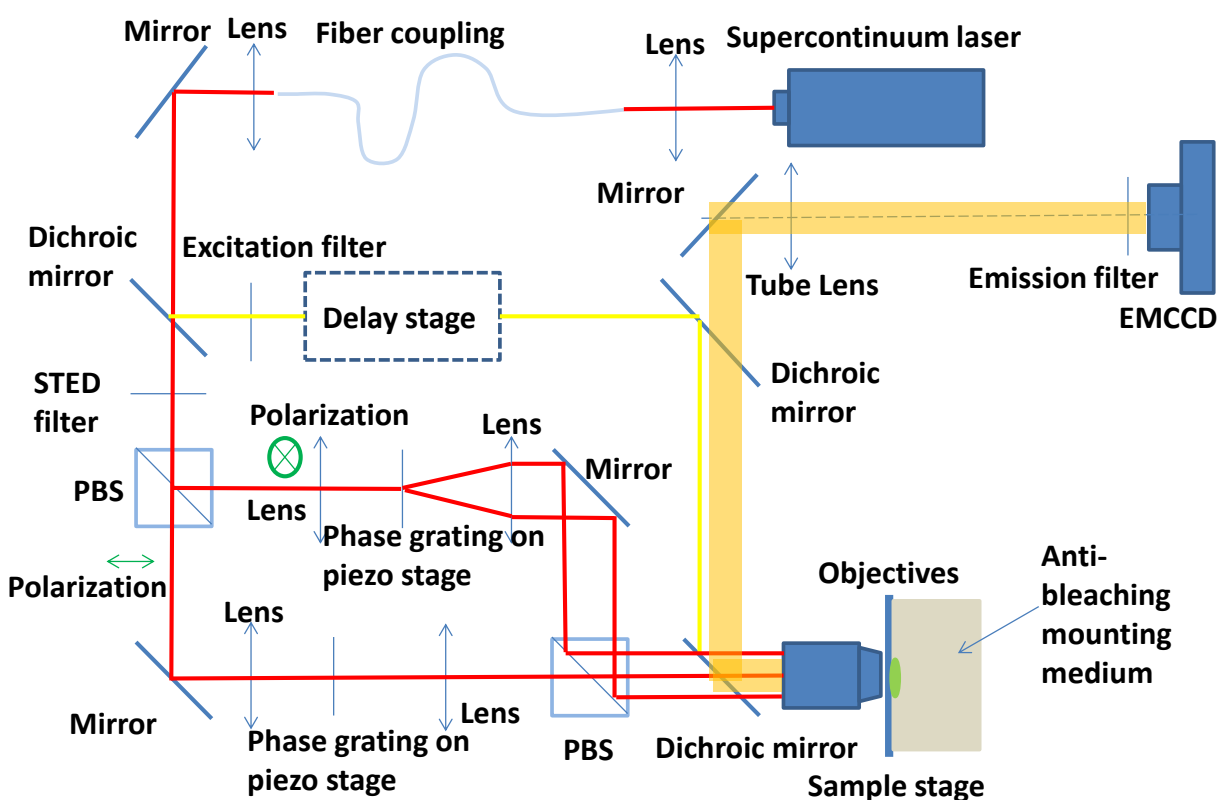


Figure 5.2 Optical setup for 2D epi-fluorescence type STED-SIM. PBS: Polarized Beam Splitter. All lens utilized in this experiment are positive doublets. The inset figure describes the details of the excitation objectives. Both the excitation and detection use the same NA 1.49 objective. The detector is an EMCCD camera.

Figure 5.2 illustrates the epi-fluorescence type STED-SIM setup. The excitation and the STED beam paths were the same as the transmitted type. But for the fluorescence detection, the illumination objective was also utilized to collect the emission from the sample. An EMCCD was employed to acquire the images with best quality. The experiments with large-size biological sample mounted in anti-fading medium can be realized with this epi-fluorescence type STED-SIM in the cost of strict requirement on dichroic mirror choice. This type of STED-SIM microscope is also more suitable for live cell imaging since it leaves more space for cell activities.

5.1.2 STED interference contrast calibration

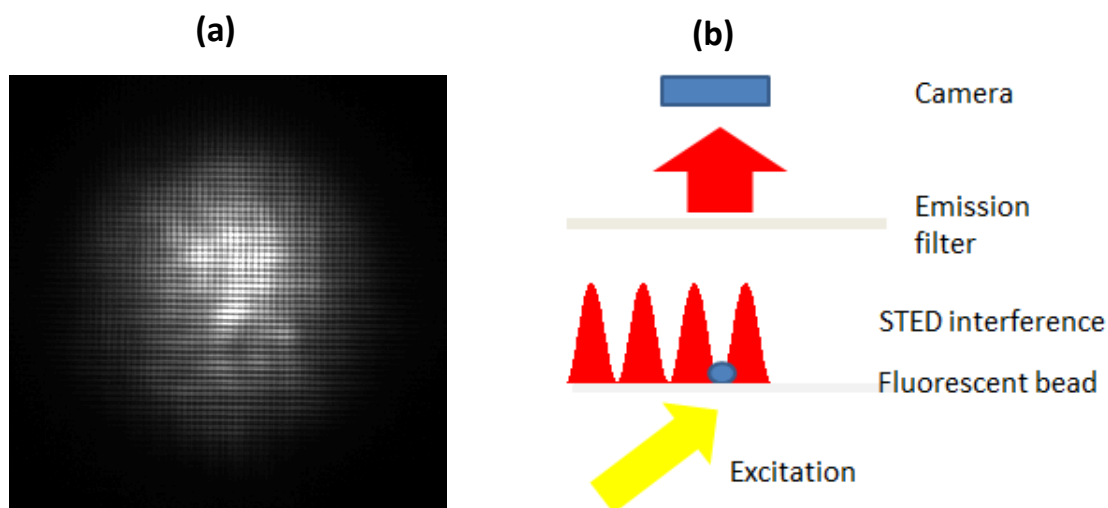


Figure 5.3 (a) 2D STED pattern. The field of view is $25 \times 25 \mu\text{m}^2$. (b) STED interference contrast calibration experiment. One dimensional STED interference is scanned across a single bead while illuminated by a uniform excitation. A camera is placed after emission filter to detect fluorescence signal emitted from this single bead.

The 2D STED pattern performed in the experiment is shown in figure 5.3 (a). The non-uniform field is resulted from the low beam quality of the laser source. The low contrast interference owes to the low sampling rate in this image. An interference contrast calibration test is performed with the schematic shown in figure 5.3 (b). One single fluorescence bead was placed on sample stage with uniform excitation. A camera was placed after emission filter to detect the fluorescent signal from this bead. The full emission without STED quenching was detected before turning on STED interference. After a STED interference pattern was placed on this bead, a piezo stage was driven to shift the interference step by step. At each step, a fluorescent signal from this bead was read by camera and then lead to the plot as shown in figure 5.4. The x axis in the plot is the position of the STED interference pattern (or the phase of interference pattern) and y axis represents the relative fluorescence signal detected by camera. With 360 nm STED pattern period, the peak of the fluorescence has the width of 90 nm, indicates a resolution better than 90 nm in our STED-SIM system.

STED interference contrast test

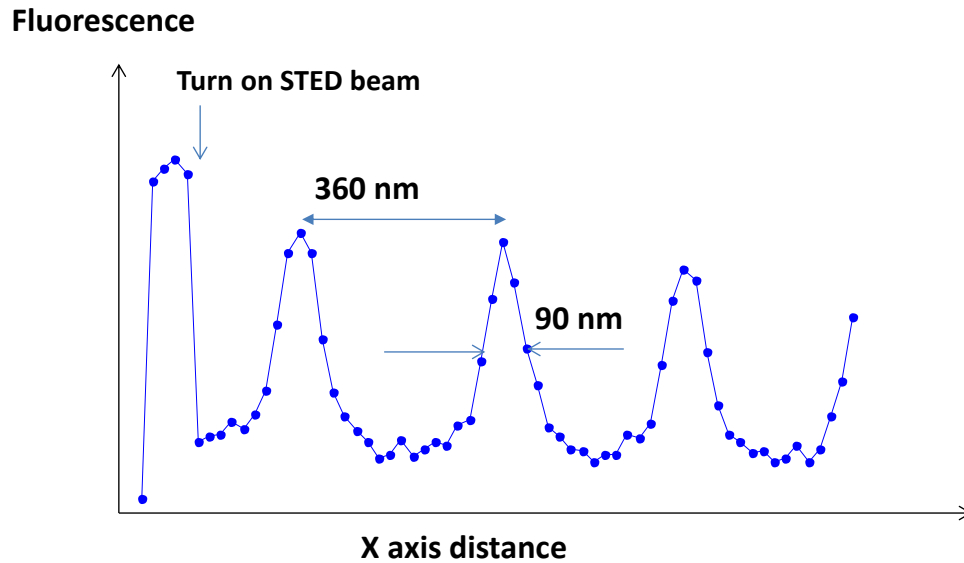


Figure 5.4 The STED interference contrast test. X axis is the x position of the interference and Y axis is the relative fluorescence signal from one single bead.

The contrast of the STED pattern is calculated following Eq. 2.2:

At the peak of the fluorescent signal, STED pattern is at its minimum: $I_{min} = 0.25I_{sat}$.

At the valley of the fluorescent signal, STED pattern is at its maximum: $I_{max} = 7I_{sat}$.

The contrast of the STED pattern is then equal to: $\frac{I_{max}-I_{min}}{I_{max}+I_{min}} = 93\%$.

The limitation to the further improvement of the STED interference pattern can be attributed to two main reasons: first, the STED beam interference is chosen to be converging beam interference in order to increase the STED power density, which prevent the perfect interference contrast naturally. The best interference contrast is typically acquired from the interference of

two collimated beam; second, the interference contrast is also limited by the beam quality of the laser source.

5.1.3 2D Superresolution imaging on fluorescent beads

The performance of the STED-SIM microscope was first tested with 20-nm diameter fluorescence beads. The 20 nm beads sample preparation is the same as what was described in chapter 4. With chemical bonding, the beads can stay permanently on the coverslip. For imaging these beads in superresolution, the 2D STED pattern is shifted in 9 phases in each dimension. A total of 81 raw frames are required. For each frame, the exposure time is 30 ms and moving time of piezo stage is around 5 ms. The excitation power is 1 mw and the STED power is 50 mw for each direction. On the sample stage, the size of the excitation beam and the STED beam are $40 \times 40 \mu\text{m}^2$ and $12 \times 12 \mu\text{m}^2$ respectively. The diffraction limit image and the reconstructed image are processed from the raw frames with the algorithm developed in chapter 3 (figure 5.5). The diffraction limit image and STED-SIM superresolution image of an identical object in full field are shown in figure 5.5 (a) and (b), respectively. By comparing these two figures, it can clearly be seen that the STED-SIM system is able to resolve beads separated by a distance below the diffraction limit. A magnified portion of STED-SIM image is shown in figure 5.5 (d), which clearly demonstrates a significantly enhanced resolution by STED-SIM.

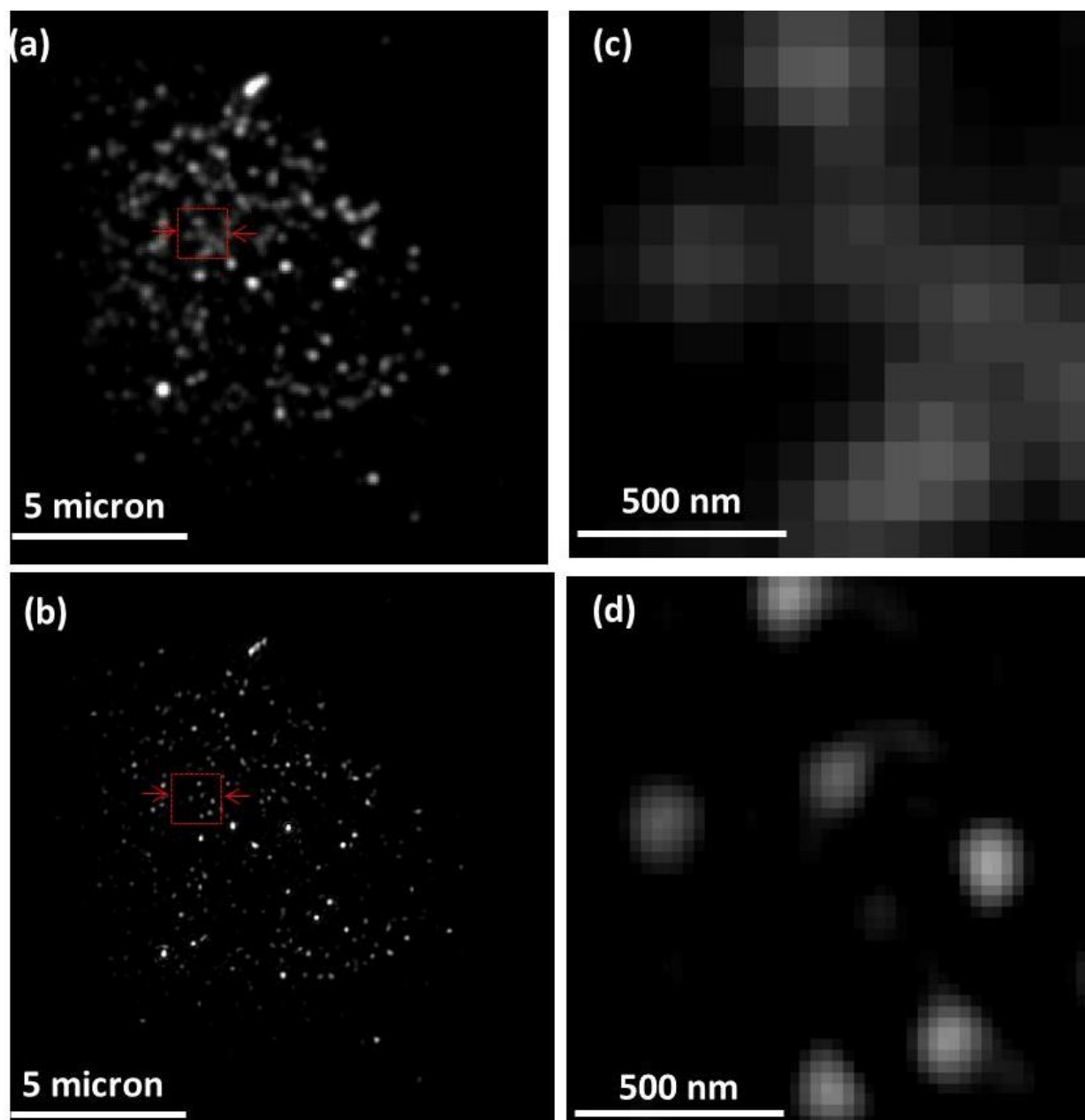


Figure 5.5 (a) Full field diffraction limit image. (b) Full field STED-SIM superresolution image. (c) Magnified image of the red square region in (a). (d) Magnified image of the red square region in (b).

To quantize the resolution of STED-SIM system, the FWHM of single bead is plotted in figure 5.6. Those beads profile are obtained from the region between the arrows in figure 5.5 (a) and (b). The green plot and blue plot are from diffraction limit image and STED-SIM image, respectively.

The FWHM of the bead profile in STED-SIM image is around 80 nm. Considering the bead has a diameter of 20 nm, the resolution of our STED-SIM microscope is better than 80 nm. In our experiment, the emission wavelength is 660 nm and working NA is 1.33 (the beads are mounted in water-based solution), which provides a 300 nm diffraction limit resolution. Four-fold resolution improvement has been achieved with our STED-SIM system.

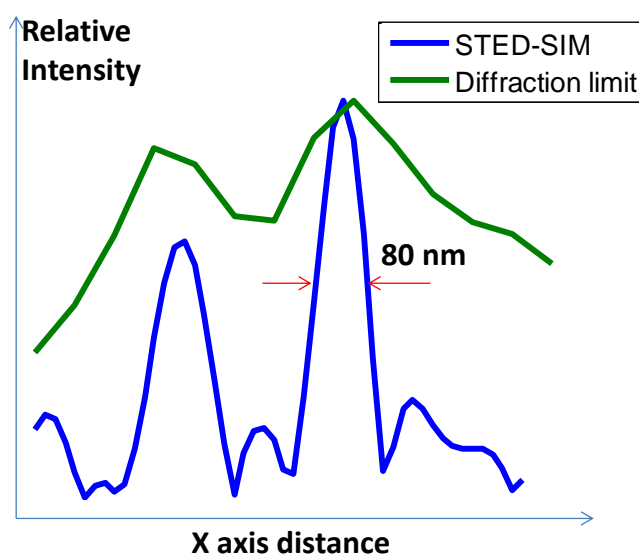


Figure 5.6 Beads profile between arrows in figure 5.5 (a) and (b). The green plot is the profile for diffraction limit image and blue plot is the profile for STED-SIM image. The FWHM of the bead profile in STED-SIM image is 80 nm.

5.1.4 Superresolution imaging stability test

In superresolution imaging, slight vibrations of the interference pattern or object stage will lead to significant reduction on the quality of the reconstructed image, and it's crucial to maintain the stability of the system. Several methods were used to limit vibrations in the system. In the sample side, a customized 3D stage, which can stay stable during the imaging process, was used to mount the sample. However, vibrations in interference pattern may not be avoidable because

that the grating stages are shifted step by step during the image acquiring. A set of tests were performed to measure the stability of grating stages. After taking an image of interference pattern and performing Fourier transform on this image, the phase of the pattern can be calculated from the phase of the first order peak in the Fourier image. When the piezo stage was shifting along the horizontal axis, the grating phase switched steadily as shown in figure 5.7 (a). However, due to the weight of the stages, fast stage shifting resulted in vibration along vertical axis, as shown in figure 5.7 (b). Figure 5.7 (c) illustrates the stability test results with inverted grating mounting when shifting the stage along vertical axis. In this case, a more steady shifting process was observed because the gravity force presses the mechanical spring of stage to keep it in tension.

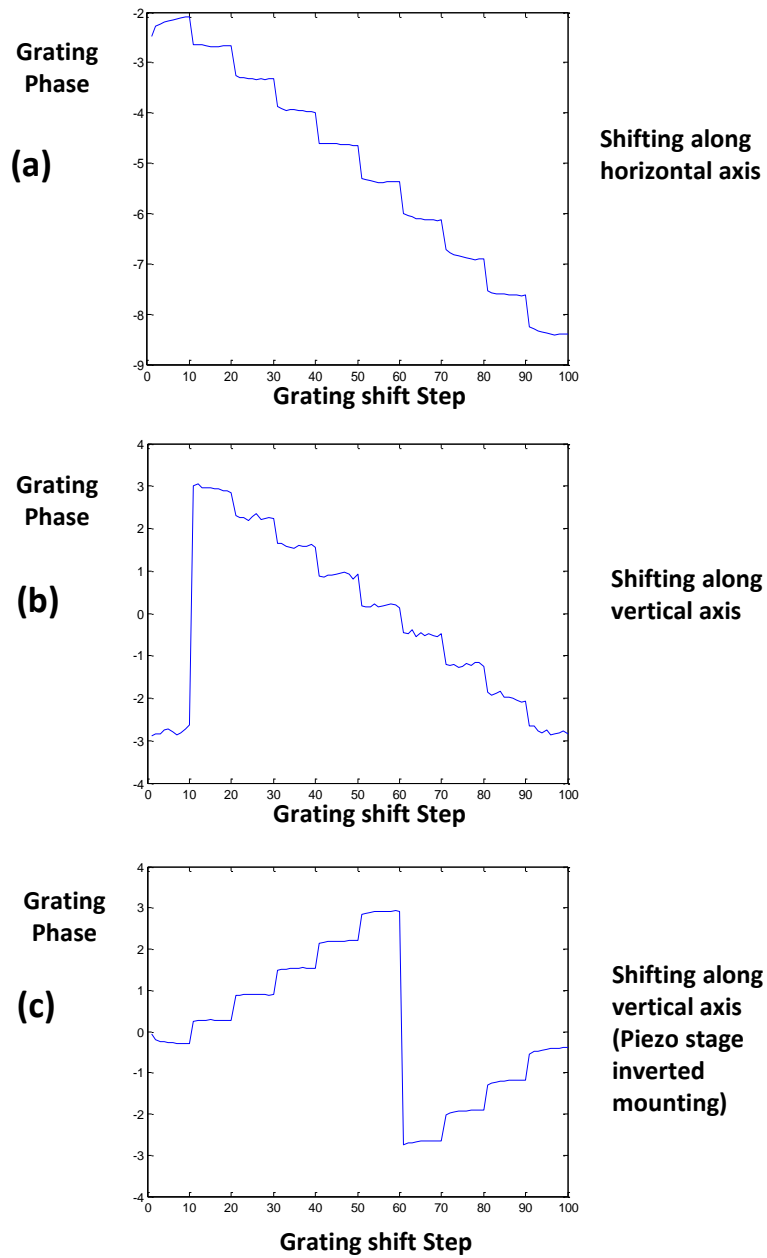


Figure 5.7 Grating stability test. (a) Grating phases with piezo stage shifts along horizontal axis. (b) Grating phases with piezo stage shifts along vertical axis. (c) Grating phases with piezo stage (inverted mounting) shifts along vertical axis.

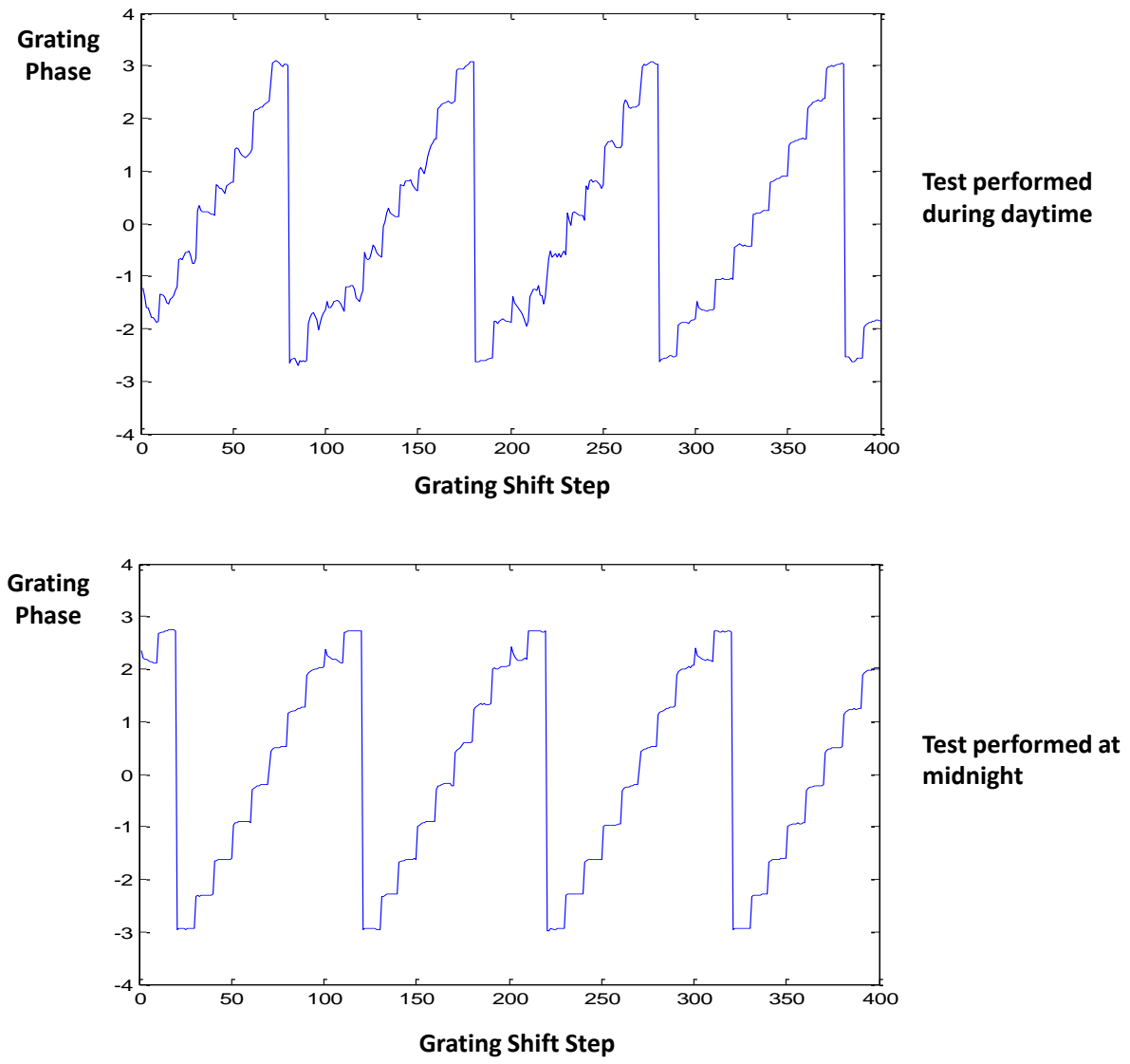


Figure 5.8 Grating stability test at different time. (a) Vertical axis test during day time. (b) Vertical axis test at midnight.

Although the grating vibration can be decreased by inverting the stage mounting along vertical axis, extra effort is still needed to minimize the artifacts caused by the remained vibration. We will discuss this effect in the next section. The stability of piezo stage is not only affected by the gravity but also the experimental environment. Figure 5.8 compares same tests performed during

daytime and midnight. The results clearly show that the stage shifts more stable at midnight due to the quieter experimental environment in midnight. Imaging results of biological samples, which will be presented in the next section, were taken at midnight.

5.2 2D superresolution imaging on fixed biological samples

5.2.1 Sample preparation

In this section, all the fixed biological samples are immunostained following this protocol:

1. Fix the cells with formalin for 10 minutes.
2. Wash the sample in 0.1% sodium borohydride in PBS (phosphate buffered saline) for 7 minutes.
3. Wash the sample in PBS for 3 times (5 minutes per time).
4. Block the sample with blocking buffer for 1 hour.
5. Incubate the sample with 1/200 primary (diluted in blocking buffer) for 30 minutes.
6. Wash the sample with washing buffer for 3 times (10 minutes per time).
7. Incubate the sample with 1/500 secondary (diluted in blocking buffer) for 30 minutes.
8. Wash the sample with washing buffer for 5 times (5 minutes per time).

And the mounting medium is prepared by mixing following chemicals:

1. 1 μ l of 40 mg/ml catalase in TN buffer. Centrifugation is performed on this solution before use.
2. 5 μ l of 100 mg/ml glucose oxidase in TN buffer.
3. 894 μ l of 1mg/ml Trolox in TN buffer. This solution need to be filtered before use.
4. 100 μ l of 100mg/ml glucose in TN buffer.

The anti-bleaching mounting medium should be prepared within one hour before the experiments.

5.2.2 STED-SIM imaging with tubulins of U2OS cell

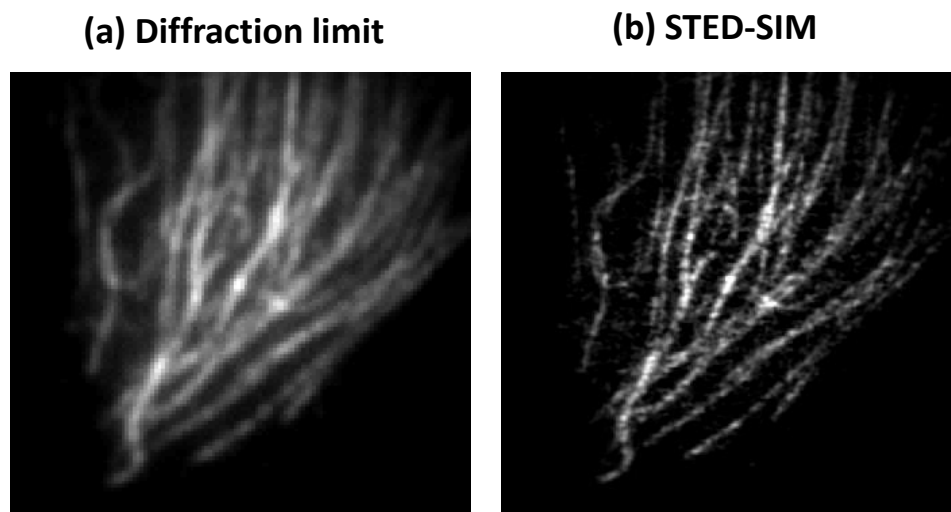


Figure 5.9 (a) Diffraction limit image of tubulins in fixed U2OS cell, labeled with ATTO 633. The field of view is $12 \times 12 \mu\text{m}^2$ (b) STED-SIM superresolution image of the same object in (a).

Figure 5.9 (a) illustrates the diffraction limited images of tubulins in a fixed U2OS cell. Those tubulins typically have a diameter of 10 nm. The adjacent tubulins with a separation less than 300 nm were not resolved in this image. The STED-SIM image of the same object is shown in figure 5.9 (b). Clearly, more details of the adjacent tubulins were revealed from those superresolution images. Proven by those tubulins images, after the image reconstruction, the STED-SIM system is capable of superresolution with biological samples. The imaging speed is 3 seconds per superresolution image. With rising excitation power, the imaging speed can be increased in the cost of sample bleaching.

As is discussed in the previous section, the grating vibration in vertical axis causes artifacts in reconstructed image (figure 5.10 (a)). This periodic artifact presented in the reconstructed image is resulted from the circled region in the Fourier domain image shown in figure 5.10 (c). And

these periodic signals in the circled region in Fourier space can be filtered out and replaced with the average value surrounding the signal as shown in figure 5.10 (d). Figure 5.10 (b) illustrates the final reconstructed image from figure 5.10 (d). The periodic artifacts are significantly removed.

Another phenomenon that prevents further resolution improvement in our system is the two photon excitation due to the strong STED field. It means that the STED beam illuminated on top of the sample not only quenches but also excites our fluorescent dye, which interrupts the image processing with strong background noise. With a better fluorescent dye which will not be excited by STED beam and a more stable motorized stage, the STED-SIM system can be optimized to achieve further improved resolution.

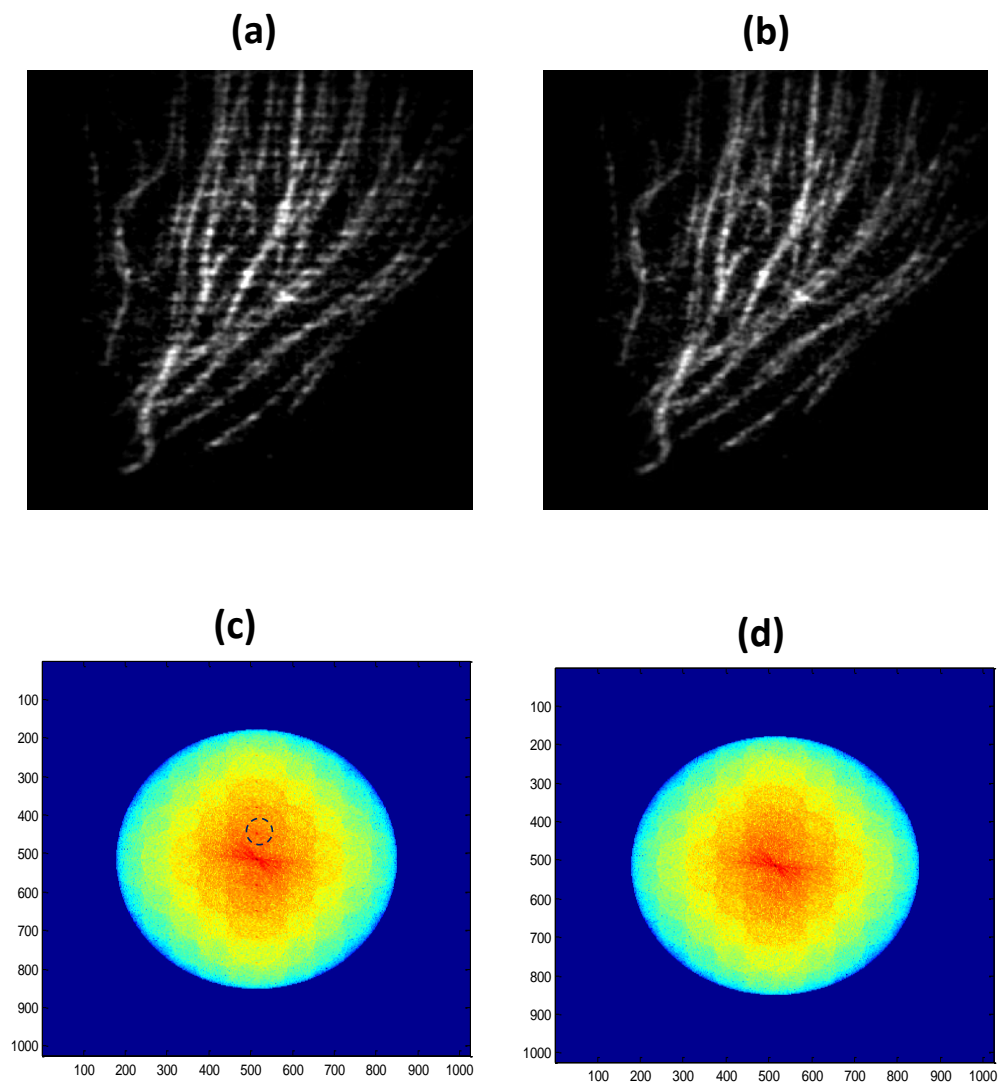


Figure 5.10 (a) Reconstructed image with artifacts. (b) Reconstructed image without artifacts. (c) The Fourier domain image of (a). (d) The Fourier domain image of (b)

5.2.3 STED-SIM imaging with granules of neuron cells

The granules of fixed neuron cells which contained the protein FMRP (Fragile X Mental Retardation Protein) were also imaged by our STED-SIM system. Since this is an RNA binding protein, we most likely were observing RNA and protein containing granules which are actively

transported in the cell on microtubules. Figure 5.11 (a-e) present the diffraction limit images of neuron cells' granules. Figure 5.11 (f-j) shows the superresolution images from our STED-SIM system with identical objects. The results again demonstrate that the STED-SIM system is suitable for superresolution imaging of samples with biological interests.

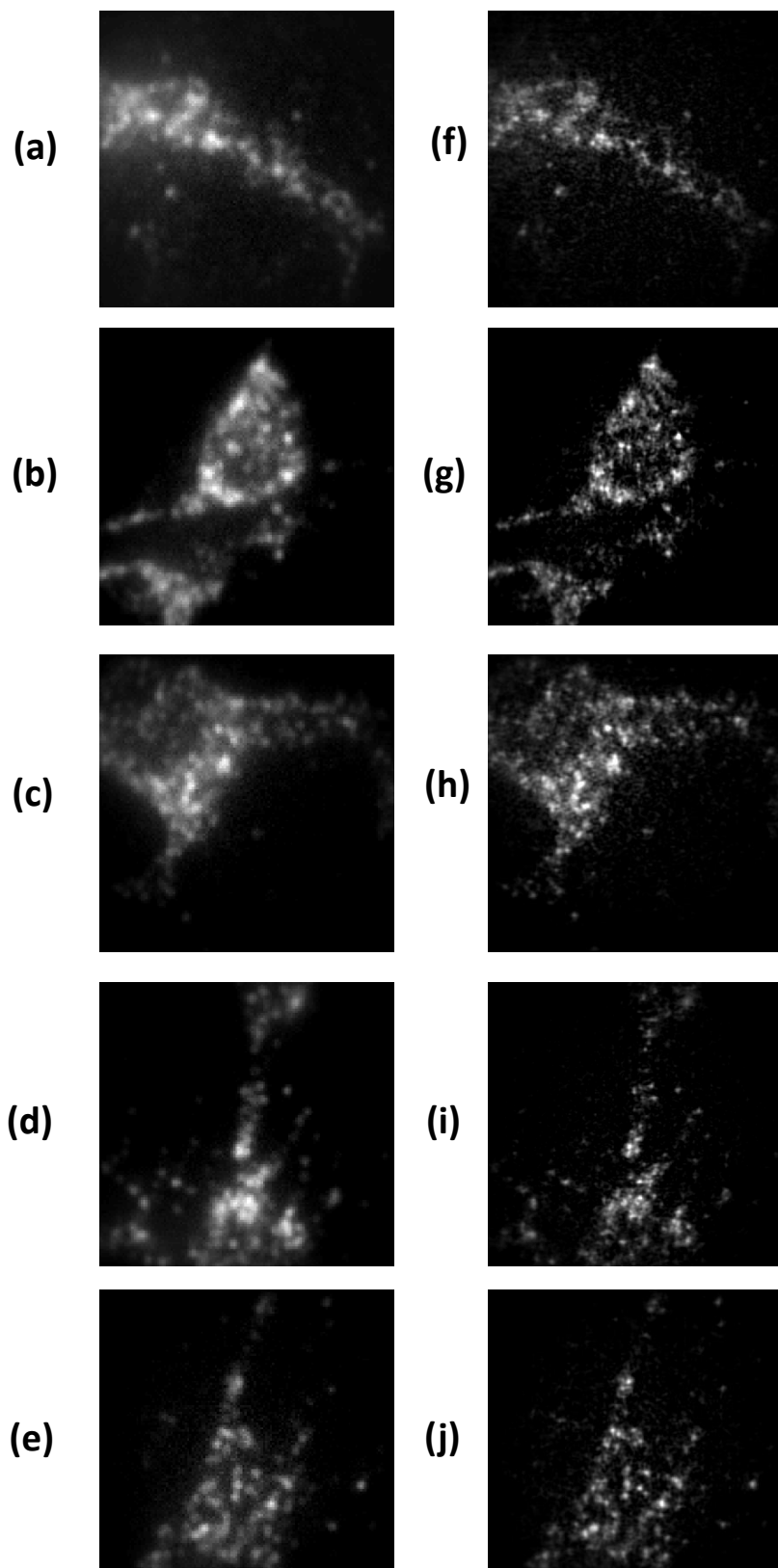


Figure 5.11 (a-e) Diffraction limit images of granules of neuron cells. (f-j) STED-SIM images of the same objects.

5.3 Summary

In this Chapter, experiments of 2D STED-SIM with the capability of superresolution imaging with fluorescent beads sample have been performed. 4-fold improved resolution has been realized. The stability test results indicate that the quality of the reconstructed image can be improved with more stable stages. Furthermore, U2OS cell's tubulins and neuron cell's granules have been successfully imaged with resolution breaking the light diffraction. Those experimental results validated our STED-SIM system as a fast full-field fluorescence imaging technique with superresolution.

Chapter 6 Summary

In the chapter 1 of this dissertation, the diffraction limit in fluorescence microscopy and several types of superresolution imaging techniques are introduced. All these techniques have been demonstrated to be practical in cell imaging with some limitations, which give us motivation to develop a new superresolution imaging technique.

By applying a strong nonlinear effect, STED quenching effect, a novel nonlinear SIM termed as STED-SIM is proposed to perform fast superresolution microscopy in full field. Compared with other nonlinear SIM, STED-SIM has the fundamental advantages of fast imaging speed, negligible switching stochastic noise, low shot noise and theoretically unlimited resolution.

The algorithm for STED-SIM superresolution reconstruction is then developed. Different from previous nonlinear SIM, instead of applying one dimensional interference pattern, 2D grid interference pattern is employed to maximize the imaging speed by removing pattern rotation. By simulating the STED-SIM image acquisition and processing in 1D, the influence of STED power and interference contrast to final reconstructed image quality is studied. The feasibility of STED-SIM with commercial available laser source is validated by 2D STED-SIM simulation.

In the effort of reaching 30 nm imaging resolution with commercial available laser source, a field enhancement mechanism, surface plasmon resonance (SPR), is introduced to our STED-SIM system. The SPR field enhancement effect is firstly predicted by field calculation and simulation. The experimental test shows that the SPR mechanism provides 8 times stronger quenching effect for STED beam to turn off the excited fluorophores. With a 50-mW STED beam, $10 I_{SAT}$ over a $17 \times 10 \mu m^2$ area or $14 I_{SAT}$ over an $11 \times 6.5 \mu m^2$ area were achieved on an optimal SPR structure

of 40-nm silver and 15-nm SiO₂. The introducing of SPR enhancement to STED-SIM system provides better than 50 nm resolution in some region but fails to achieve improved superresolution in full field because of the propagation of the SPR field along the interface and the distortion of interference field.

In chapter 5, a 2D full field STED-SIM microscope that was built with a commercially available laser source is presented. The system achieves 4-times resolution improvement over the diffraction limit on fluorescent beads. The system was then applied to biological samples. Two dimensional superresolution images of fixed U2OS cell's tubulins and neuron cell's granules were acquired.

In the next section, appendix, the application of nonlinear structured illumination in light-sheet microscopy will be introduced. By combining two photon light-sheet microscopy and nonlinear structured illumination, 3D live sample imaging at cellular resolution in depth beyond 200 microns has been achieved on live zebrafish.

Appendix-Nonlinear Structured Illumination Application in Light-Sheet

Microscopy

In the previous chapters, the ability for structured illumination microscopy to improve the resolution of the imaging system has been proven theoretically and experimentally. Other than the resolution improvement, structured illumination technique was originally invented to achieve better sectioning image by removing emission from out of focus samples. In this chapter, the application of nonlinear structured illumination in two photon light-sheet microscopy is studied. By combining two photon light-sheet microscopy and nonlinear structured illumination, 3D live sample imaging at cellular resolution in depth beyond 200 microns has been achieved on live zebrafish. Two-color imaging of pronephric glomeruli and vasculature of zebrafish kidney, whose cellular structures located at the center of the fish body are revealed in high clarity by two-color two-photon Bessel light-sheet SIM.

A1 Light-sheet microscopy

A1.1 Introduction to light-sheet fluorescent microscopy

Light-sheet illumination or select plane illumination [22, 70], which is generated to excite the sample at a specific z section by scanning a circular beam in a plane or focusing beam in one direction with prism, is capable of penetrating thick tissue layers while still maintaining cellular resolution and has been demonstrated as a fast 3D microscopy approach capable of live sample imaging, which makes it highly demand. Compared with other techniques, such as point scanning techniques, Confocal or multi-photon fluorescence microscopy, which are also suitable for 3D live sample imaging, light-sheet illumination not only owns the advantage of higher

imaging speed, but also deeper sample imaging with less photo damage and stress induced on the living sample, for the optical axis of the detection instruments is perpendicular to the plane of light-sheet illumination and only the actually observed section is illuminated.

A1.2 Limitation of traditional light-sheet fluorescent microscopy

However, the traditional light-sheet microscopy generated by cylindrical lens has many shortcomings as listed below:

1, As the nature of Gaussian beam, the traditional light-sheet microscopy has the compromise between axial resolution and the field of view, since short beam waist and long depth of focus cannot be acquired simultaneously.

2, The field-of-view of light-sheet microscopy is also limited by the penetration depth of illumination light through the sample. Although the field-of-view can be doubled with so called two-side sheet illumination, the complexity and the cost of imaging system are also added to the microscope [71, 72].

3, Image quality of light-sheet microscopy is affected by tissue scattering in emission photon detection path, which degrades the resolution of system in deep tissue and presents a strongly blurred image when imaging deep samples.

Therefore, large and deep sample imaging in live samples is still challenging with traditional light-sheet imaging.

A2 Two-photon Bessel light-sheet microscope with nonlinear structured illumination

A2.1 Introduction to two-photon Bessel light-sheet microscope with nonlinear SIM

To overcome those limitations, Combination of the two-photon light-sheet illumination imaging with Bessel beam technique and nonlinear structured illumination microscopy is chosen for the advantages discussed in detail as follows:

1. Rather than one photon excitation, two-photon excitation is applied [73]. The excitation penetration with two-photon excitation is deeper compared with the one with one-photon excitation because of the application of longer excitation wavelength. Similar to the two-photon application in confocal microscope, any out of layer emission will be weaker since the fluorescence emission is proportional to the square of the excitation intensity.
2. Instead of traditional Gaussian beam, Bessel beam is applied to generate the light-sheet illumination. Better penetration in scattering tissue can be obtained with the Bessel light-sheet due to the ‘self-healing’ effect [74]. Because of the non-diffractive nature of Bessel beam, larger field-of-view can be realized with Bessel beam light sheet microscopy while maintaining high axial resolution [75]. The photo-toxicity of Bessel light-sheet could be potentially higher than Gaussian light-sheet since the light is tightly focused over a longer distance with Bessel light-sheet. However, our experimental results showed that, similar to two-photon Gaussian light-sheet, two-photon Bessel light-sheet does not cause long-term photo-toxicity in live zebrafish.
3. Nonlinear structured-illumination microscopy (SIM) is applied to remove the diffused photons derived from deep tissue scattering in the emission path. Previously, a three-

phase optical sectioning method had been used in light-sheet microscopy to remove the scattered photons and improve image quality in deeper layers [76-78]. Compared with the three-phase optical sectioning method, nonlinear SIM has higher signal-to-noise ratio in terms of removing out-of-focal-plane photos.

4. As out-of-focal-plane excitation and tissue scattering in emission path both impose diffused background over the ballistic image, more effective out of focus light rejection is expected with nonlinear SIM than the three-phase optical sectioning method in deep tissue light-sheet illumination imaging. However, completely removing of strong diffused photon background cannot be fulfilled with the standard nonlinear SIM image reconstruction algorithm. Therefore, a large amount of artifacts would be introduced into the final image due to the residue diffused emission photons. A critical modification of the standard nonlinear SIM algorithm is required to remove diffusion-induced artifacts and improve the diffusion reduction.

Due to the advantages described above, two-photon Bessel beam light-sheet microscopy with nonlinear structured illumination is capable of 3D imaging in large and deep live samples with cellular resolution. The theory and algorithm study for this instrument will be studied in the next section.

A2.2 The theory and algorithm development in two-photon Bessel light-sheet microscope with nonlinear SIM

In deep tissue imaging with the sample of more than 200 μm thickness, the acquired image is usually strongly blurred by tissue scattering of emission photons, with the loss of image contrast

and effective resolution of the light-sheet images, indicating that the emission light propagation is reaching the ballistic transport limit. The sample we will image with this technique is zebrafish kidney, which is located in the center of the fish body and its renal glomeruli structures are not fully developed until about 4 days post fertilization (dpf). At that time, the top layer of kidney is at least 200 μm beneath the surface from all sides of the fish surface. Observing the cellular structures of the kidney in live intact larvae at 4 dpf is extremely challenging because of the strong tissue scattering due to the thick tissue and the increasing amount of pigmentation (1-Phenyl-2-thiourea treatment, a standard practice for delaying pigmentation in zebrafish imaging study, starts losing effect at 3 dpf).

In order to realize 3D imaging in large and deep live samples with cellular resolution, the algorithm of nonlinear structured illumination microscopy in the two-photon Bessel light-sheet system is developed. A stripe-pattern light-sheet is generated by hopping the Bessel beam in uniform steps during sheet scan, the experimental details of which will be described in detail later. Due to the nature of Bessel beam and two-photon excitation, the effective excitation pattern is highly nonlinear and can be expressed as

$$I(x, y) = \sum_{n=-N}^N a_n \exp(ink_0 y) \quad (\text{A1})$$

where k_0 is the spatial frequency of the illumination pattern, and a_n is the harmonics order coefficient constant. The image expression is given by

$$M(x, y) = O(x, y) I(x, y) \otimes \text{PSF} \quad (\text{A2})$$

where $O(x, y)$ is the emission signal and PSF is the point spread function of the imaging system.

When the photon emission is subjected to tissue scattering, the emission signal is split into a ballistic signal O_b and a diffused signal O_d , and the acquired image becomes

$$M(x, y) = O_b(x, y)I(x, y) \otimes PSF + O_d(x, y)I(x, y) \otimes PSF_s \otimes PSF \quad (A3)$$

where PSF_s is the point spread function induced by scattering. In the Fourier space, the acquired image is

$$\begin{aligned} \tilde{M}(k_x, k_y) &= \tilde{O}_b \otimes \tilde{I} \times OTF + \tilde{O}_d \otimes \tilde{I} \times OTF_s \times OTF \\ &= \sum_{n=-N}^N a_N [\underbrace{\tilde{O}_b(k_x, k_y + nk_0) + \tilde{O}_d(k_x, k_y + nk_0)OTF_s}_{\text{}}] \times OTF \end{aligned} \quad (A4)$$

where OTF is the optical transfer function of the imaging system, and OTF_s is the optical transfer function of tissue scattering process. $2N + 1$ phase shifted images are acquired to solve all the component in Eq. A4 [79]. Each order represents a frequency-shifted Fourier image of the emission object.

In non-zero orders of these Fourier images, the emission signal is shifted to higher spatial frequencies by nk_0 , as illustrated in figure A1 (a). The scatter OTF_s , also illustrated in figure A1 (a), is a low-pass filter and remains at near zero frequency. The fundamental reason for the scatter OTF_s to be a low-pass filter is the point spread function for scattering process is much wider than the diffraction limit PSF. The diffused signal is therefore filtered out by OTF_s except in the zero frequency regions (figure A1 (b)). In standard SIM algorithm, the frequency center of the Fourier image is shifted back to zero (figure A1 (c)) and then performed an inverse Fourier transform to acquire the reconstructed image. However, if the diffused signal is strong, there is a residue of diffused signal remains in the Fourier image to cause artifact in final reconstructed image.

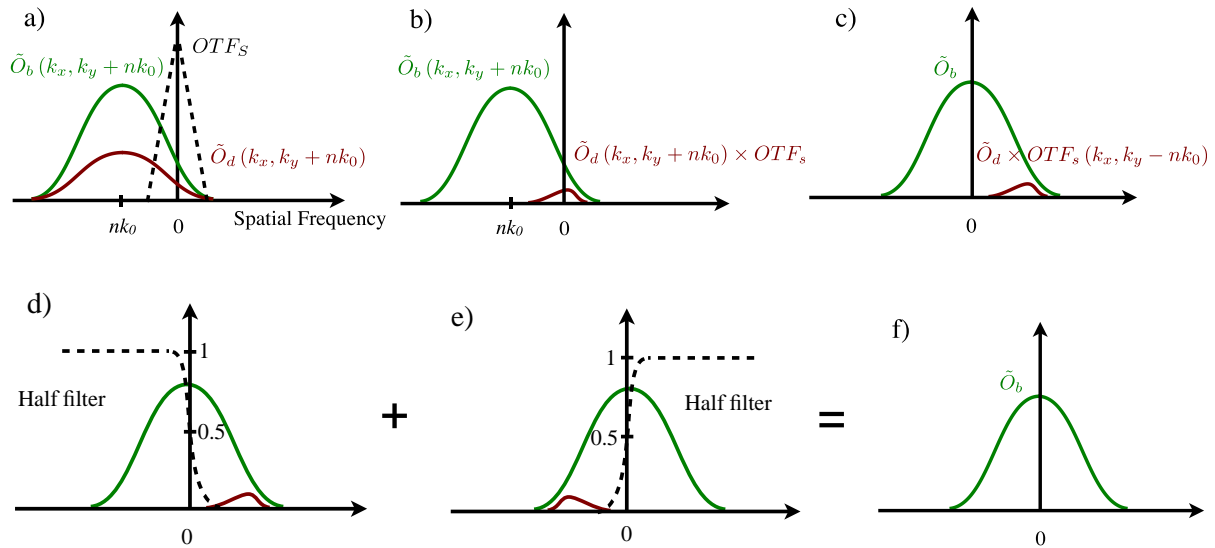


Figure A1 The nonlinear SIM Imaging processing steps to remove strong diffused signal in light-sheet imaging of deep tissue structures[80].

In order to remove the effect of the residue of diffused signal, an improved SIM algorithm, which merges two diffusion-free halves of two Fourier images together and reconstructed from $-n$ (Figure A1 (d)) and $+n$ orders (Figure A1 (e)), respectively, can be developed. With the improved nonlinear SIM method, each of the $+n$ and $-n$ Fourier components produces a fully reconstructed diffusion-free image. Since it is impossible to remove the diffused photon background signal, the 0th order Fourier image data is discarded.

After optimization of the nonlinear SIM described in the later section, a 5-step phase shift SIM scan was chosen in our experiments. The imaging processing produces two diffusion-free images from 1st and 2nd order pairs respectively. The image reconstructed from 2nd order Fourier images has better diffusion rejection but with a lower SNR due to the weaker harmonic coefficient a_2 . By overlay the images from the 1st and 2nd order reconstruction with a specific weighting ratio chosen based on the balance of diffusion reduction and SNR, a final image is then produced.

Similar to the traditional nonlinear SIM, the final image has superresolution since the Fourier bandwidth is extended by Nk_0 in the y-axis direction. However, in our case, since the period of the pattern is 11.2 μm and the spatial vector k_0 is much smaller than the diffraction limit, the superresolution effect is not significant.

A2.3 Optical setup and sample preparation

After the development of the novel nonlinear SIM reconstruction algorithm, the optical setup is built up to realize the Bessel beam light-sheet two-photon illumination microscope in experiment (figure A2 (a)). An beam expander is applied to expand the output beam from a femtosecond Ti: Sapphire laser (Newport Tsunami) to the size of 8 mm of FWHM, so the aperture of the phase spatial light modulator (SLM) (Hamamatsu X10468-07, 800-by-600, 20 μm pitch) can be fully utilized with minimal pixilation effect. The laser power is in the range of 100~200 mW on live samples. A narrow collimated beam is performed on the sample after the objective (Mitutoyo 20x long working distance, NA=0.42) when a uniform phase is imposed on the SLM, as shown in figure A2 (a). With a spherical lens phase pattern imposed on the SLM, a focused Gaussian shaped beam is generated and a typical localized two-photon signal is observed (Figure. A2 (b)). A Bessel beam two-photon excitation is generated with extended focal depth (Figure A2 (c)) when the SLM is switched to an axicon phase pattern.

The plane illumination is generated when the Bessel beam is translated in Y-axis direction (perpendicular to the paper in figure A1(a)) by a galvanometer mirror. Emission images are collected at 90° to the Bessel beam axis, through a water immersion long working distance

objective lens (40X, NA 0.8, Olympus), a zooming tube lens (Sigma Photo, 300-70 mm) and is projected onto an EMCCD (Rolera Thunder, 512-by-512, 16 μm pitch). A refractive index matched FEP tube is utilized to mount the sample and its position and shifting z-axis during 3D imaging is controlled by a motorized stage. When the tube lens is zoomed to 300 mm, the best lateral resolution of 0.5 μm can be achieved. A high-speed motorized filter wheel is placed in front of the camera to switch the emission filter to perform dual-color imaging.

The live samples imaged in the experiments were live zebrafish embryo, which were maintained in embryo medium with 0.003% 1-Phenyl-2-thiourea. Fishes between 1 to 5 dpf were mounted in a 0.8-mm ID FEP tube with embryo medium containing 0.1% low melting point agarose and 200 mg/L tricaine. The tube is plugged with a solid 1% agarose gel plug. In the IR range at wavelengths around 800 nm, the optical property of the FEP tube matches with water well. As shown in figure A3 (a), the Bessel beam maintains a strong and long two-photon excitation line in FEP tubes filled with dye solution, showing no degradation due to astigmatism.

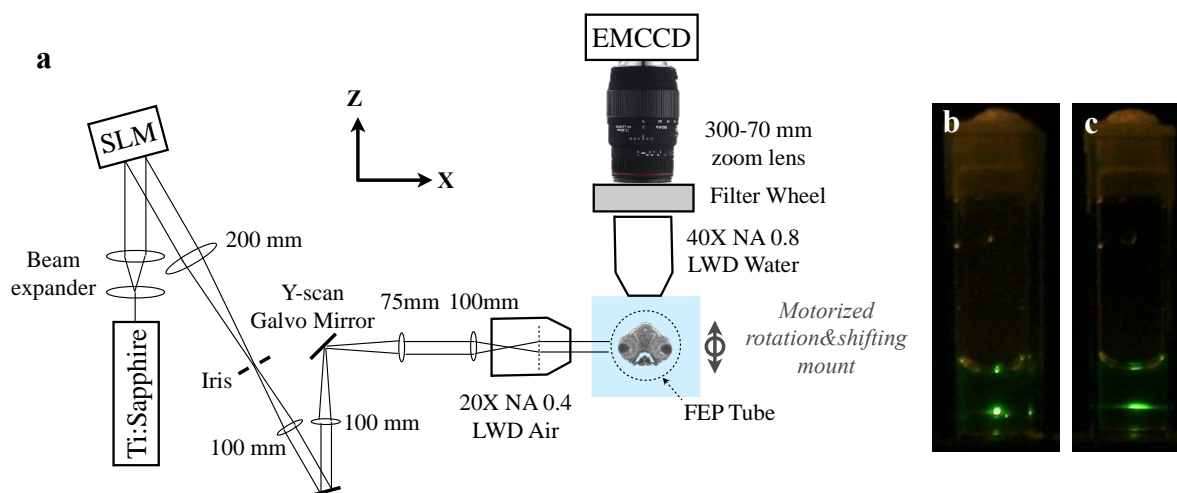


Figure A2 (a) Optical schematic of the nonlinear structured illumination Bessel beam two-photon light-sheet microscope. SLM: spatial light modulator. (b) Two-photon emission from a cuvette of fluorescein solution under a focused Gaussian beam, and (c) under a Bessel beam[80].

A2.4 The axial and lateral imaging resolution characterization

The axial resolution of the system was measured by imaging a fluorescein solution with Bessel beam. The two-photon emission has over 50% uniformity over a 600 μm span (figure A2 (a)). The main-band signal has a width of 2 μm , indicating a 2 μm axial resolution of the light-sheet system.

To measure the lateral resolution of the system, green fluorescent beads with 20-nm diameter (Invitrogen) embedded in 1% agarose gel with light-sheet illumination was imaged. The image of single bead shows a diffraction-limited 0.5 μm point spread function (figure A2 (b)) at the sampling rate of 27 μm per pixel.

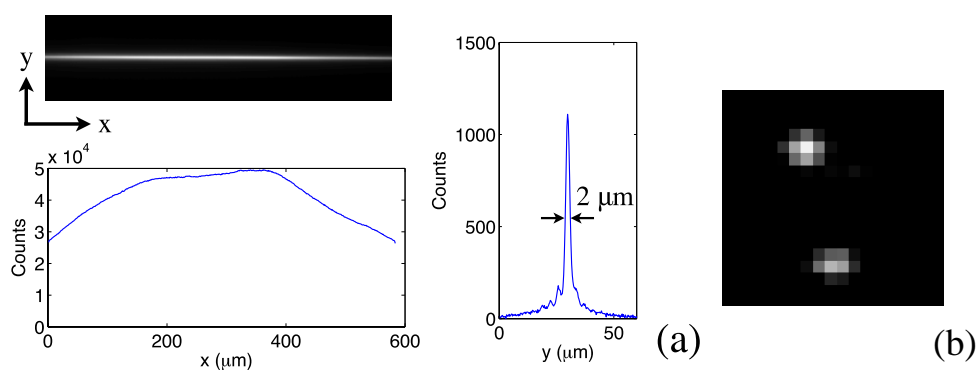


Figure A3 Axial and lateral resolution calibration. (a) Field uniformity over a 600 μm distance and 2 μm axial resolution, measured by imaging a fluorescein solution filled FEP tube. (b) Diffraction limited 0.5 μm lateral resolution, measured by imaging 20-nm diameter beads at 0.27 μm per pixel[80].

A2.5 Structured illumination parameter optimization

In order to generate highly nonlinear periodic illumination (figure A4 (a)), instead of scanning Bessel beam with constant speed, the Bessel beam is scanned in fixed steps by hopping the laser beam. The phase of the pattern is controlled by the initial position of the laser beam scanner, and the period of the pattern is adjusted by changing the hopping step size. Figure A4 (b) plots the spatial power spectra of an excitation pattern, taken from a fluorescein solution sample. High order harmonics of the excitation pattern are prominent as shown in figure A4 (b).

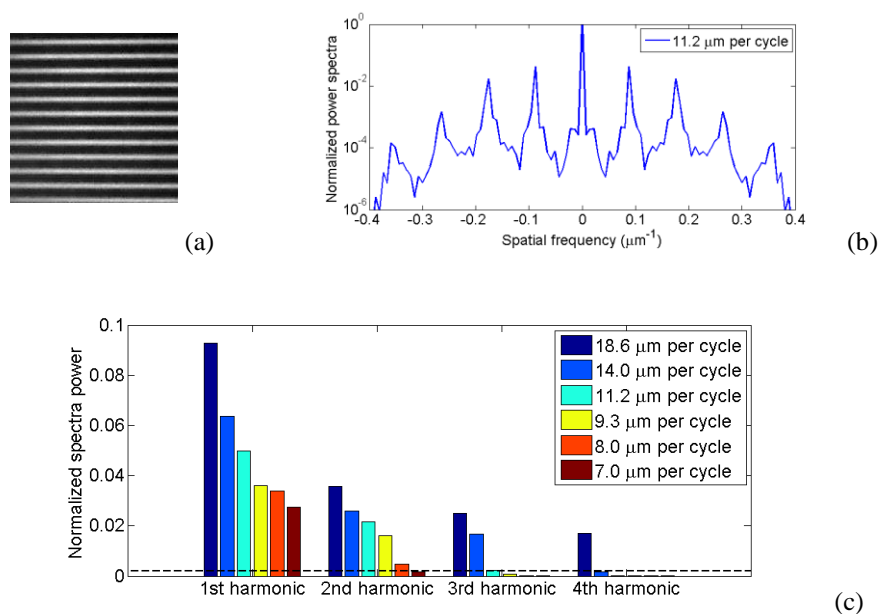


Figure A4 (a) Nonlinear structured two-photon excitation image from a fluorescein solution sample. (b) Normalized spatial power spectrum of two-photon excitation patterns showing high order harmonics of the pattern. (c) Normalized spectra powers at different harmonic orders of the excitation pattern with different pattern period. Different color represents varied pattern period. The dashed line is the typical noise level of light-sheet images deep inside zebrafish[80].

In non-linear SIM, small phase shift step $2\pi/2N + 1$ of the pattern is required to get a uniform illumination effectively after the summation of the complete exposure sequence. Otherwise artifacts will be inevitable in the reconstructed image. The noise level is the key factor to determine the maximum harmonics order to be solved and the number of phase-shift steps required. Figure A4 (b) illustrates the power spectrum of the excitation pattern in figure A4 (a), which was obtained from fluorescence solution sample. All harmonic orders above the imaging noise level (dashed line in figure A4 (c)) need to be considered in the image reconstruction to remove the artifacts in the final image. Therefore, harmonic orders equal or below the 3rd, 2nd and 1st order are required to be considered for illumination pattern period of 14 μm , 11.2 μm , and 7.0 μm , respectively.

Linear SIM, requires a 7.0 μm period pattern and gives significantly weaker signal strength at the 1st harmonic order, whereas 3rd order nonlinear SIM requires 7 exposures per sequence. Considering those limitations, 2nd order non-linear SIM with 5 phase steps was applied for *in vivo* two-photon imaging of developing embryos and larvae in our system. Among all pattern periods suitable for 5-phase nonlinear SIM, the 11.2 μm pattern period was selected for the strongest pattern harmonic orders it can provide. Our two-photon excitation pattern presents a contrast of 60% under such condition, which means 60% of the emission photons are utilized in the reconstruction and the rest 40% are discarded in the form of 0th order image.

A2.6 Nonlinear structured light-sheet illumination microscopy on zebrafish kidney

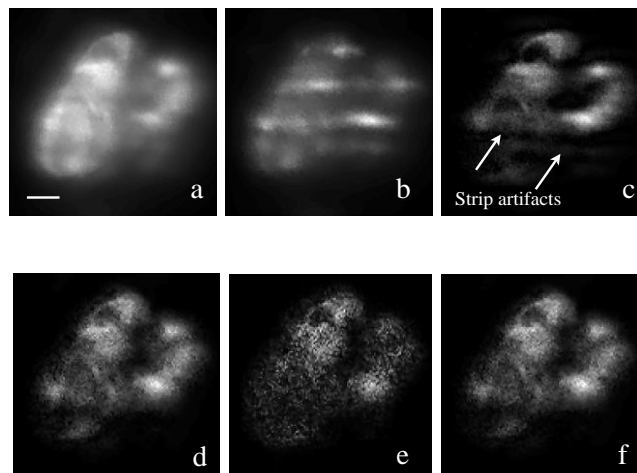


Figure A5 Diffusion reductions with our novel nonlinear SIM reconstruction algorithm. (a) The summation of 5 SIM raw frames with phase-shifted patterns. The merged image is similar to a 5-seconds-exposure image under uniform light-sheet. (b) One of the raw image frames under structured light-sheet illumination. The exposure time was 2s. (c) Reconstructed image under the standard SIM algorithm, showing stripe-shaped artifacts due to residual emission photon diffusion; (d) Reconstructed image from ± 1 order harmonics pair following the improved SIM reconstruction algorithm. (e) Reconstructed image from ± 2 order harmonics pair by the improved SIM algorithm; (f) Weighted merge of ± 1 and ± 2 order reconstructed image. The samples were the kidney of a live transgenic *Tg (pod::mCherry)* zebrafish at 4 dpf. Podocytes in the fish kidney is labeled with mCherry dye. The scale bar is 10 μm [80].

Figure A5 (a-f) illustrates the diffusion reduction process in deep tissue two-photon Bessel light-sheet imaging. Figure A5 (a) shows an *in vivo* light-sheet image of glomerulus structures, which was taken from a 4 dpf live transgenic *Tg (pod::mCherry)* zebrafish larva at $\sim 250 \mu\text{m}$ deep from the fish skin. Under uniform light-sheet illumination (figure A5 (a)), which is merged from 5 structured illuminated frames (figure A5 (b)) with different phases, the image is severely blurred by tissue scatter. The comparison of standard nonlinear SIM reconstruction algorithm and

improved nonlinear SIM reconstruction algorithm are presented in figure A5 (c-f). Strong stripe-shaped artifacts are received after standard reconstruction, although the diffused noise is significantly removed as shown in figure A5 (c). The improved non-linear SIM reconstruction algorithm is then employed to remove these artifacts. Figure A5 (d) and (e) shows the reconstructed images from ± 1 and ± 2 order harmonics pairs, respectively. Figure A5 (f) presents a merged image of ± 1 and ± 2 orders, with the 1st order result weighed twice more than the 2nd order.

The SNR of figure A5 (f) is lower than the equivalent uniform-illumination image owing to the following reason:

100% of the shot noise remains although more than 40% of the photons are discarded due to the imperfect pattern contrast. Although diffused photon signals are filtered out by SIM through spatial spectra manipulation, the white-spectrum shot-noise associated with diffused photons remains. The SNR of SIM reconstructed image is given by

$$SNR_{SIM} \propto \frac{m\sqrt{T}n_b}{\sqrt{n_{total}}} \quad (A5)$$

where m is the illumination pattern contrast, T is the exposure time, n_b and n_{total} are the ballistic photon flux and total photon flux, respectively. The noise of the diffused photon signal originated from adjacent structures can reduce the visibility of one structure in the final SIM image. However, increasing exposures time is an effective way to reduce such noise. Exposure time twice of the typical time used to acquire images from surface layers using the uniform light-sheet is utilized to acquire the SIM image shown in figure A5 (f).

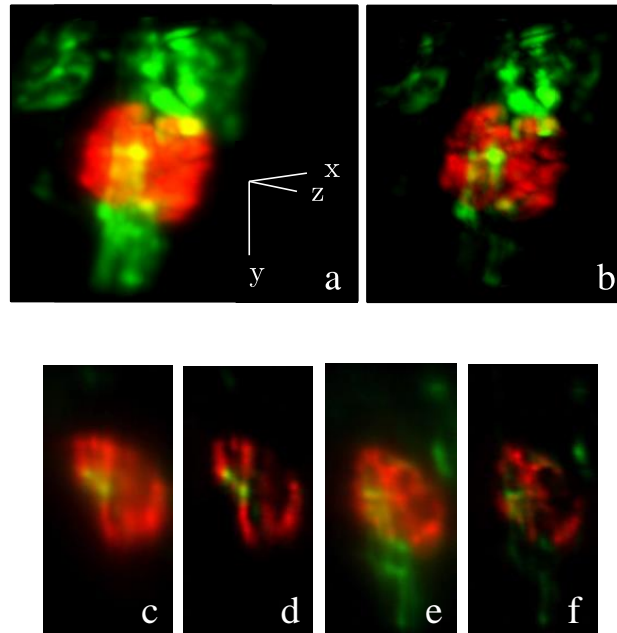


Figure A6 3D two-color images of kidney cellular structure of a live double transgenic zebrafish larva at 4dpf. Green fluorescence protein (GFP) labels endothelial cells in the vasculature and presented in green color. mCherry (red) labels podocytes. (a) Maximum intensity projection of 3D image set taken with a uniform light-sheet illumination; (b) Maximum intensity projection of diffusion-free 3D image set obtained with nonlinear structured light-sheet illumination; (c) A x-z plane cross section (anterior view) of the 3D image taken with a uniform light-sheet (d) Same cross section as (c), taken with structured light-sheet; (e) A y-z plane cross section (lateral view) of the 3D image taken with a uniform light-sheet; (f) Same cross section as (e), taken with structured light-sheet. The scale bar is 20 μm [80].

The cellular structures of zebrafish kidney at 4 dpf in double transgenic fish *Tg (pod:mCherry; kdrl:GFP)* [81] is imaged by two-photon Bessel beam light-sheet SIM microscope with the improved nonlinear SIM algorithm. This zebrafish has GFP-expressing endothelial cells and mCherry-expressing renal podocytes. With uniform light-sheet microscopy, the acquired 3D images are highly blurred, especially in densely structured glomeruli. With our nonlinear SIM light-sheet microscopy, figure A6 (b) shows diffusion-free 3D image set under maximum

intensity projection. The individual podocytes are visible in this figure. The corresponding cross section images presented in figure A6 (d) and (f) clearly show podocytes wrapping around endothelial cells in vasculature.

A3 Summary

In this chapter, the application of nonlinear structured illumination in light-sheet microscopy is introduced. With the combination of two-photon light sheet microscopy and nonlinear structured illumination, our instrument is capable of 3D imaging in deep live samples with cellular resolution and wide field of view. With an improved nonlinear SIM reconstruction algorithm, the diffused signal from the emission sample can be significantly reduced and stripe-shaped artifacts can be removed from final image. With this technique, the 3D live imaging on double transgenic zebrafish kidney, which is deep in the zebrafish body, is successfully acquired with artifact-free image quality.

References

1. Denk, W., J.H. Strickler, and W.W. Webb, *Two-photon laser scanning fluorescence microscopy*. Science, 1990. **248**(4951): p. 73-76.
2. Wilson, T., *Confocal microscopy*. Academic Press: London, etc, 1990. **426**: p. 1-64.
3. Amos, W. and J. White, *How the confocal laser scanning microscope entered biological research*. Biology of the Cell, 2003. **95**(6): p. 335-342.
4. Helmchen, F. and W. Denk, *Deep tissue two-photon microscopy*. Nature methods, 2005. **2**(12): p. 932-940.
5. Zipfel, W.R., R.M. Williams, and W.W. Webb, *Nonlinear magic: multiphoton microscopy in the biosciences*. Nature biotechnology, 2003. **21**(11): p. 1369-1377.
6. Hell, S.W., *Microscopy and its focal switch*. Nature methods, 2008. **6**(1): p. 24-32.
7. Hell, S.W., *Far-field optical nanoscopy*. Science, 2007. **316**(5828): p. 1153-1158.
8. Huang, B., H. Babcock, and X. Zhuang, *Breaking the diffraction barrier: super-resolution imaging of cells*. Cell, 2010. **143**(7): p. 1047-1058.
9. Schermelleh, L., R. Heintzmann, and H. Leonhardt, *A guide to super-resolution fluorescence microscopy*. The Journal of cell biology, 2010. **190**(2): p. 165-175.
10. Lippincott-Schwartz, J. and S. Manley, *Putting super-resolution fluorescence microscopy to work*. Nature methods, 2008. **6**(1): p. 21-23.
11. Leung, B.O. and K.C. Chou, *Review of super-resolution fluorescence microscopy for biology*. Applied spectroscopy, 2011. **65**(9): p. 967-980.
12. Huang, B., *Super-resolution optical microscopy: multiple choices*. Current opinion in chemical biology, 2010. **14**(1): p. 10-14.
13. Betzig, E., et al., *Imaging intracellular fluorescent proteins at nanometer resolution*. Science, 2006. **313**(5793): p. 1642-1645.
14. Shroff, H., et al., *Live-cell photoactivated localization microscopy of nanoscale adhesion dynamics*. Nature methods, 2008. **5**(5): p. 417-423.
15. Manley, S., et al., *High-density mapping of single-molecule trajectories with photoactivated localization microscopy*. Nature methods, 2008. **5**(2): p. 155-157.
16. Hess, S.T., T.P. Girirajan, and M.D. Mason, *Ultra-high resolution imaging by fluorescence photoactivation localization microscopy*. Biophysical journal, 2006. **91**(11): p. 4258-4272.
17. Gould, T.J., V.V. Verkhusha, and S.T. Hess, *Imaging biological structures with fluorescence photoactivation localization microscopy*. Nature protocols, 2009. **4**(3): p. 291-308.
18. Fölling, J., et al., *Fluorescence nanoscopy by ground-state depletion and single-molecule return*. Nature methods, 2008. **5**(11): p. 943-945.
19. Han, K.Y., et al., *Metastable dark states enable ground state depletion microscopy of nitrogen vacancy centers in diamond with diffraction-unlimited resolution*. Nano letters, 2010. **10**(8): p. 3199-3203.
20. Rust, M.J., M. Bates, and X. Zhuang, *Sub-diffraction-limit imaging by stochastic optical reconstruction microscopy (STORM)*. Nature methods, 2006. **3**(10): p. 793-796.
21. van de Linde, S., et al., *Direct stochastic optical reconstruction microscopy with standard fluorescent probes*. Nature protocols, 2011. **6**(7): p. 991-1009.

22. Keller, P.J., et al., *Reconstruction of zebrafish early embryonic development by scanned light sheet microscopy*. Science, 2008. **322**(5904): p. 1065-1069.
23. Heilemann, M., et al., *Subdiffraction - resolution fluorescence imaging with conventional fluorescent probes*. Angewandte Chemie International Edition, 2008. **47**(33): p. 6172-6176.
24. Hell, S.W. and J. Wichmann, *Breaking the diffraction resolution limit by stimulated emission: stimulated-emission-depletion fluorescence microscopy*. Optics letters, 1994. **19**(11): p. 780-782.
25. Klar, T.A. and S.W. Hell, *Subdiffraction resolution in far-field fluorescence microscopy*. Optics letters, 1999. **24**(14): p. 954-956.
26. Moneron, G. and S.W. Hell, *Two-photon excitation STED microscopy*. Optics express, 2009. **17**(17): p. 14567-14573.
27. Willig, K.I., et al., *Nanoscale resolution in GFP-based microscopy*. Nature methods, 2006. **3**(9): p. 721.
28. Gustafsson, M.G., *Surpassing the lateral resolution limit by a factor of two using structured illumination microscopy*. Journal of microscopy, 2000. **198**(2): p. 82-87.
29. Schermelleh, L., et al., *Subdiffraction multicolor imaging of the nuclear periphery with 3D structured illumination microscopy*. Science, 2008. **320**(5881): p. 1332-1336.
30. Gustafsson, M.G., et al., *Three-dimensional resolution doubling in wide-field fluorescence microscopy by structured illumination*. Biophysical journal, 2008. **94**(12): p. 4957-4970.
31. Shao, L., et al., *Super-resolution 3D microscopy of live whole cells using structured illumination*. Nature methods, 2011. **8**(12): p. 1044-1046.
32. Gustafsson, M.G., *Nonlinear structured-illumination microscopy: wide-field fluorescence imaging with theoretically unlimited resolution*. Proceedings of the National Academy of Sciences of the United States of America, 2005. **102**(37): p. 13081-13086.
33. Rego, E.H., et al., *Nonlinear structured-illumination microscopy with a photoswitchable protein reveals cellular structures at 50-nm resolution*. Proceedings of the National Academy of Sciences, 2012. **109**(3): p. E135-E143.
34. Rittweger, E., et al., *STED microscopy reveals crystal colour centres with nanometric resolution*. Nature Photonics, 2009. **3**(3): p. 144-147.
35. Huang, B., M. Bates, and X. Zhuang, *Super resolution fluorescence microscopy*. Annual review of biochemistry, 2009. **78**: p. 993.
36. Hell, S.W., *Toward fluorescence nanoscopy*. Nature biotechnology, 2003. **21**(11): p. 1347-1355.
37. Heintzmann, R. and C.G. Cremer. *Laterally modulated excitation microscopy: improvement of resolution by using a diffraction grating*. in *BiOS Europe'98*. 1999: International Society for Optics and Photonics.
38. Frohn, J.T., H.F. Knapp, and A. Stemmer, *True optical resolution beyond the Rayleigh limit achieved by standing wave illumination*. Proceedings of the National Academy of Sciences, 2000. **97**(13): p. 7232-7236.
39. Kner, P., et al., *Super-resolution video microscopy of live cells by structured illumination*. Nature methods, 2009. **6**(5): p. 339-342.

40. Fernández-Suárez, M. and A.Y. Ting, *Fluorescent probes for super-resolution imaging in living cells*. Nature Reviews Molecular Cell Biology, 2008. **9**(12): p. 929-943.
41. Bates, M., et al., *Multicolor super-resolution imaging with photo-switchable fluorescent probes*. Science, 2007. **317**(5845): p. 1749-1753.
42. Nägerl, U.V., et al., *Live-cell imaging of dendritic spines by STED microscopy*. Proceedings of the National Academy of Sciences, 2008. **105**(48): p. 18982-18987.
43. Hein, B., K.I. Willig, and S.W. Hell, *Stimulated emission depletion (STED) nanoscopy of a fluorescent protein-labeled organelle inside a living cell*. Proceedings of the National Academy of Sciences, 2008. **105**(38): p. 14271-14276.
44. Westphal, V., et al., *Video-rate far-field optical nanoscopy dissects synaptic vesicle movement*. Science, 2008. **320**(5873): p. 246-249.
45. Jones, S.A., et al., *Fast, three-dimensional super-resolution imaging of live cells*. Nature methods, 2011. **8**(6): p. 499-505.
46. Zanicchi, F.C., et al., *Live-cell 3D super-resolution imaging in thick biological samples*. Nature methods, 2011. **8**(12): p. 1047-1049.
47. Heintzmann, R. and M.G. Gustafsson, *Subdiffraction resolution in continuous samples*. Nature Photonics, 2009. **3**(7): p. 362-364.
48. Klar, T.A., E. Engel, and S.W. Hell, *Breaking Abbe's diffraction resolution limit in fluorescence microscopy with stimulated emission depletion beams of various shapes*. Physical Review E, 2001. **64**(6): p. 066613.
49. Fain, B. and P.W. Milonni, *Classical stimulated emission*. JOSA B, 1987. **4**(1): p. 78-85.
50. Willig, K.I., et al., *STED microscopy with continuous wave beams*. Nature methods, 2007. **4**(11): p. 915-918.
51. Zhang, H., M. Zhao, and L. Peng, *Nonlinear structured illumination microscopy by surface plasmon enhanced stimulated emission depletion*. Optics express, 2011. **19**(24): p. 24783-24794.
52. Chang, B.-J., et al., *Isotropic image in structured illumination microscopy patterned with a spatial light modulator*. Optics express, 2009. **17**(17): p. 14710-14721.
53. Heintzmann, R., T.M. Jovin, and C. Cremer, *Saturated patterned excitation microscopy—a concept for optical resolution improvement*. JOSA A, 2002. **19**(8): p. 1599-1609.
54. Homola, J., *Electromagnetic theory of surface plasmons*, in *Surface Plasmon Resonance Based Sensors*. 2006, Springer. p. 3-44.
55. Willig, K.I., et al., *STED microscopy reveals that synaptotagmin remains clustered after synaptic vesicle exocytosis*. Nature, 2006. **440**(7086): p. 935-939.
56. Kasper, R., et al., *Single - Molecule STED Microscopy with Photostable Organic Fluorophores*. Small, 2010. **6**(13): p. 1379-1384.
57. Pattnaik, P., *Surface plasmon resonance*. Applied biochemistry and biotechnology, 2005. **126**(2): p. 79-92.
58. Van Der Merwe, P.A., *Surface plasmon resonance*. 2001, Oxford University Press: New York, NY, USA. p. 137-170.
59. Kneipp, K., et al., *Single molecule detection using surface-enhanced Raman scattering (SERS)*. Physical review letters, 1997. **78**(9): p. 1667.
60. Chung, E., et al., *Wide-field extended-resolution fluorescence microscopy with standing surface-plasmon-resonance waves*. Optics letters, 2009. **34**(15): p. 2366-2368.

61. Ekgasit, S., F. Yu, and W. Knoll, *Fluorescence intensity in surface-plasmon field-enhanced fluorescence spectroscopy*. Sensors and Actuators B: Chemical, 2005. **104**(2): p. 294-301.
62. He, R.-Y., et al., *Enhanced live cell membrane imaging using surface plasmon-enhanced total internal reflection fluorescence microscopy*. Optics express, 2006. **14**(20): p. 9307-9316.
63. He, R.-Y., et al., *Surface plasmon-enhanced two-photon fluorescence microscopy for live cell membrane imaging*. Optics express, 2009. **17**(8): p. 5987-5997.
64. Hatta, A., Y. Suzuki, and W. Suëtaka, *Infrared absorption enhancement of monolayer species on thin evaporated Ag films by use of a Kretschmann configuration: Evidence for two types of enhanced surface electric fields*. Applied Physics A, 1984. **35**(3): p. 135-140.
65. West, P.R., et al., *Searching for better plasmonic materials*. Laser & Photonics Reviews, 2010. **4**(6): p. 795-808.
66. Liebermann, T. and W. Knoll, *Surface-plasmon field-enhanced fluorescence spectroscopy*. Colloids and Surfaces A: Physicochemical and Engineering Aspects, 2000. **171**(1): p. 115-130.
67. Mudry, E., et al., *Structured illumination microscopy using unknown speckle patterns*. Nature Photonics, 2012. **6**(5): p. 312-315.
68. Orioux, F., et al., *Bayesian estimation for optimized structured illumination microscopy*. Image Processing, IEEE Transactions on, 2012. **21**(2): p. 601-614.
69. Cox, S., et al., *Bayesian localization microscopy reveals nanoscale podosome dynamics*. Nature methods, 2012. **9**(2): p. 195-200.
70. Huisken, J., et al., *Optical sectioning deep inside live embryos by selective plane illumination microscopy*. Science, 2004. **305**(5686): p. 1007-1009.
71. Krzic, U., et al., *Multiview light-sheet microscope for rapid in toto imaging*. Nature methods, 2012. **9**(7): p. 730-733.
72. Tomer, R., et al., *Quantitative high-speed imaging of entire developing embryos with simultaneous multiview light-sheet microscopy*. Nature methods, 2012. **9**(7): p. 755-763.
73. Truong, T.V., et al., *Deep and fast live imaging with two-photon scanned light-sheet microscopy*. Nature methods, 2011. **8**(9): p. 757-760.
74. Fahrbach, F.O., P. Simon, and A. Rohrbach, *Microscopy with self-reconstructing beams*. Nature Photonics, 2010. **4**(11): p. 780-785.
75. Fahrbach, F.O., et al., *Light-sheet microscopy in thick media using scanned Bessel beams and two-photon fluorescence excitation*. Optics express, 2013. **21**(11): p. 13824-13839.
76. Neil, M., R. Juskaitis, and T. Wilson, *Method of obtaining optical sectioning by using structured light in a conventional microscope*. Optics letters, 1997. **22**(24): p. 1905-1907.
77. Keller, P.J., et al., *Fast, high-contrast imaging of animal development with scanned light sheet-based structured-illumination microscopy*. Nature methods, 2010. **7**(8): p. 637-642.
78. Mertz, J., *Optical sectioning microscopy with planar or structured illumination*. Nature methods, 2011. **8**(10): p. 811-819.
79. Heintzmann, R., *Saturated patterned excitation microscopy with two-dimensional excitation patterns*. Micron, 2003. **34**(6): p. 283-291.

80. Zhao, M., et al., *Cellular imaging of deep organ using two-photon Bessel light-sheet nonlinear structured illumination microscopy*. Biomedical optics express, 2014. **5**(5): p. 1296-1308.
81. Zhou, W. and F. Hildebrandt, *Inducible podocyte injury and proteinuria in transgenic zebrafish*. Journal of the American Society of Nephrology, 2012. **23**(6): p. 1039-1047.